Graz University of Technology

Modeling and Simulations of Granular Flows using Discrete Element Method (DEM)

Dissertation

to obtain the academic degree of 'Doktor der technischen Wissenschaften' at the

Graz University of Technology

by Muhammad Shafiq Siraj, M.Sc.

Graz, March 2012

Institute for Process and Particle Engineering

Graz University of Technology

Graz, Austria

Candidate

Muhammad Shafiq Siraj

Dissertation

Modeling and Simulations of Granular Flows

using Discrete Element Method (DEM)

First assessor

Univ.-Prof. Dipl.-Ing. Dr.techn. Johannes Khinast

Head, Institute for Process and Particle Engineering

Scientific Director, Research Center Pharmaceutical Engineering GmbH

Graz University of Technology, Graz (Austria).

Second assessor

Ao. Univ.-Prof. Dipl.-Ing. Dr.techn. Rudolf Eichinger

Institute for Paper-, Pulp-, and Fiber Technology

Graz University of Technology, Graz (Austria).

Statutory Declaration

I declare that I have authored this thesis independently, that I have not used other than the declared sources / resources, and that I have explicitly marked all material which has been quoted either literally or by content from the used sources.

(Ich erkläre an Eides statt, dass ich die vorliegende Arbeit selbstständig verfasst, andere als die angegebenen Quellen/Hilfsmittel nicht benutzt, und die den benutzten Quellen wörtlich und inhaltlich entnommene Stellen als solche kenntlich gemacht habe.)

01 Feb, 2012 …………………………………………..

(Muhammad Shafiq Siraj, M.Sc.)

Dedicated to all those who devoted their lives for the betterment of humanity without getting acclaimed or rewarded

Acknowledgements

Kurzfassung

Das Verständnis von granularen Strömungen, granularem Mischen bzw. Pulvermischen steht bereits für viele Jahrzehnte im Mittelpunkt des Interesses der Bergbau-, der Chemie-, der Prozess-und der Pharmaindustrie, aufgrund der sich aus ihnen ergebenden zahlreichen Anwendungsmöglichkeiten.

Granulare Strömungen und granulares Mischen hängen von einer Reihe verschiedener Faktoren, wie z.B. von den verschiedenen Partikelkräften, ab, weshalb granulare Strömungen mit den zugrundeliegenden Mischphänomenen bis heute noch nicht ganz erforscht und verstanden sind.

Diese Dissertation wurde unter den oben genannten Aspekten gestartet: Um einen besseren Einblick in den Sachverhalt zu bekommen wurden verschiedene Bedingungen simuliert und der Einfluss von Materialeigenschaften, wie z.B. der Teilchendurchmesserverhältnisse, auf das Strömungs- und das Mischverhalten untersucht. Auch wurde die Auswirkung der Behältergeometrie durch die Verwendung von 2-D und 3-D Simulationsgeometrien als auch durch die Variation der Simulationsgitterlänge studiert.

Die Auswirkungen der internen Parameter, wie jener der Partikel-Wand Reibung, auf die Fließeigenschaften wurden ebenso untersucht wie die Auswirkungen von äußeren Parametern, wie Blattwinkel und Blattform., auf das granulare Strömungsverhalten. Zusätzlich wurden die Auswirkungen all dieser internen und externen Parameter auf die Mischblattkräfte und die interpartikulären Anpresskräfte untersucht.

Ein neuer Mischindex wurde zur Quantifizierung der Mischleistung körniger Strömungen formuliert. Die Auswirkungen der Partikelfüllstand oder Betthöhe auf granulare Mischung wurde ebenfalls untersucht.

Letztlich wurde die Mischleistungseffizienz bezüglich der Anzahl der Mischblattdurchläufe hin untersucht und eine mathematische Beziehung für die Anzahl der Mischblattdurchläufe, die Mischblattgeschwindigkeit und von der vom Mischblatt zurückgelegte Entfernung abgeleitet.

Abstract

The understanding of granular flows and granular mixing or powder blending has been a focus of interest for many decades due to bulk handling and processing of solid materials whether in mining, chemical, process, civil or pharmaceutical industry.

Granular flows and mixing are dependent on a number of different factors (e.g. on the behavior of different interparticle forces) and hence can be influenced in a number of ways. This dependence and influence by a number of factors leads to a lack of understanding of granular flows and underlying mixing phenomena, even today.

The dissertation was started keeping the same objective in mind. Rigorous mixing simulations were performed under different conditions. The studies were performed for the investigation of material characteristics like the effect of particle diameter ratios on granular flows and mixing in rectangular box geometries. The effects of container geometry on granular flows and mixing performance were also investigated by using 2-D and 3-D boxes and also by increasing the length of the simulation box.

The effects of internal parameters like particle-wall friction on flow characteristics and mixing were also investigated. Similarly, the effects of external parameters like blade angle and blade shape, etc., on granular flows and mixing were also investigated in this study.

A new mixing index was also formulated for the quantification of mixing performance for granular flow simulations. Effects of particle fill-level or bed-height on granular mixing were also investigated.

Additionally, the effects of all these internal and external parameters on blade force and interparticle contact forces were also investigated.

In the end, the effect of number of blade passes on mixing performance efficiency was also investigated and a mathematical relationship was derived in terms of number of blade passes, blade speed and distance covered by the blade.

Table of Contents

List of Tables

List of Figures

1 **Goals and Content Description**

Since granular flows and mixing are dependent on a number of different factors, e.g., on the behavior of different interparticle forces and some external factors, hence the granular flows can be influenced in a number of different ways.

The objective of this dissertation was to investigate the influence of different internal and external parameters on the granular flows and granular flow simulations.

The thesis contains the following chapters:

Chapter 2:

This chapter discusses in brief an introduction to granular flows and their dependence on different interparticle forces as well as other external factors. It also discusses mixing and industrial mixers briefly.

Chapter 3:

This chapter gives a detailed description of different numerical methods used in granular flows and simulations and description of mixing index derived and used in our studies.

Chapter 4:

This chapter discusses in detail the use of PASIMODO for different particle simulation at the start of the dissertation.

Chapter 5:

This chapter discusses in detail the effects of blade angle and particle size on powder mixing performance in a rectangular box.

Chapter 6:

This chapter discusses in detail the effect of the blade shape and angle on single-blade convective powder mixing using 2-D and 3-D simulation setup.

Chapter 7:

This chapter discusses in detail the effects of particle fill-level or bed-height variation and number of blade passes on powder mixing performance.

Chapter 8:

This chapter concludes the work done in this study and the future work that can be extended.

_____

2 Introduction

Granular flows and mixing phenomena are dependent on a number of different factors, and hence are/can be influenced by a number of ways. The dependence and influence by a number of factors leads to the lack of understanding of granular flows and underlying mixing phenomena even today.

2.1 Interparticle Forces

Granular flows and mixing phenomena are governed by a number of different interparticle forces listed in Fig. 2.1.
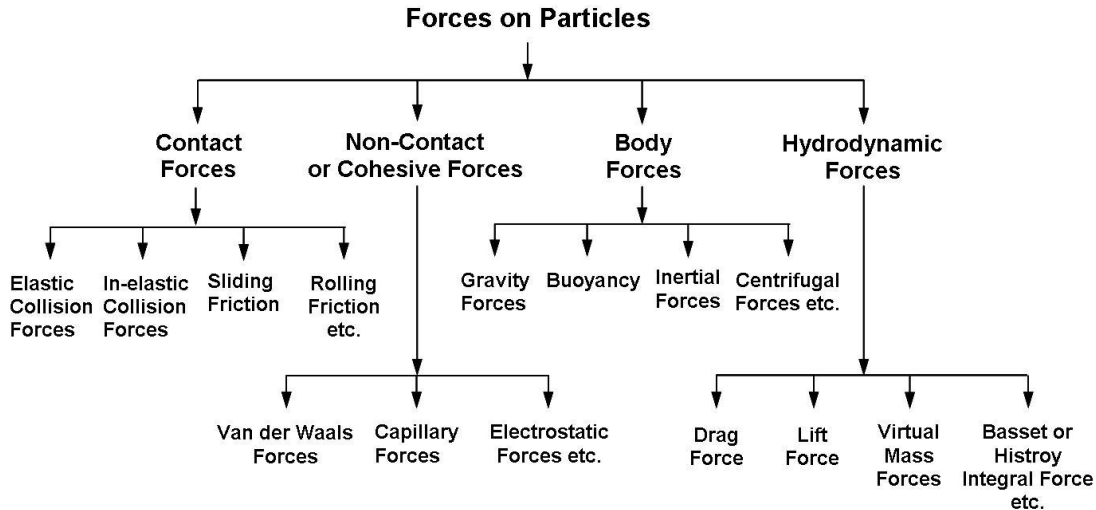
Figure 2.1. Different interparticle forces.

Therefore, due to these different interparticle forces, solid particle mixing depends on several parameters. Some of these parameters include the nature of the material of the particles, their size, shape, number and their loading/unloading profile.

Similarly, it is dependent on the size, shape, and material of the mixer and the blades, fill level or particle bed-height, position of the blade, its speed and acceleration. Additionally, solid particle mixing is also dependent on the presence of any external surfaces/obstacles, e.g., baffles and number of phases involved in the granular flows/mixing. In case of the presence of a liquid phase, the flow/mixing is further dependent on the nature of the fluid (Newtonian or non-Newtonian) and its physical conditions like viscosity, surface tension, temperature and pressure etc.

Because of the number of parameters involved, the mixing phenomenon becomes complicated to understand both numerically and experimentally, thus giving rise to its significance.

2.2 Granular flows

Cohesive granular flows are found in a wide variety of industrial and natural flows. For example, in the pharmaceutical industry, it is of paramount importance to understand the effects of various process parameters on the final product performance, which often is a function of granular mixing, compression, coating and other particle-based methods. In addition, maintaining the right dosage and coating uniformity is a challenge for the pharmaceutical industry.

Therefore, in this work we mainly focus on the analyses of mixing mechanisms. Current state-of-the-art does not allow as of yet a detailed investigation of complex, cohesive granular flows, as no universal constitutive equations exist similar to Newton's and Navier-Stokes' equations for fluids.

However, the major flow regimes in granular mixing can be identified and represented as shown in Fig. 2.2.
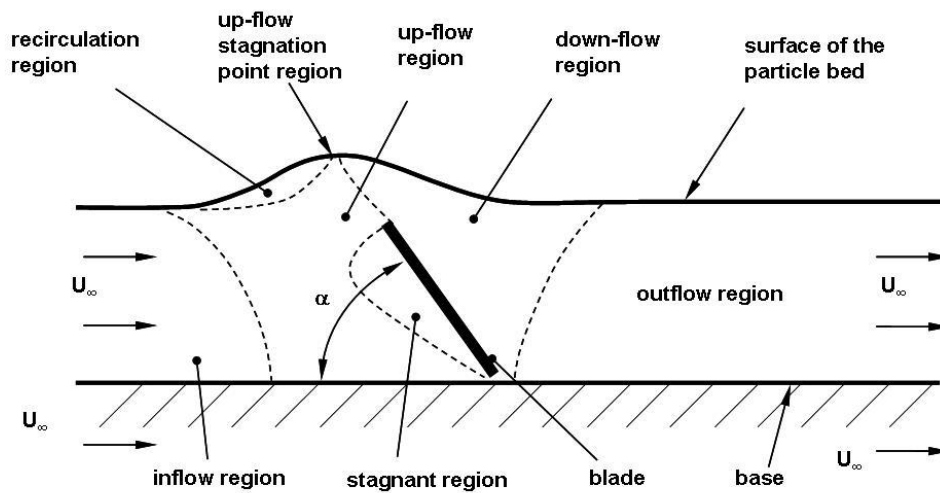
Figure 2.2. Schematic representation of the flow regions over a blade (adapted from Bagster and Bridgewater, 1967).

Previous studies show the high complexity of the flow in convective mixers including multiple recirculation zones, for example by Stewart et al. [1], as well as anisotropic velocity fluctuations by Radl et al. [2].

_____

Rotating internals force the granular material to flow over the barrier, i.e., blade. Fig. 2.2 explains some typical features of the flow over a single blade. In principle, the flow is similar to a fluid flowing over a weir. This analogy with fluid flow has not been fully explored in the previous works. Thus, the objective was to develop a flow map using the well-accepted Froude number which is a key non-dimensional quantity in the fluid flow over weirs. Similar regimes were observed experimentally in the flow of water in weir fishways, a study by Ead et al. [3].

2.3 Mixing and Industrial Mixers

Different types of industrial mixers are employed for solid particle mixing particularly in the pharmaceutical industry due to strict controls on the quantities of active pharmaceutical ingredients (APIs) in the final dosage form. Convective mixers are the most important ones used for this purpose. Continuous mixers like ribbon blenders and batch mixers like vertical cylindrical mixers with two or four blades are typical examples of convective mixers.

In general, according to Lacey [4], there are three types of mixing mechanisms:

- Convective mixing based on the movement of a large group of particles. The rate of mixing is high in this case.

- Diffusive mixing based on random movement of solid particles (sometimes expressed by the granular temperature). The mixing rate is slow compared to convective mixing.

- Shear mixing based on the development of slip failure planes in the powder mixture, e.g., when a chunk of powder slips down along the slip plane.

Shear mixing can occur in convective and high-shear mixers and also in tumbling mixers where a layer of powder mixture avalanches down along a slope plane [5]. Convective and shear mixing is difficult to distinguish [6] in dense particle systems and can be collectively termed as convective-shear mixing.

A tumbling mixer is defined as any closed vessel rotating about its axis. It typically consists of a double cone or v-shape and is normally half-filled to allow particles

to move randomly and to slide or roll down along a sloping surface. Because of low shearing this mixer may not be quite effective for cohesive powders and powder materials that tend to segregate. A convective mixer consists of a static vessel and rotating blades and paddles or screws that allow particles to rotate in the static mixer vessel, thus inducing convective and shear mixing [7]. In a convective batch mixer the predominant modes of mixing are convective and shear mixing. The scale-up of both mixer types, however, is not straightforward, albeit for different reasons.

Convective bladed mixers have been investigated more in detail using both experimental and simulation techniques [8-17] as compared to tumbling batch mixers. A number of publications have appeared recently in the literature employing a convective batch mixer with two [8-9, 14-15, 17] or four [10-13, 16] blades. These bladed mixers have been studied using experimental [8, 10], simulations [11-12, 14-17], and by comparing results using both [9, 13] techniques. Stewart et al. [8] investigated granular flow over a flat bladed stirrer using positron emission particle tracking and observed three-dimensional recirculation zones; they also observed a linear variation of particle speed with the speed of blade. In addition, they also observed that the size of the recirculation zones and the number of blade passes that the particles spend in these zones decreased with the increase in fill level and blade speed. In their second paper [9], they compared their experimental results with the simulation results. Conway et al. [10] used particle image velocimetry (PIV) technique to study velocity fields near top and the wall for near-monodisperse and polydisperse granular materials. They also observed the three-dimensional recirculating zones and also studied mixing and segregation with respect to shear rates. Remy et al. [11] investigated the effect of blade orientation on particle flow patterns and mixing kinetics using DEM simulations. They also investigated the effects of friction coefficients on mixing and, in addition, studied normal and shear stresses and their dependence on mixer height and friction coefficients of particles. In their second paper [12], Remy et al. investigated the effects of fill level and mixer properties (vertical blade position from bottom, wall friction, mixer diameter, and blade speed) on granular flow characteristics and on mixing. In another paper [13], Remy et al. investigated, experimentally and using simulations, the effects of varying roughness on granular flow of cohesionless particles, in addition to the effects of varying blade speed. Zhou et al. [14] investigated the effects of blade speed, particle size, volume fraction, and

particle density on the segregation of binary mixtures. In another paper [15], Zhou et al. investigated the microdynamic analysis of the particle flow especially the effects of sliding and rolling friction coefficients on the promotion of three-dimensional recirculating particle zones. Radl et al. [16] investigated the mixing characteristics of wet granular matter and observed better mixing rates and performance as compared to dry granular matter under same conditions.

Some publications have also reported two-dimensional flow over a flat blade in a horizontal cylinder, e.g., Malhotra et al. [18]; and have also studied flow using paddle type blades [19-21] by taking photographs. They observed difference in flow in the main bed and the flow at the end wall. Laurent et al. [22] also used a single blade to observe the motion in a particle bed using positron emission particle tracking.

In a recent paper [17], blade rake angle for 3-D mixer system was investigated using three angles 45°, 90°, and 135°. The mixing performance in this work was quantified using Lacey's mixing index, and 90° was reported as the angle showing fastest mixing rate. In this work, however, although mixing was done in a convective batch mixer but the geometry used was different than any other convective batch mixers that have been used until now. In this case, a simple 3D rectangular box was used with a single blade to allow the movement of the blade only in x-dir and thus understanding of the mixing phenomenon at the very basic level without involving the complex mixer geometries.

2.4 References

[1]   R.L. Stewart, J. Bridgwater, D.J. Parker, Granular flow over a flat-bladed stirrer. Chemical Engineering Science 56 (2001) 4257-4271.

[2]   S. Radl, E. Kalvoda, B.J. Glasser, J.G. Khinast, Mixing characteristics of wet granular matter in a bladed mixer. Powder Technology 200 (2010) 171-189.

[3]   S.A. Ead, C. Katopodis, G.J. Sikora, N. Rajaratnam, Flow regimes and structure in pool and weir fishways. Journal of Environmental Engineering and Science 3 (2004) 379-390.

[4]   P.M.C. Lacey, Developments in the theory of particle mixing. Journal of Applied Chemistry 4 (1954) 257–268.

[5]   P.J. Cullen, Food Mixing: Principles and Applications. New York, Wiley-Blackwell (2009).

[6]   J. Bridgwater, Fundamental powder mixing mechanisms. Powder Technology 15 (1976) 215-236.

[7]   P.M. Portillo, M.G. **Ierapetritou, F.J. Muzzio,** Characterization of continuous convective powder mixing processes. Powder Technology 182 (2008) 368-378.

[8]   R.L. Stewart, J. Bridgwater, D.J. Parker, Granular flow over a flat-bladed stirrer. Chemical Engineering Science 56 (2001) 4257-4271.

[9]   R.L. Stewart, J. Bridgwater, Y.C. Zhou, A.B. Yu, Simulated and measured flow of granules in a bladed mixer - a detailed comparison. Chemical Engineering Science 56 (2001) 5457-5471.

[10]   S.L. Conway, A. Lekhal, J.G. Khinast, B.J. Glasser, Granular flow and segregation in a four-bladed mixer. Chemical Engineering Science 60 (2005) 7091-7107.

[11]   B. Remy, J.G. Khinast, B.J. Glasser, Discrete element simulation of free flowing grains in a four-bladed mixer. AIChE Journal 55 (2009) 2035-2048.

[12]   B. Remy, J.G. Khinast, B.J. Glasser, The effect of mixer properties and fill level on granular flow in a bladed mixer. AIChE Journal 56 (2009) 336-353.

[13]   B. Remy, T.M. Canty, J.G. Khinast, B.J. Glasser, Experiments and simulations of cohesionless particles with varying roughness in a bladed mixer. Chemical Engineering Science 65 (2010) 4557-4571.

[14]   Y.C Zhou, A.B. Yu, J. Bridgwater, Segregation of binary mixture of particles in a bladed mixer. Journal of Chemical Technology and Biotechnology 78 (2003) 187-193.

[15]   Y.C. Zhou, A.B. Yu, R.L. Stewart, J. Bridgwater, Microdynamic analysis of the particle flow in a cylindrical bladed mixer. Chemical Engineering Science 59 (2004) 1343-1364.

_____

[16]   S. Radl, E. Kalvoda, B.J. Glasser, J.G. Khinast, Mixing characteristics of wet granular matter in a bladed mixer. Powder Technology 200 (2010) 171-189.

[17]   G.R. Chandratilleke, A.B. Yu, R.L. Stewart, J. Bridgwater, Effects of blade-rake angle and gap on particle mixing in a cylindrical mixer. Powder Technology 193 (2009) 303-311.

[18]   K. Malhotra, A.S. Mujumdar, H. Imakoma, M. Okazaki, Fundamental particle mixing studies in an agitated bed of granular materials in a cylindrical vessel. Powder Technology 55 (1988) 107-114.

[19]   K. Malhotra, A.S. Mujumdar, Particle mixing and solids flowability in granular beds stirred by paddle-type blades. Powder Technology 61 (1990) 155-164.

[20]   K. Malhotra, A.S. Mujumdar, M. Miyahara, Estimation of particle renewal rates along the wall in a mechanically stirred granular bed. Chemical Engineering and Processing 27 (1990) 121-130.

[21]   K. Malhotra, A.S. Mujumdar, M. Okazaki, Particle flow patterns in a mechanically stirred two-dimensional cylindrical vessel. Powder Technology 60 (1990) 179-189.

[22]   B.F.C. Laurent, J. Bridgwater, D.J. Parker, Motion in a particle bed agitated by a single blade. AIChE Journal 46 (2000) 1723-1734.

3 Numerical Methods

In this study, both numerical and experimental techniques were used to investigate the flow of granular materials. Numerical techniques were based on the discrete element method (DEM) and experimental on using a novel experimental setup employing a rectangular box geometry.

Keywords: DEM, mixing, mixing index, GMMI, MGMMI, EDEM

3.1 Numerical Models

Our simulations were based on the DEM which is a powerful tool for granular flow simulations as it gives a detailed picture of the floe and mixing by keeping track of each individual particle discretely. In discrete element method (DEM), every particle is treated in a discrete manner and is solved for all the forces acting on it including contact forces, body forces, hydrodynamic forces and cohesive forces. These forces are then integrated over time to get position and velocity of each individual particle.

In DEM, the most important parameter to determine in mixing simulations is position and velocity of all particles after certain time. According to Newton's second law of motion the position of particle i is:

$$m_i \frac{d^2 \vec{x_i}}{dt^2} = \vec{F}_{total,i} = \sum \vec{F}_{cont,ij} + \sum \vec{F}_{n-cont,ik} + \vec{F}_{g,i} + \vec{F}_{drag,i} \qquad (3.1)$$

$$I_i \frac{d\vec{\omega_i}}{dt} = \sum_j \vec{M}_{ij} \qquad (3.2)$$

Where m_i is the mass of the particle i and x_i is the position. This equation can be integrated to get velocity, and double integration gives position of the particle i in x, y, and z-coordinate system. $\vec{F}_{total,i}$ is the sum of all the forces acting on particle i by the colliding particle j or walls or other particles namely;

- $\sum \vec{F}_{cont,ij}$ is the contact force,

- $\sum F_{n-cont,ik}$ is the force other than contact force e.g. van der Waals, electrostatic, and liquid bridge forces etc.,

- $\vec{F}_{drag,i}$ is the force exerted by surrounding fluid i.e. drag (fluid is air in case of solid mixing so the drag in our case was ignored as it is negligible in comparison to contact and other forces),

- $\vec{F}_{g,i}$ is the gravitational force exerted on the particle i.

In Eq. 3.2, I_i is the moment of inertia, ω_i is the angular velocity, and $\overrightarrow{M}_{ij}$ is the torque acting on particle i by particle j.

The resultant equation in our solid mixing case from Eq. 3.1 would be

$$m_i \frac{d^2 \overrightarrow{x}_i}{dt^2} = \sum \overrightarrow{F}_{cont,ij} + \sum \overrightarrow{F}_{n-cont,ik} + \overrightarrow{F}_{g,i} \tag{3.3}$$

Different numerical schemes are available that can be used to solve these two equations for each particle and at each time step. The first term on right hand side of Eq. 3.3, i.e., the contact force is the most important part comprising normal and tangential force components and lot of models have been proposed to account for this term (Zhu et al. [1]):

1. Linear spring-dashpot model by Cundall and Strack [2].

   - Normal force,

   $$\overrightarrow{F}_n = -K_n \delta_n \hat{n}_c - C_n (\overrightarrow{v}_c . \hat{n}_c) \hat{n}_c \tag{3.4}$$

   - Tangential force,

   $$\overrightarrow{F}_t = -K_t \overrightarrow{v}_c^t + C_t (\overrightarrow{v}_c \times \hat{n}_c) \times \hat{n}_c \tag{3.5}$$

2. Simplified Hertz-Mindlin and Deresiewicz model by Langston et al. [3-5], Zhou et al. [6], and Zhu and Yu [7].

   - Normal force

   $$F_n = -\frac{4}{3} E^* \sqrt{R^*} (\delta_n)^{3/2} - C_n (8m^* E^* \sqrt{R^* \delta_n})^{1/2} . (\overrightarrow{v}_c . \hat{n}_c) \hat{n}_c \tag{3.6}$$

   - Tangential force

   $$\begin{aligned} \overrightarrow{F}_t = &-\mu |\overrightarrow{F}_{n,e}| (1 - (1 - |\overrightarrow{v}_c^t| / \delta_{max})^{3/2}) \hat{v}_c^t \\ &+ 2C_t (1.5\mu m^* |\overrightarrow{F}_{n,e}| . \sqrt{1 - |\overrightarrow{v}_c^t| / \delta_{max}} / \delta_{max})^{1/2} . (\overrightarrow{v}_c \times \hat{n}_c) \times \hat{n}_c \end{aligned} \tag{3.7}$$

3. Walton and Braun's model by Walton and Braun [8], and Walton [9].

- Normal force

$$\vec{F}_n = -k_1 \delta_n \hat{n}_c, \dot{\delta}_n \geq 0 \text{ (for loading)} \tag{3.8}$$

and

$$\vec{F}_n = -k_2 (\delta_n - \delta_{n0}) \hat{n}_c, \dot{\delta}_n < 0 \text{ (for unloading)} \tag{3.9}$$

- Tangential force

$$\vec{F}_t = \vec{F'}_t + k_t^0 \left(1 - \left(1 - \frac{\vec{F}_t - \vec{F}_t^*}{\mu \vec{F}_n - \vec{F}_t^*}\right)^{1/3}\right) \Delta \vec{v}_c^t \tag{3.10}$$

if $\vec{v}_c^t$ is in initial direction and

$$\vec{F}_t = \vec{F'}_t + k_t^0 \left(1 - \left(1 - \frac{\vec{F}_t^* - \vec{F}_t}{\mu \vec{F}_n - \vec{F}_t^*}\right)^{1/3}\right) \Delta \vec{v}_c^t \tag{3.11}$$

if $\vec{v}_c^t$ is in opposite direction.

4. Similarly some torque models are summarized (Zhu et al. [1]) as:

- In first method (Iwashita and Oda, [10-11]), the rolling friction torque is

  calculated as $\vec{m}_r = -k_r \vec{\theta}_r - C_r \dfrac{d\vec{\theta}_r}{dt}$ whereas torque from tangential forces

  is calculated as $\vec{m}_t = \vec{R} \times \vec{F}_t$.

- In second model, rolling friction torque is calculated [12-13] as:

  $$m_r = -\min(\mu_r | \vec{F}_n | \mu'_r | \vec{\omega}_n |) \hat{\omega}_n$$

Following basic steps are involved in all DEM simulations (Siraj et al. [14]);

1. Collision detection through particle-particle and particle-wall contacts/overlaps.

2. Application and calculation of contact forces to all collisions.

3. Calculation of other forces, body (gravitational) and hydrodynamic (fluid drag) for all particles but fluid drag by air was neglected in this work.

4. Calculation of particles' translational and rotational acceleration after calculation of unknown forces in equations 3.1 and 3.2.

5. Integration of these accelerations numerically to find particles' new positions and velocities.

The major disadvantage for most DEM simulations is increased computational time and cost despite the availability of modern multi-core computers. Another disadvantage is the representation of the true shape of the particles and some other forces e.g. hydrodynamic forces which are ignored for the sake of simplicity although they may not have a significant effect on overall mixing for dense particulate systems.

3.2 Software

PASIMODO and EDEM were used for the study of granular flow simulations. PASIMODO is an academic software developed at the University of Stuttgart, Germany and stands for **PA**rticle **SI**mulation and **MO**lecular **D**ynamics, in an **O**bject oriented fashion. EDEM, on the other hand, is commercial software developed by DEM Solutions Inc.

3.3 Mixing Index

For the mixing calculations, mixing indices need to be established in order to quantify the mixing process. In this work, the mixing index was based on Generalized Mean Mixing Index, GMMI [15]. However, GMMI was modified after some limitations were encountered and some errors were detected under certain conditions in some cases.

If there are two types of particles, *a* and *b*, then the GMMI of *a*-type particles, i.e., $GMMI_a$, is calculated [15] as the sum of the mean positions of *n* *a*-type particles

divided by the sum of the mean positions of all N particles of $a+b$ type. GMMI$_a$ is

calculated in x, y, or z directions depending on whether positions x, y or z are used. The

total GMMI is then:

$$GMMI_a = (GMMIx_a + GMMIy_a + GMMIz_a)/3 \qquad (3.12a)$$

where

$$GMMIx_a = \frac{\left[\sum_{p=1}^{n}\frac{(x_p - x_{ref})}{n}\right]}{\left[\sum_{q=1}^{N}\frac{(x_q - x_{ref})}{N}\right]} \quad GMMIy_a = \frac{\left[\sum_{p=1}^{n}\frac{(y_p - y_{ref})}{n}\right]}{\left[\sum_{q=1}^{N}\frac{(y_q - y_{ref})}{N}\right]} \quad GMMIz_a = \frac{\left[\sum_{p=1}^{n}\frac{(z_p - z_{ref})}{n}\right]}{\left[\sum_{q=1}^{N}\frac{(z_q - z_{ref})}{N}\right]}$$

Here x_{ref}, y_{ref}, and z_{ref} are the reference positions in x, y and z directions and were

zero in our box case. It can best be illustrated by an example analogous to our

simulations (Fig. 1). GMMI for this example is:

$$GMMI_{blue} = (GMMIx_{blue} + GMMIy_{blue} + GMMIz_{blue})/3 \qquad (3.12b)$$

Where

$$GMMIx_{blue} = \frac{\left[\sum_{p=1}^{5}\frac{x_p}{5}\right]}{\left[\sum_{q=1}^{10}\frac{x_q}{10}\right]} \quad GMMIy_{blue} = \frac{\left[\sum_{p=1}^{5}\frac{y_p}{5}\right]}{\left[\sum_{q=1}^{10}\frac{y_q}{10}\right]} \quad GMMIz_{blue} = \frac{\left[\sum_{p=1}^{5}\frac{z_p}{5}\right]}{\left[\sum_{q=1}^{10}\frac{z_q}{10}\right]}$$

3.3.1 Development of a New Mixing Index for DEM Simulations

The problem with GMMI was detected in Equations 3.12a and 3.12b when all

three GMMI values in x, y, and z directions are averaged out. Some values for example

in z-dir could be greater than 1.0 whereas other GMMI values in x and y directions may

be less than 1.0 with the ideal mixing value of 1.0 in between. In this case, therefore, the

averaged value does not represent a true value and the error was observed in some of our simulation cases. It can better be explained with an example. In our case, blue (top) and red (bottom) particles were used. If we break-up the individual GMMI values for this example then:

$$GMMIx_{blue} = \frac{(x.pos)_{mean,blue}}{(x.pos)_{mean,all}} = \frac{(x.pos)_{mean,blue}}{\dfrac{(x.pos)_{mean,blue} + (x.pos)_{mean,red}}{2}} = \frac{1}{0.5 + 0.5\left[\dfrac{(x.pos)_{mean,red}}{(x.pos)_{mean,blue}}\right]} \quad (3.13a)$$

If mean x-pos of red particles is greater than that of blue particles, meaning more red particles are towards right-side of the box compared to blue particles thus $GMMIx_{blue}$ will be less than 1.0.

Similarly in z-direction:

$$GMMIz_{blue} = \frac{(z.pos)_{mean,blue}}{(z.pos)_{mean,all}} = \frac{(z.pos)_{mean,blue}}{\dfrac{(z.pos)_{mean,blue} + (z.pos)_{mean,red}}{2}} = \frac{1}{0.5 + 0.5\left[\dfrac{(z.pos)_{mean,red}}{(z.pos)_{mean,blue}}\right]} \quad (3.13b)$$

Since blue particles, for example, in our simulations were on top so the $GMMIz_{blue}$ is greater than 1.0, also evident from Eq. 3.13b. Hence, considering the ideal mixing value of 1.0 and averaging out in such cases where some values are less than 1.0 and some greater than 1.0, gives false results. GMMI, however, is valid when all three GMMI values in x, y and z directions are either less than 1.0 or greater than 1.0.

The method was modified and for all three GMMI values, i.e., GMMIx, GMMIy, and GMMIz. This gave rise to the modified generalized mean mixing index (MGMMI). In this case, no MGMMI value is greater than the ideal mixing value of 1.0 and thus causing no confusion between mixing and segregation values.

$$MGMMI = 1 - \frac{abs(1 - GMMIx_a) + abs(1 - GMMIy_a) + abs(1 - GMMMIz_a)}{3}$$

(3.14)

A value of MGMMI=1 indicates that a binary mixture is perfectly mixed. MGMMI has several advantages [15]:

1. It is precise and easy to implement for DEM simulations.

2. It is fast to evaluate.

3. It uses a physical property, i.e., the position of all particles, and does not depend on sampling.

4. It does not depend on a sample size.

5. It is not limited to only binary mixtures as other mixing indices.

6. It indicates mixing, as well as segregation.

Thus, MGMMI is used in this work to quantify the effect of mixing.

3.4 Nomenclature

C_n normal damping coefficient (kg-s^{-1})

C_t tangential damping coefficient (kg-s^{-1})

C_r viscosity coefficient (-)

E^* reduced Young's modulus (-)

$\vec{F}$ force (N)

$\vec{F}_{cont,ij}$ contact force between particle i and j (N)

$\vec{F}_{drag,i}$ drag force on particle i (N)

$\vec{F}_{g,i}$ gravitational force on particle i (N)

$\vec{F}_{n}$ normal force (N)

$\vec{F}_{n-cont,ik}$ non-contact force on particle i by other particle k (N)

$\vec{F}_{t}$ tangential force (N)

$\vec{F}_{total,i}$ total force on particle i (N)

I_i moment of inertia (kg-m^2)

k_1 spring constant for loading (-)

k_2 spring constant for unloading (-)

k_t^0 initial tangential stiffness (N-m^{-1})

k_r rolling stiffness (N-m^{-1})

K_n normal spring coefficient (-)

m   mass (kg)

m^* reduced particle mass (-)

$\vec{m}_r$ rolling friction torque (Nm)

$\vec{M}_{ij}$ torque (Nm)

N   No. of particles

n   numbers (1,2,3,…….,n)

_____

$\hat{n}_c$ unit normal vector at contact point (-)

$\vec{R}$ vector of the mass center of the particle to contact plane (m)

R^* reduced particle radius (-)

t   time (s)

Δt time difference (s)

$\vec{v}_c$ relative velocity of the two particles at their contact point (m-s^{-1})

$\vec{v}_c^t$ relative tangential displacement at contact (m)

$\vec{x}$ position in x-direction (m)

Δx displacement (m)

x, y, z position of a particle in x, y, or z direction (m)

$x_{ref}, y_{ref}, z_{ref}$ reference position in x, y, or z directions (m)

Greek Letters

δ_n relative normal displacement at contact (m)

δ_{max} maximum relative tangential displacement when particle starts sliding (m)

$\vec{\theta}_r$ relative particle rotation (-)

μ friction coefficient (-)

μ_r rolling friction coefficient (-)

μ_r' rotational stiffness (Nm)

ρ_p particle density (kg-m^{-3})

$\vec{\omega}_i$ angular velocity (s^{-1})

$\vec{\omega}_n$ relative angular velocity component in the contact plane (s^{-1})

$\hat{\omega}_n$ unit vector of $\vec{\omega}_n$ (s^{-1})

Subscripts

d   drag

e   elastic

g   gravitational

i   particle i

j   particle j

n   normal

t   tangential

3.5 References

[1] H.P. Zhu, Z.Y. Zhou, R.Y. Yang, A.B. Yu, Discrete particle simulation of particulate systems: Theoretical developments. Chemical Engineering Science 62 (2007) 3378-3396.

[2] P.A. Cundall, O.D.L. Strack, Discrete Numerical-Model for Granular Assemblies. Geotechnique 29 (1979) 47-65.

[3] P.A. Langston, U. Tüzün, D.M. Heyes, Continuous potential discrete particle simulations of stress and velocity fields in hoppers: transition from fluid to granular flow. Chemical Engineering Science 49 (1994) 1259-1275.

[4]   P.A. Langston, U. Tüzün, D.M. Heyes, Discrete element simulation of granular flow in 2D and 3D hoppers: dependence of discharge rate and wall stress on particle interactions. Chemical Engineering Science 50 (1995) 967-987.

[5]   P.A. Langston, U. Tüzün, D.M. Heyes, Discrete element simulation of internal stress and flow fields in funnel flow hoppers. Powder Technology 85 (1995) 153-169.

[6]   Y.C. Zhou, B.D. Wright, R.Y. Yang, B.H. Xu, A.B. Yu, Rolling friction in the dynamic simulation of sandpile formation. Physica A 269 (1999) 536-553.

[7]   H.P. Zhu, A.B. Yu, Averaging method of granular materials. Physical Review E 66 (2002) 1-10.

[8]   O.R. Walton, R.L. Braun, Viscosity, Antigranulocytes-Temperature, and Stress Calculations for Shearing Assemblies of Inelastic, Frictional Disks. Journal of Rheology 30 (1986) 949-980.

[9]   O.R. Walton, Numerical simulation of inclined chute flows of monodisperse inelastic, frictional spheres. Mechanics of Materials 16 (1993) 239-247.

[10]   K. Iwashita, M. Oda, Rolling resistance at contacts in simulation of shear band development by DEM. Journal of Engineering Mechanics - ASCE 124 (1998) 285-292.

[11]   K. Iwashita, M. Oda, Micro-deformation mechanism of shear banding process based on modified distinct element method. Powder Technology 109 (2000) 192-205.

[12]   Y.C. Zhou, B.D. Wright, R.Y. Yang, B.H. Xu, A.B. Yu, Rolling friction in the dynamic simulation of sandpile formation. Physica A 269 (1999) 536-553.

[13]   H.P. Zhu, A.B. Yu, Averaging method of granular materials. Physical Review E 66 (2002) 1-10.

[14]   M.S. Siraj, S. Radl, B.J. Glasser, J.G. Khinast, Effect of Blade Angle and Particle Size on Powder Mixing Performance in a Rectangular Box. Powder Technology 211 (2011) 100-113.

[15] B.N. Asmar, P.A. Langston, A.J. Matchett, A generalized mixing index in distinct element method simulation of vibrated particulate beds. Granular Matter 4 (2002) 129-138.

4 Validation of experimental Results of Particle-Wall Collision Interaction for Glass using PASIMODO

To understand and validate the particle-particle, particle-wall interaction and mixing using DEM, the best approach is to start with a few particles and then extend the results based on these understanding/findings. The same approach was adopted in this work. The particle-wall interaction was studied and the results were compared with the experimental results for the same case under the same physical conditions. After setting up the correct parameters, the work was extended to particles of other materials. In this work some very important parameters were corrected because these parameters are limited not only to just PASIMODO but all other simulation software using linear spring-dashpot model.

Keywords: Particle, DEM, normal force, tangential force, collision, friction

_____

4.1 Introduction:

Particles handling and mixing is as old as human history itself but the real phenomenon on the other hand has not been understood well. Mixing phenomenon is simple and complicated at the same time. It is simple as it does not involve a complicated process or high tech equipment but at the same time difficult to understand due to lack of understanding of the physical behavior. The scale-up is also a big issue even if it is well understood in a small experimental setup.

Historically, different types of mixers have come up in the market mostly from hit and trial and from post modifications in the design through experience gained in the mixing. But as pressure for cost minimization is increasing on all industries, mixing industry cannot be an exception, thus leading to more automation and understanding of the process using simulation.

Mixing depends on several parameters, nature of the material of the particles which are to be mixed, their size, shape, number, their loading/unloading profile, and size, shape, and material of the mixer, likewise size, shape and material of the blades, fill level, position of the blade, its speed, and acceleration, any external surfaces/obstacles present e.g. baffles, phases involved, nature of the fluid (Newtonian or non-Newtonian) and its physical conditions like viscosity, surface tension, temperature, pressure etc.

Because of the number of parameters involved, the mixing phenomenon becomes complicated to understand both experimentally and using simulation thus giving rise to its significance.

The discrete element method (DEM) gives a detailed picture of mixing insight as it keeps track of each discrete particle. The disadvantage for most of the DEM simulations is that they require huge computational time and cost despite the availability of modern day multi-core computational machines. Another disadvantage is true representation of surface and some forces which are ignored for the sake of simplicity e.g. hydrodynamic forces although they do not have a significant effect on overall mixing for dense particulate solids.

In this work, first the simulation results were validated using a small number of 25 particles and then compared with the experimental results by Lorenz et al. [1]. Later

part of the work focused mostly on correct use of input parameters as they are used in all simulation softwares using DEM and last part of the work consisted of extension of these results to other materials besides glass.

4.2 Numerical Method:

4.2.1 Discrete Element Method (DEM)

In discrete element method (DEM), every particle is treated in discrete manner and solved for all the forces acting on it including contact forces, body forces, and cohesion forces etc. these forces are then integrated over time in the three coordinate system, updated at each time step to get the latest position, velocity, and forces we are interested in.

In DEM, the most important parameter to determine mixing simulations is position and velocity of all particles after certain time. According to Newton's second law of motion the position of particle i is:

$$m_i \frac{d^2 \vec{x}_i}{dt^2} = \vec{F}_{total,i} = \sum \vec{F}_{cont,ij} + \sum \vec{F}_{n-cont,ik} + \vec{F}_{g,i} + \vec{F}_{drag,i} \qquad (4.1)$$

$$I_i \frac{d\vec{\omega}_i}{dt} = \sum_j \vec{M}_{ij} \qquad (4.2)$$

Where m_i is the mass of the particle i and x_i is the position. This equation can be integrated to get velocity, and double integration gives position of the particle i in x, y, and z-coordinate system. $\vec{F}_{total,i}$ is the sum of all the forces acting on particle i by the colliding particle j or walls or other particles namely;

- $\sum \vec{F}_{cont,ij}$ is the contact force,
- $\sum F_{n-cont,ik}$ is the force other than contact force e.g. van der Waals, electrostatic, and liquid bridge forces etc.,
- $\vec{F}_{drag,i}$ is the force exerted by surrounding fluid i.e. drag (fluid is air in case of solid mixing so the drag in our case was ignored as it is negligible in comparison to contact and other forces),

- $\vec{F}_{g,i}$ is the gravitational force exerted on the particle i.

In Eq. 4.2, I_i is the moment of inertia, ω_i is the angular velocity, and $\vec{M}_{ij}$ is the torque acting on particle i by particle j.

The resultant equation in our solid mixing case from Eq. 4.1 would be

$$m_i \frac{d^2 \vec{x}_i}{dt^2} = \sum \vec{F}_{cont,ij} + \sum \vec{F}_{n-cont,ik} + \vec{F}_{g,i} \qquad (4.3)$$

Different numerical schemes are available that can be used to solve these two equations for each particle and at each time step. The first term on right hand side of Eq. 4.3, i.e., contact force is the most important part comprising normal and tangential force components and lot of models have been proposed to account for this term (Zhu et al. [2]):

Following basic steps are involved in all DEM simulations (Siraj et al. [3]) as discussed in chapter on Introduction:

1. Collision detection through particle-particle and particle-wall contacts/overlaps.
2. Application and calculation of contact forces to all collisions.
3. Calculation of other forces, body (gravitational) and hydrodynamic (fluid drag) for all particles but fluid drag by air was neglected in this work.
4. After calculation of unknown forces in equations 4.1 and 4.2, calculation of particles' translational and rotational acceleration.
5. Integration of these accelerations numerically to find particles' new positions and velocities.

4.2.2 Linear Spring-Dashpot Model

In our simulation studies spring-dashpot model was used. The simulation software was PASIMODO which is an academic particle-simulation software developed at the University of Stuttgart, Germany.

Linear spring-dashpot model is the simplest model to calculate accurately the contact forces for particle-particle and particle-wall collisions, the same model was used

_____

for DEM calculations by Cundall and Strack [3]. The model assimilates the contact forces calculation in particle-particle and particle-wall collisions in terms of:

- an elastic spring storing and then releasing the energy during the collision in the form of rebound and,

- a dashpot which accounts for the dissipation of the energy in a collision, the energy which is lost.
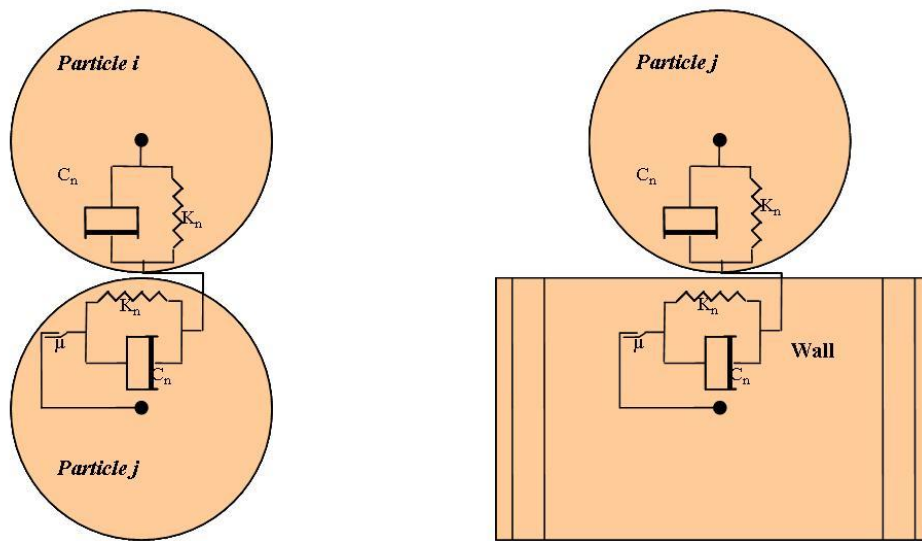
Figure 4.1. left: spring-dashpot model for particle-particle interaction, right: spring-dashpot model for particle-wall interaction.

In this figure (Fig. 4.1) adopted from Muguruma et al. [5], the frictional force in not accounted for which is always present in a collision and plays an important role in calculation of contact force calculation in Eq. 4.1.

Frictional forces are an important part of spring-dashpot model but unfortunately there are two methods for the calculation of these forces, global and complex models (Dziugys and Peters [6]). Global models as clear from the name use one law to model the tangential force whereas complex models use multiple equations for the modeling of different parts of the tangential force.

_____

4.3 Simulations

4.3.1 Software – PASIMODO

The simulations were performed using an academic software, PASIMODO developed at the University of Stuttgart. PASIMODO stands for **PA**rticle **SI**mulation and **MO**lecular **D**ynamics in an **O**bject oriented fashion. Details about this software can be found at the University of Stuttgart's website [7].

Our Institute (Institute for Process and Particle Engineering) has an official access to the software and some improvements were done in the code and overall working of the software.

4.3.2 Parameters

In any simulation, parameters and their determination is important as they serve as the input for simulation in the form of coefficients of modeling equations. The beads used were of glass and the parameters used are listed in Table 4.1 and Table 4.2.

Table 4.1. Parameters for sphere-triangle interactions.

Parameter	Value	Units
Maximum velocity in the system ($\vec{v}_{max}$)	3	m/s
Particle Diameter (d_p)	0.003	m
Particle Density (ρ_p)	2500	kg/m³
Normal Coefficient of Restitution (COR_n)	0.700	-
Tangential Coefficient of Restitution (COR_t)	0.250	-
Percentage for Overlap (f)	1.0%	-
Time Steps per Contact (n_t)	50	-
Poisson Ratio (ν for glass 0.18 to 0.30, avg=0.24)	0.24	-
Mass of Particle (m) = $\dfrac{4}{3}\pi r^3 \rho_p$	3.53×10^{-5}	kg
Normal Stiffness Coefficient, $K_n = \dfrac{1}{f^2}\dfrac{m\vec{v}_{max}^2}{r^2}$	1.41×10^6	N/m

Parameter	Value	Units
Normal Damping Coefficient, $C_n = \sqrt{\dfrac{4K_n m}{\left(\dfrac{\pi^2}{\ln^2(COR_n)}+1\right)}}$	1.5948	kg/s
Tangential Stiffness Coefficient, $K_t = \dfrac{[\alpha \cos^2(COR_t)(4K_n m - C_n^2)]}{14\pi^2 m}$	1.05×10^5	N/m
Tangential Damping Coefficient (c_t)	0	kg/s
Friction Coefficient (μ)	0.177	-
Normal Eigen-Frequency (ω_n) = $\sqrt{\dfrac{K_n}{m} - \left(\dfrac{C_n^2}{4m^2}\right)}$	1.99×10^5	-
Contact Time (T_c) = $\dfrac{\pi}{\overrightarrow{\omega_n}}$	1.58×10^{-5}	s
Time Step Size (Δt) = $\dfrac{T_c}{n_t}$	3.16×10^{-7}	s

Similarly parameters for sphere-sphere interactions are as below:

Table 4.2. Parameters for sphere-sphere interactions.

Parameter	Value	Units
Maximum velocity in the system (v_{max})	3	m/s
Particle Diameter (d_p)	0.003	m
Particle Density (ρ_p)	2500	kg/m³
Normal Coefficient of Restitution (COR_n)	0.700	-
Tangential Coefficient of Restitution (COR_t)	0.250	-
Percentage for Overlap (f)	1.0%	-
Time Steps per Contact (n_t)	50	-
Poisson Ratio (ν for glass 0.18 to 0.30, avg=0.24)	0.24	-
Mass of Particle (m) = $\dfrac{4}{3}\pi r^3 \rho_p$	3.53×10^{-5}	kg
Effective Particle Mass (m_{eff}) = $\dfrac{m_1 m_2}{m_1 + m_2}$	1.77×10^{-5}	kg

Parameter	Value	Units
Normal Stiffness Coefficient, $K_n = \dfrac{1}{f^2}\dfrac{mv_{max}^2}{r^2}$	7.07×10^5	N/m
Normal Damping Coefficient, $C_n = \sqrt{\dfrac{4K_n m}{\sqrt{\left(\dfrac{\pi^2}{\ln^2(COR_n)}+1\right)}}}$	0.7974	kg/s
Tangential Stiffness Coefficient, $K_t = \dfrac{[\alpha\cos^2(COR_t)(4K_n m - C_n^2)]}{14\pi^2 m}$	5.27×10^4	N/m
Tangential Damping Coefficient (C_t)	0	kg/s
Friction Coefficient (μ)	0.177	-
Normal Eigen-Frequency (ω_n) = $\sqrt{\dfrac{K_n}{m}-\left(\dfrac{C_n^2}{4m^2}\right)}$	1.99×10^5	-
Contact Time (T_c) = $\dfrac{\pi}{\overrightarrow{\omega_n}}$	1.58×10^{-5}	s
Time Step Size (Δt) = $\dfrac{T_c}{n_t}$	3.16×10^{-7}	s

The equations used for the determination of these parameters in PASIMODO depend on whether the case is a particle-particle or particle-wall interaction because in PASIMODO sphere-wall interactions are modeled by two spheres (one as a dummy sphere with triangle as mirror between the two spheres).

4.4 Results and Discussion

The objective to start the work for simulation of few particles was to get a deep insight for different forces into play and how do they interact, save huge computational efforts to check if the model and numerical scheme are working well or not.

To start with some experimental results already existed (though limited in number) to validate the simulation results. One of the experiments was performed by Lorenz et al. [1] in which they set up an experiment to detect the impact characteristics of almost

spherical particles of glass. However, there were still some problems regarding sphericity, surface reflectivity, and surface damage etc. (Lorenz et al. [1]). The basic set up used in this experiment was based on Foerster et al. [7].

In the simulations, 25 particles were dropped from a certain height at initial velocity of 1.5 m/s and at different psi1 values i.e. ratio of the tangential contact point velocity to normal contact point velocity before collision.
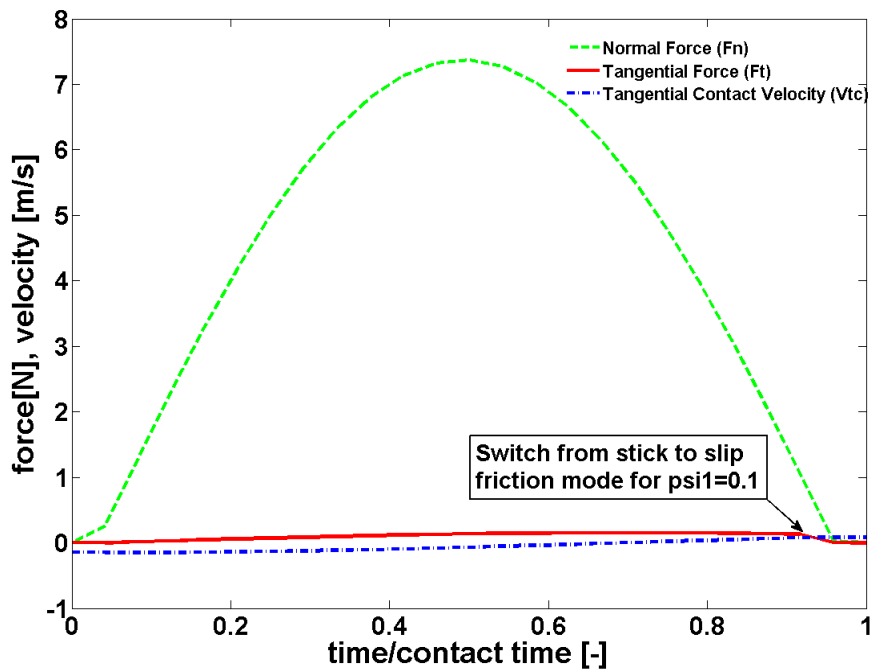
Figure 4.2. Normal and tangential force and tangential contact velocity against time/contact time for low values of psi1.

The normal force during the contact increases gradually and then decreases after the collision or impact with the wall. Similarly, tangential force increase linearly during the contact an after certain time it switches from stick to slip friction at the end of contact for low psi2 values. The tangential contact point velocity increases almost linearly at this value of psi1 (0.1) as shown in Fig. 4.2.

_____
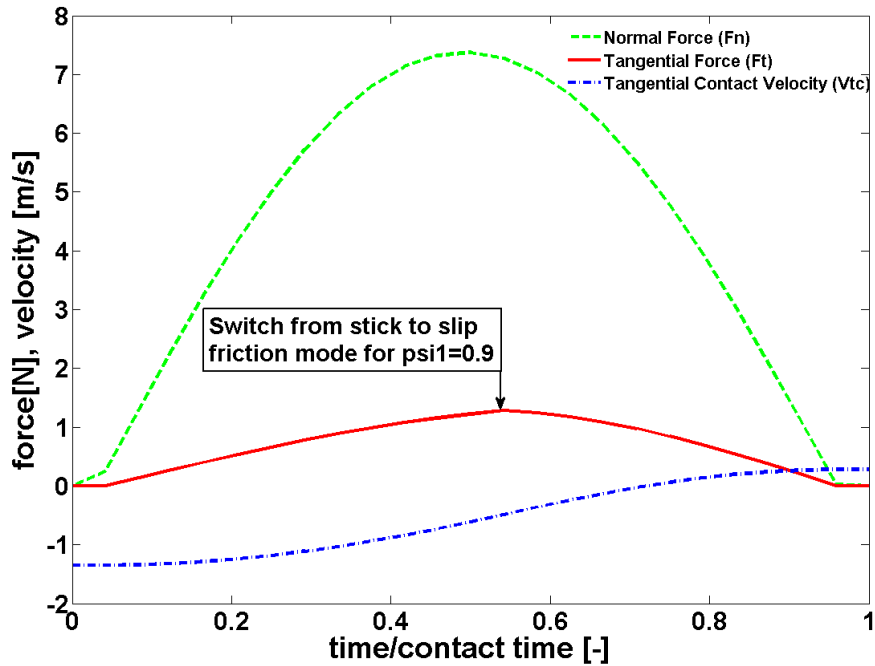
Figure 4.3. Normal and tangential force and tangential contact velocity against
time/contact time for intermediate values of psi1.

Similarly, in Fig. 4.3, the trend for normal force is almost the same; it increases during the contact point and then a decrease during the start of release in the impact. In this case the tangential force, however, switches from stick to slip almost in the middle of the contact for the intermediate values of ps1 (0.9 in this case).

Fig. 4.4 shows the same plot but for high psi1 values, i.e., 2.4. In this case, however, it is difficult to distinguish between stick and slip friction. The normal force and tangential contact velocity have the same trend as for intermediate psi1 values.
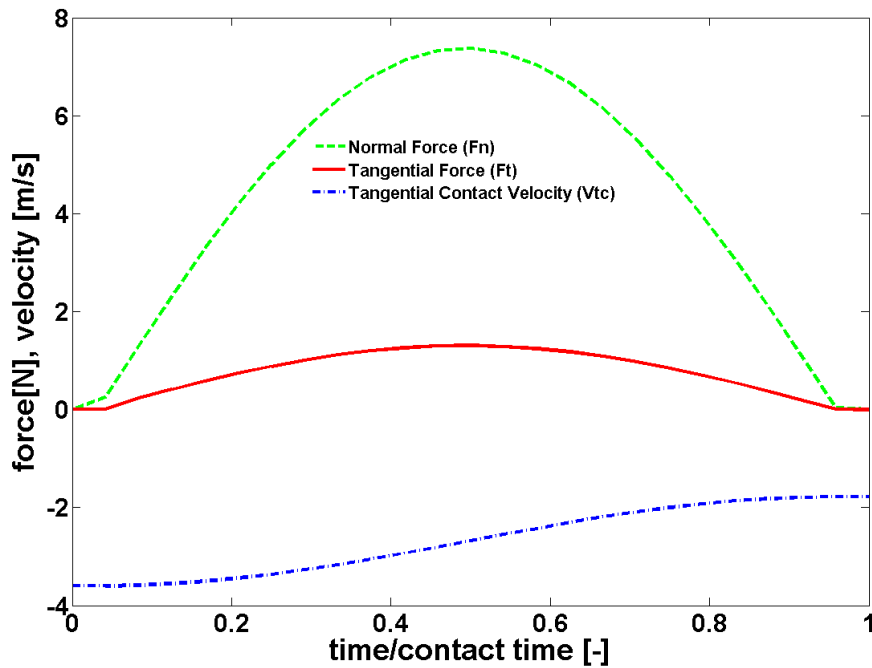
Figure 4.4. Normal and tangential force and tangential contact velocity against time/contact time for high values of psi1.

Later, psi1 and psi2 were plotted against each other for 25 different values of psi1. The results obtained in this chart are in good comparison to experimental results by Lorenz et al. [1], psi2 values show a decrease below zero in the first part of the graph and then increase linearly against psi1 values.
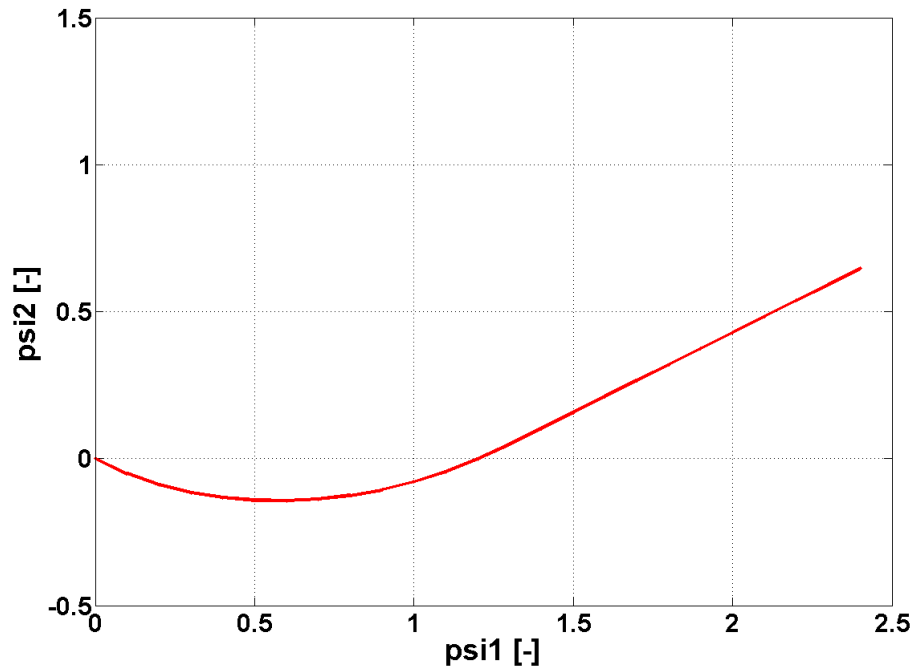
Figure 4.5. psi1 versus psi2

4.5 Conclusion

The results obtained were well in comparison with the experimental results and gave a full insight into the collision mechanics with simple particles. Computational efforts put in were a minimal in comparison to the knowledge gained through these simple simulations. The results were extended to other materials as well.

4.6 Nomenclature

C_n normal damping coefficients (kg-s^{-1})

C_t tangential damping coefficients (kg-s^{-1})

C_r viscosity coefficient (-)

COR_n normal coefficient of restitution (-)

COR_t tangential coefficient of restitution (-)

d_p particle diameter (m)

_____

f	percentage for overlap (-)
$\vec{F}$	force (N)
$\vec{F}_{cont,ij}$	contact force between particle i and j (N)
$\vec{F}_{drag,i}$	drag force on particle i (N)
$\vec{F}_{g,i}$	gravitational force on particle i (N)
$\vec{F}_{n-cont,ik}$	non-contact force on particle i by other particle k (N)
$\vec{F}_{total,i}$	total force on particle i (N)
I_i	moment of inertia (kg-m^2)
k_n	normal spring coefficient (-)
k_t	tangential spring coefficient (-)
m	mass (kg)
$\vec{M}_{ij}$	torque (Nm)
n_t	time steps per contact (-)
$psi1$	ratio of the tangential contact point velocity to normal contact point velocity before collision (-)
$psi2$	ratio of the tangential contact point velocity to normal contact point velocity after collision (-)
r	particle radius
t	time (s)
T_c	contact time (s)
$\varDelta t$	time step (-)
$\vec{x}$	position in x-direction (m)

_____

Greek Letters

μ friction coefficient (-)

ρ_p particle density (kg-m^{-3})

$\vec{\omega}_i$ angular velocity (s^{-1})

ω_n normal-eigen frequency (-)

$\vec{\omega}_n$ relative angular velocity component in the contact plane (s^{-1})

Subscripts

d drag

g gravitational

$cont$ contact

max maximum

n normal

t tangential

i particle i

j particle j

4.7 References

[1] A. Lorenz, C. Tuozzolo, M.Y. Louge, Measurements of impact properties of small, nearly spherical particles. Experimental Mechanics 37 (1997) 292-298.

[2] H.P. Zhu, Z.Y. Zhou, R.Y. Yang, A.B. Yu, Discrete particle simulation of particulate systems: Theoretical developments. Chemical Engineering Science 62 (2007) 3378-3396.

[3] M.S. Siraj, S. Radl, B.J. Glasser, J.G. Khinast, Effect of Blade Angle and Particle Size on Powder Mixing Performance in a Rectangular Box. Powder Technology 211 (2011) 100-113.

[4] P.A. Cundall, O.D.L. Strack, Discrete Numerical-Model for Granular Assemblies. Geotechnique 29 (1979) 47-65.

[5] Muguruma, Y., Tanaka, T., Tsuji, Y., 2000. Numerical simulation of particulate flow with liquid bridge between particles (simulation of centrifugal tumbling granulator). Powder Technology 109, 49-57.

[6] A. Dziugys, B. Peters, An approach to simulate the motion of spherical and non-spherical fuel particles in combustion chambers. Granular Matter 3 (2001) 231-265.

[7] http://www.itm.uni-stuttgart.de/research/pasimodo/pasimodo_en.php. Online (21.01.2012).

[8] S.E. Foerster, M.Y. Louge, H. Chang, K. Allia, Measurements of the Collision Properties of Small Spheres. Physics of Fluids 6 (1994) 1108-1115.

5 Effect of Blade Angle and Particle Size on Powder Mixing Performance in a Rectangular Box

This study focuses on the understanding of flow over a single blade and its impact on powder mixing. The Discrete or Distinct Element Method (DEM) is used and the flow of a single blade through a bed of a binary particle mixture is studied. Mixing performance with respect to a blade-rake angle and particle size is investigated using the Modified Generalized Mean Mixing Index (MGMMI) and the maximum mean instantaneous velocities. A wide range of angles and different loading scenarios of the binary particle mixture were studied. Velocity profiles for all these cases were computed, as well as the forces on particles and the blade. The results showed an inverse relation between the interparticle force and blade-rake angle. Systems with a higher number of larger particles experienced a higher interparticle force. Similar results were obtained for the blade force. The results for mixing efficiency showed that if the smaller particles are placed at the top this leads to a higher mixing performance. The mixing performance was highest for blade-rake angles that offered a maximal surface area or maximal resistance to the flow of particles, which occurred for blade-rake angles from 70° to 90°.

5.1 Introduction

A wide variety of industrial mixers (blenders) are employed for solid particle (granular) mixing, particularly in the pharmaceutical industry due to the need to blend small quantities of active pharmaceutical ingredients (APIs) with larger amounts of excipients to provide the final mixture for a pharmaceutical dosage form. Clearly, blending is a key unit operation for solid dosage form manufacturing as it ensures blend homogeneity that is directly linked to the (potential) critical quality attribute (CQA) "content uniformity", which in turn is directly related to product safety and efficacy [1]. Inefficient blending can lead to increased variability of the active component in the final dosage form, threatening the health of patients [2]. Thus, the understanding of granular mixing or powder blending has been a focus of interest for many decades. A general classification of mixing mechanism has been given by Lacey [3]. Shear mixing can occur in convective, high-shear mixers and tumbling mixers, where a layer of powder avalanches down along a slope plane [4]. Convective and shear mixing are difficult to distinguish [5] in dense particle systems and can be collectively termed as convective-shear mixing.

Most powder blenders can be classified as tumbling and convective mixers. Compared to tumbling mixers, convective-bladed mixers have been investigated in more detail using both experimental and simulation techniques [2, 6-15]. A number of publications have appeared recently in the literature regarding convective batch mixers with two [6,7,12,13,15] or four [8-10,11,14] blades and using experimental [6,8] and simulation [9,10,12-15] techniques - or both for comparison purposes [7,11]. Stewart et al. [6] investigated granular flow over a flat bladed stirrer using positron emission particle tracking and observed three-dimensional recirculation zones, as well as a linear dependence of particle speed on the blade speed. In addition, they observed that the size of the recirculation zones and the number of blade passes that the particles spend therein decreased with an increase in fill level and blade speed. In their second paper [7], they compared their experimental results with the simulation results. Conway et al. [8] used particle image velocimetry (PIV) to study velocity fields near the top and the wall for near-monodisperse and polydisperse granular materials. In addition, they observed three-dimensional recirculating zones and studied mixing and segregation with respect to

shear rates. Remy et al. [9] investigated the effect of blade orientation on particle flow patterns and mixing kinetics using DEM simulations. They also investigated the effects of friction coefficients on mixing and normal and shear stresses and their dependence on the mixer's height and the friction coefficients of the particles. In another publication, Remy et al. [10] reported the effects of fill level and mixer properties (vertical blade position from bottom, wall friction, mixer diameter and blade speed) on granular flow characteristics and mixing. In yet another paper [11] they used experiments and simulations to quantify the effects of varying particle roughness on granular flow of cohesionless particles and the effects of varying blade speed. Zhou et al. [12] studied the effects of the blade speed, the particle size, the volume fraction and the particle density on the segregation of binary mixtures. In addition, Zhou et al. [13] performed a microdynamic analysis of the particle flow, especially the effects of sliding and rolling friction coefficients on three-dimensional recirculating particle zones. Radl et al. [14] investigated the mixing characteristics of wet granular matter and observed better mixing rates and performance compared to dry granular matter under the same conditions.

In this study, convective bladed mixers are the focus. However, instead of investigating the whole mixer the objective was to gain a detailed understanding of the particle flow across a single blade by studying the impact of single-blade orientation and shape on blending performance and mixing. A few experimental studies on two-dimensional flows over a single flat blade in a cylinder [16] (e.g., by using paddle type blades [17-19] and by taking photographs) were reported in the literature. Laurent et al. [20] used a single blade and monitored the motion in a particle bed using positron emission particle tracking. In a recent paper [15], single-blade mixing was studied in a 3-D mixer system using three angles of 45°, 90°, and 135°. The mixing performance in this work was quantified using Lacey's mixing index, and the 90°-degree angle was reported to show the highest mixing rate.

In this work mixing is investigated in a convective batch mixer whose geometry is different from any other convective batch mixer reported before. A simple, thin, 3D rectangular box (depth = 0.1m) with a single blade is considered. The box is filled with either a monodisperse particle system or a binary particle mixture. Then, movement of the blade occurs only in one direction (i.e., x-direction), and the results are monitored

and analyzed to gain an understanding of the mixing phenomenon at a very basic level, without involving complex mixer geometries. Thus, the objective was to study single blade flows in binary particle mixtures and the impact on mixing and forces as a function of blade-rake angle and geometry. DEM has been used to simulate the flow over the blade. The DEM method is briefly presented in the next section, followed by a section describing the parameters of the study. Finally, the results are presented.

5.2 Numerical Method

Over the last years, the Distinct or Discrete Element Method (DEM) has become a powerful tool to simulate granular flows [14-21], as it gives a detailed picture of the flow by keeping track of each individual particle. For example, Sarkar and Wassgren [28] have recently investigated the effect of operating conditions on flow and mixing of a continuous granular mixer using DEM simulations. Studies including DEM with an external force (as in this case) have been reported as well. Examples include the studies by Zhenghua et al. [32], Shuai et al. [33], Xiang et al. [34] and Tatemoto et al. [35] for vibrated fluidized beds and Willigen et al. [36] for electric-field enhanced fluidized bed. More details on the basic principles of DEM simulations can be found in the review paper of Zhu et al. [29]. However, recent novel developments, allowing the simulation of many millions of particles, have transformed DEM from a tool for simulating $O(10^5)$ particles (i.e., model problems) into a tool that is capable of tackling $O(10^7)$ and more particles and generating reliable statistics [30]. This has made DEM capable of handling some realistic large–scale problems, i.e., the design, scale-up and optimization of industrial applications.

In DEM every particle is treated in a discrete manner. All the forces acting on it are considered, including contact forces, body forces, hydrodynamic forces and cohesive forces. These forces are then integrated over time to obtain the position and the velocity of each individual particle. Newton's second law of motion can be translated into a force balance equation for a particle i as follows:

$$m_i \frac{d^2 \vec{x}_i}{dt^2} = \vec{F}_{total,i} = \sum_j \vec{F}_{cont,ij} + \sum_k \vec{F}_{non-cont,ik} + \vec{F}_{g,i} + \vec{F}_{drag,i} \qquad (5.1)$$

Here, m_i is the mass of the particle i, and $\vec{x_i}$ is the position of the particle. This equation can be integrated to calculate velocity, and double integration yields the position of the particle i. $\vec{F}_{total,i}$ is the sum of all forces acting on the particle i, whereas $\sum_j \vec{F}_{cont,ij}$ is the sum of contact forces between particle i and j. $\sum_k \vec{F}_{non-cont,ik}$ is the sum of non-contact forces or cohesive forces between particle i and k, e.g., van der Waals, electrostatic and liquid bridge forces. $\vec{F}_{drag,i}$ is the drag force exerted by a surrounding fluid. Since in granular flows fluid-particle interactions are often much smaller in comparison to contact and other forces, $\vec{F}_{drag,i}$ may be ignored under certain circumstances (e.g., relatively large particles in air, as in this study). $\vec{F}_{g,i}$ is the gravitational force exerted on the particle i.

The rotational momentum balance is solved as well, i.e.,

$$I_i \frac{d\vec{\omega_i}}{dt} = \sum_j \vec{M}_{ij} \tag{5.2}$$

In Eq. 2, I_i is the moment of inertia, ω_i is the angular velocity and $\vec{M}_{ij}$ is the torque acting on particle i by particle j.

Various numerical schemes are available for solving theses equations for translational and rotational motion of each particle. A commercial software EDEM has been used to solve the momentum balance equations. The first term on the right hand side of Eq. 1, i.e., $\sum_j \vec{F}_{cont,ij}$, is the most critical part comprising normal and tangential force components. In this work, the simulations are based on the simplified Hertz-Mindlin and Deresiewicz model [21-26], i.e.,

- Normal force

$$\vec{F}_n = \left[-\frac{4}{3} E^* \sqrt{R^*} (\delta_n)^{3/2} - C_n (8m^* E^* \sqrt{R^* \delta_n})^{1/2} . (\vec{v_c} . \hat{n}_c) \right] \hat{n}_c \tag{5.3}$$

- Tangential force

$$\vec{F}_t = -\mu \, | \, \vec{F}_{n,e} \, | \, (1 - (1 - | \, \vec{v}_c^t \, | \, / \delta_{max})^{3/2}) \hat{v}_c^t$$
$$+ 2C_t (1.5 \mu m^* \, | \, \vec{F}_{n,e} \, | \, . \sqrt{1 - | \, \vec{v}_c^t \, | \, / \delta_{max}} \, / \delta_{max})^{1/2} . (\vec{v}_c \times \hat{n}_c) \times \hat{n}_c \qquad (5.4)$$

- Rolling friction torque

$$m_r = -\min(\, \mu_r \, | \, \vec{F}_n \, |, \mu_r' \, | \, \vec{\omega}_n \, |) \hat{\omega}_n \qquad (5.5)$$

The following basic steps are typical for all DEM simulations:

1. Collision detection through particle-particle and particle-wall contacts/overlaps.

2. Application and calculation of contact forces to all collisions.

3. Calculation of other forces, body (gravitational) and hydrodynamic (fluid drag) for all particles (fluid drag was neglected in this work).

4. After calculation of the unknowns in Eqs. 5.1 and 5.2, the particles' translational and rotational accelerations are calculated.

5. Integration of the acceleration numerically to find the particles' new positions and velocities.

For the mixing calculations, mixing indices need to be established in order to quantify the mixing process. In this work, the mixing index was based on the Generalized Mean Mixing Index (GMMI) [27]. However, the GMMI was modified after some limitations became apparent under certain conditions.

If there are two types of particles, *a* and *b*, then the GMMI of *a*-type particles, i.e., $GMMI_a$, is calculated [27] as the sum of the mean positions of *n* *a*-type particles divided by the sum of the mean positions of all *N* particles of *a*+*b* type. $GMMI_a$ is calculated in x, y, or z directions depending on whether positions x, y or z are used. The total GMMI is then:

$$GMMI_a = (GMMIx_a + GMMIy_a + GMMIz_a)/3 \qquad (5.6a)$$

where

$$GMMIx_a = \frac{\left[\sum\limits_{p=1}^{n}\frac{(x_p - x_{ref})}{n}\right]}{\left[\sum\limits_{q=1}^{N}\frac{(x_q - x_{ref})}{N}\right]} \quad GMMIy_a = \frac{\left[\sum\limits_{p=1}^{n}\frac{(y_p - y_{ref})}{n}\right]}{\left[\sum\limits_{q=1}^{N}\frac{(y_q - y_{ref})}{N}\right]} \quad GMMIz_a = \frac{\left[\sum\limits_{p=1}^{n}\frac{(z_p - z_{ref})}{n}\right]}{\left[\sum\limits_{q=1}^{N}\frac{(z_q - z_{ref})}{N}\right]}$$

Here x_{ref}, y_{ref}, and z_{ref} are the reference positions in x, y and z directions and are zero in this case as the origin is on the front-side lower-left corner, as shown in Fig. 5.2. It can best be illustrated by an example analogous to the simulations explained by Fig. 5.1. GMMI for this example is:

$$GMMI_{blue} = (GMMIx_{blue} + GMMIy_{blue} + GMMIz_{blue})/3 \tag{5.6b}$$

where

$$GMMIx_{blue} = \frac{\left[\sum\limits_{p=1}^{5}\frac{x_p}{5}\right]}{\left[\sum\limits_{q=1}^{10}\frac{x_q}{10}\right]} \quad GMMIy_{blue} = \frac{\left[\sum\limits_{p=1}^{5}\frac{y_p}{5}\right]}{\left[\sum\limits_{q=1}^{10}\frac{y_q}{10}\right]} \quad GMMIz_{blue} = \frac{\left[\sum\limits_{p=1}^{5}\frac{z_p}{5}\right]}{\left[\sum\limits_{q=1}^{10}\frac{z_q}{10}\right]} \tag{5.6c}$$
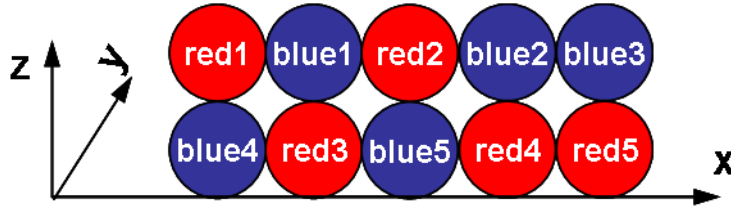
Figure 5.1. MGMMI Example.

The problem with GMMI is that if the directional values of GMMI are larger than 1 for one direction and smaller than 1 for another direction, the average GMMI may still give 1, although in each direction mixing is not perfect (a GMMI of 1 corresponds to perfect mixing). Such cases were obtained in the simulations. Thus, a modified GMMI was used, i.e.,

$$MGMMI = 1 - \frac{abs(1 - GMMIx_a) + abs(1 - GMMIy_a) + abs(1 - GMMIz_a)}{3} \tag{5.7}$$

In this case, no MGMMI value is greater than the ideal mixing value of 1.0. A value of MGMMI=1 indicates that a binary mixture is perfectly mixed. The MGMMI has several advantages [27]:

1. It is precise and easy to implement for DEM simulations.
2. It is fast to evaluate.
3. It uses a physical property, i.e., the position of all particles, and does not depend on sampling.
4. It does not depend on a sample size.
5. It is not limited to only binary mixtures like some other mixing indices.
6. It indicates mixing, as well as segregation.

Thus, MGMMI is used in this work to quantify the effect of mixing.

5.3 Simulation Set-up

The parameters used for all simulations are summarized in Table 5.1. As discussed above, industrial batch mixing is mostly carried out in cylindrical containers with a different number of blades, whereas in the present case a rectangular box with a single blade was used.

Table 5.1. Parameters used for the simulations.

Parameter	Value	Units
Box dimensions (length × width × height)	$0.8 \times 0.1 \times 0.2$	m
Blade dimensions (length × width)	0.1×0.05	m
Blade-rake angles used	40, 50, 60, 70, 80, 90, 100, 110, 120, 130, 135, 140, 150	degrees
Material (Particle /Blade/Container)	glass/steel/steel	-
Particle diameter (d_p)	6, 8 and 10	mm
Particle density, glass (ρ_p)	2456	kg/m³
Poisson ratio	0.25	-

_____

Parameter	Value	Units
Shear modulus	2.2×10^8	Pa
Coefficient of restitution	0.3 (glass-steel) & 0.5 (glass-glass)	-
Coefficient of static friction	0.5 & 0.0 for cases without wall friction	-
Coefficient of rolling friction	0.01 & 0.0 for cases without wall friction	-

Figure 5.2 shows the box geometry. The dimensions of the box are (0.8m×0.1m×0.2m).
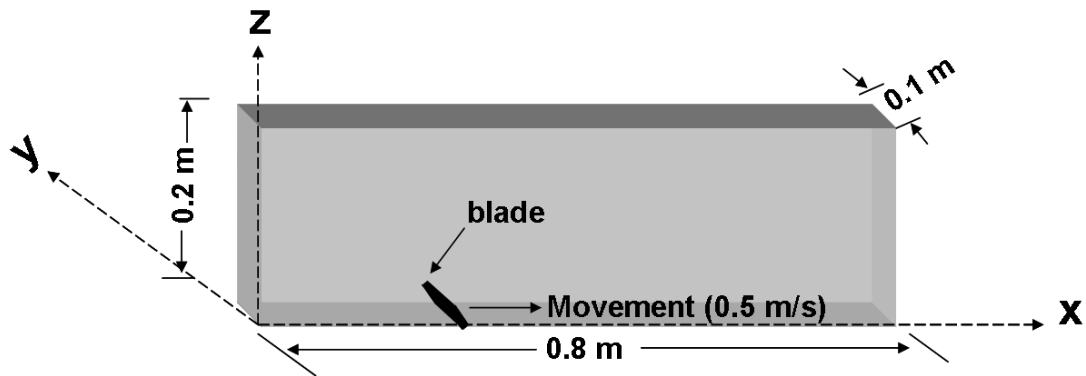
Figure 5.2. Geometry of box used for the simulations.

Fig. 5.3 illustrates the blade-rake angle. It is important to note, that angles smaller than 90º are called *acute*, while angles larger than 90º are *obtuse*.
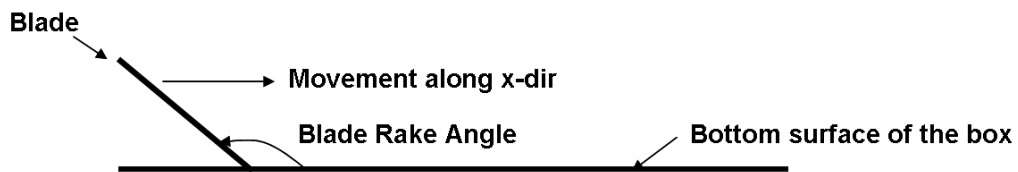
Figure 5.3. Blade rake angle.

The distance between box and blade was zero. However, no friction was assumed between the blade and the walls of the box. A single blade was considered, in order to study the effects of and the flow across a single blade.

Three particle diameters (6 mm, 8 mm, and 10 mm) were used in three combinations, i.e., 6 and 10 mm, 8 and 10 mm, and 10 and 10 mm. The three different sizes were selected in order to study the effect of different particle size ratios on binary-mixtures particle mixing. Relatively large particles were used in order to reduce computational effort and to compare to experimental data. Also other researchers studied large particles. For example, Remy et al. [9] used 5 mm and 10 mm particles for their simulations and reported that the change of size did not affect significantly the flow patterns. However, effects of particle size on DEM simulations are known, for example, when the particle size approaches the size of gaps between surfaces, leading to locking effects. Further studies will address size effects of smaller particles, and were excluded from the current study. Two types of particles (i.e., blue and red) were arranged in the box by first dropping one type of particles and then dropping the next one on top. This type of arrangement is closer to practical situations than the side-by-side arrangement used in some previous studies [9-11, 14].

The particle size ratio is defined as:

$$r = \frac{d_{p,top}}{d_{p,bottom}} \tag{5.8}$$

Thus, if larger particles are on top, r > 1. A total of five particle size ratios r were studied, i.e., Case A: $r = 0.6$, Case B: $r = 0.8$, Case C: $r = 1.0$, Case D: $r = 1.25$, Case E: $r = 1.67$. Furthermore, Case F had $r = 1$. However, here wall friction was set to zero, mimicking a situation where particles are pushed over the blade via a vertical wall (at the end) and do not experience tangential forces from the particle bed, i.e., a situation similar to a 3D mixer where particle flow is restricted by the preceding blade. In this case only selected angles were simulated. The presence or absence of wall friction also helps in analyzing the effect of the mixer material and its surface quality on the mixing performance. Friction coefficients and the coefficient of restitution are given in Table 5.1. A total of sixty-eight simulations were performed, as summarized in Table 5.2.

Table 5.2. Summary of the cases considered.

Category	No. of Particles	Top and Bottom Particle Diameters Ratio ($d_{p,top}/d_{p,bot}$)	Blade-rake Angle (deg)
Case-A	(top) 2500 blue ($d_{p,top}$ = 6 mm) + (bot) 2500 red ($d_{p,bot}$ = 10 mm)	0.6	40, 50, 60, 70, 80, 90, 100, 110, 120, 130, 135, 140, and 150
Case-B	(top) 2500 blue ($d_{p,top}$ = 8 mm) + (bot) 2500 red ($d_{p,bot}$ = 10 mm)	0.8	40, 50, 60, 70, 80, 90, 100, 110, 120, 130, 135, 140, and 150
Case-C	(top) 2500 blue ($d_{p,top}$ = 10 mm) + (bot) 2500 red ($d_{p,bot}$ = 10 mm)	1.0	40, 50, 60, 70, 80, 90, 100, 110, 120, 130, 135, 140, and 150
Case-D	(top) 2500 blue ($d_{p,top}$ = 10 mm) + (bot) 2500 red ($d_{p,bot}$ = 8 mm)	1.25	40, 50, 60, 70, 80, 90, 100, 110, 120, 130, 135, 140, and 150

Category	No. of Particles	Top and Bottom Particle Diameters Ratio $(d_{p,top}/d_{p,bot})$	Blade-rake Angle (deg)
Case-E	(top) 2500 blue ($d_{p,top}$ = 10 mm) + (bot) 2500 red ($d_{p,bot}$ = 6 mm)	1.67	40, 50, 60, 70, 80, 90, 100, 110, 120, 130, 135, 140, and 150
Case-F	(top) 2500 blue ($d_{p,top}$ = 10 mm) + (bot) 2500 red ($d_{p,bot}$ = 10 mm)	1.0	60, 90, and 140

In all cases, 5000 particles were used, half of them blue, the rest being red. The material of the particles was glass, whereas the blade and the box were assumed to be made of steel, as in an industrial mixer. The blade was given a translational motion of 0.5 m/s in the x direction (after 0.4s, to allow settling). It has been shown by Remy et al. [10], that in the quasi-static regime, the blade speed does not have significant impact in mixing. The dimensionless shear rate is known to be one of the most important parameters that determine the regime of a granular flow [31]:

$$I = \frac{\dot{\gamma} \cdot d_p}{\sqrt{P/\rho}} . \tag{5.9}$$

Here, $\dot{\gamma}$ is the shear rate, d_p is the particle diameter, P is a characteristic normal stress (i.e., the particle pressure) and ρ is the bulk density. The dimensionless parameter I describes the relative importance of inertia to the normal stress in the particle bed. For vertical free surface flows, the characteristic normal stress can be approximated by [31]:

$$P = \rho \cdot g \cdot h, \tag{5.10}$$

and the shear rate can be approximated with [31]:

$$\dot{\gamma} = V/h. \tag{5.11}$$

Here, h and V are a characteristic bed height and bed velocity, respectively. Inserting these approximations into the definition of the dimensionless shear rate yields:

$$I = \frac{V \cdot d_p}{\sqrt{g \cdot h^3}}. \tag{5.12}$$

If the parameter I is above 10^{-2}, the quasi-static regime (where the effective friction coefficient is constant) is no longer valid, and the transition to the dense inertial regime has been reached [31]. In the current case I was 0.096 for the largest particles. Thus, the process is not in the quasi-static regime. However, the influence of speed was still small, as was indicated by test simulations (see Appendix). The impact of blade speed will be reported on in further publications. The blade movement was stopped at t=1.9 s, and the total simulation time was 2.7 s in order to allow settling of the particles after the cessation of blade movement.

As discussed above, six categories of cases (A-F) were studied using blade-rake angles of 40° to 150° with 10° intervals (plus a set of simulations at 135°). Fig. 5.4 shows snapshots of three cases in the initial state for a blade-rake angle of 140° after settling of the particles. All other cases looked similar. Due to the settling process, the interface between blue and red particles was only approximately planar.
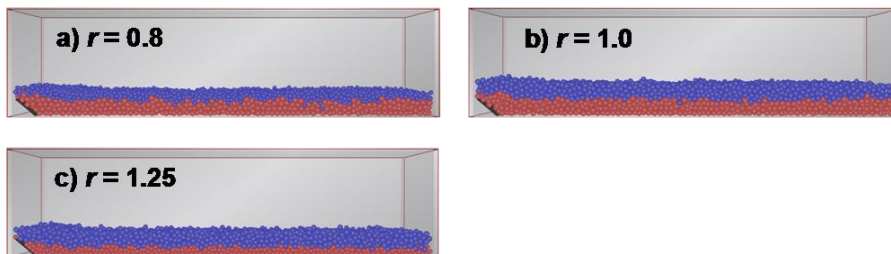
Figure 5.4. Selected simulation cases at the initial state for a blade-rake angle of 140°.

5.4 Results and Discussion

First, the final results of one blade-pass are reported before analyzing and quantifying mixing for the various cases. Figs. 5.5 to 5.9 show the final state of the bed after one blade pass from left to right for the five cases (A-E) for selected blade angles. A visual inspection reveals that size ratios r smaller than 1 show better mixing, i.e., cases with the larger particles at the bottom yield better mixing results. If the mixing performance efficiency is denoted by η, then $\eta_{r=0.6} > \eta_{r=0.8} > \eta_{r=1.0} > \eta_{r=1.25} > \eta_{r=1.67}$. This is expected to a certain extent, since it is known that in shear layers larger particles have a tendency to rise to the top, and *vice versa*, a phenomenon called the "brazil nut effect" or "sieving segregation". Thus, a situation with the larger particles at the bottom will benefit from sieving segregation. Alternatively, large particles initially at the top will show a tendency to stay there.
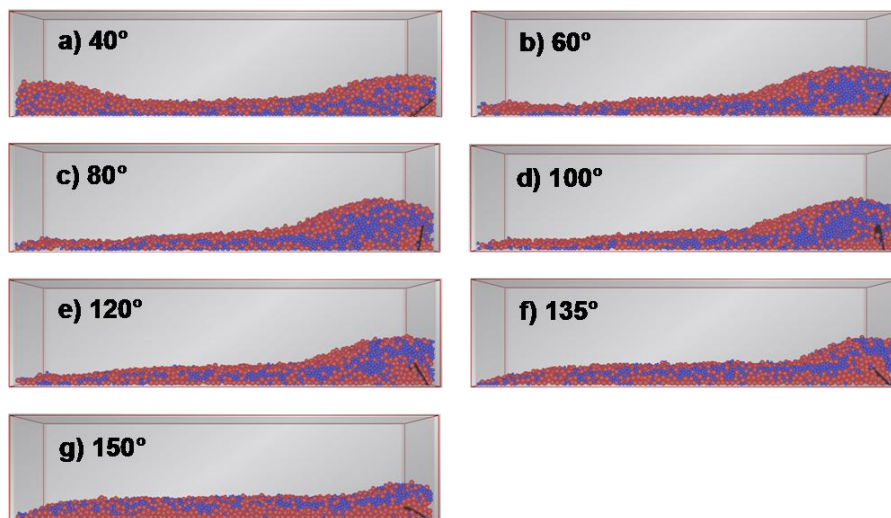
Figure 5.5. Case A: Final particle position at the end of the simulation for r = 0.6.
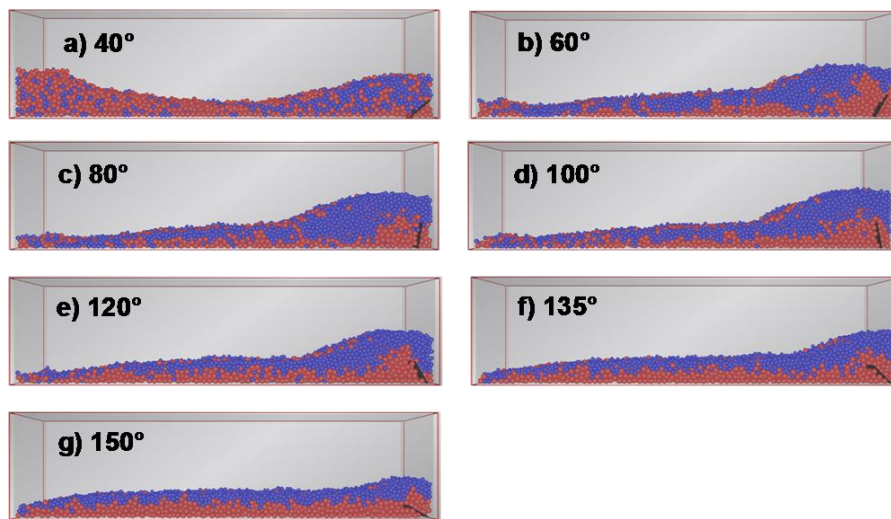
Figure 5.6. Case B: Final particle position at the end of the simulation for r = 0.8.
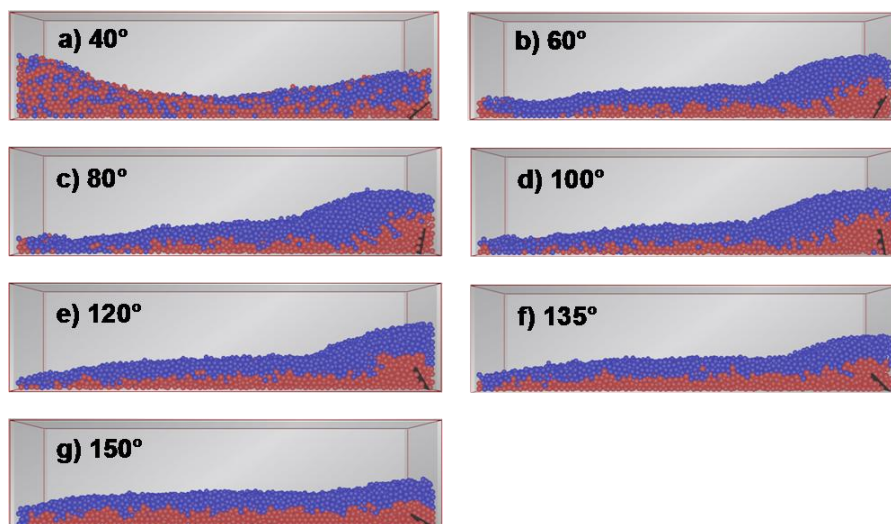
Figure 5.7. Case C: Final particle position at the end of the simulation for r = 1.0.
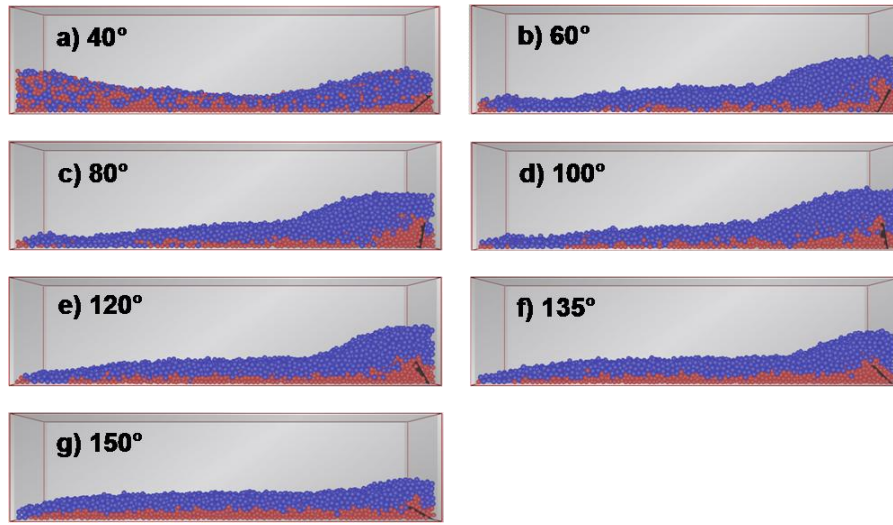
Figure 5.8. Case D: Final particle position at the end of the simulation for r = 1.25.
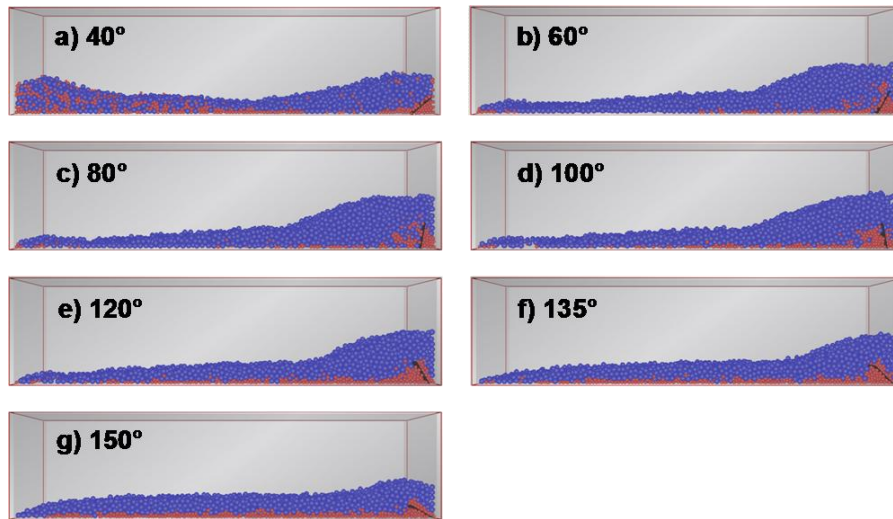
Figure 5.9. Case E: Final particle position at the end of the simulation for r = 1.67.

Another visual inspection result is that the particle bed-height variations are the smallest for strongly obtuse blade-rake angles, i.e., 150° and 140°. For acute and slightly obtuse blade-rake angles the bed-height variation is significant. In these cases, a significant amount of powder is transported with the blade from the left to the right. Thus, these blade rake angles have a tendency to impart not only vertical mixing but also strong horizontal mixing to the bed. Interestingly, for strongly acute blade-rake angles of 40° and 50°, particles tend to accumulate in the beginning and at the end of the box

around the blade. In these two cases, particles were later found to be popping up due to the high stress developed in the bed in front of the blade. This will be discussed later.

Results were also obtained for a box with no wall friction, i.e., case F, and compared with simulations including wall friction, as shown in Fig. 5.10. In the absence of wall friction, the particle bed continues to move after the blade ceases movement. The effect is clear from Fig. 5.10 for blade angles of 90° and 60°. The back-movement of the particle bed after stopping of the blade contributes towards the accumulation of each type of particles in clusters at both ends leading to increased segregation. MGMMI values (discussed later) also suggest the same trend, i.e., that in the absence of wall friction, the mixing efficiency is lower as compared to a similar case with wall-friction for blade angles of 60° and 90°. Thus, wall friction is needed to transmit energy into the particle bed, leading to increased mixing. However, the difference is not as clear for a blade rake angle of 140°.
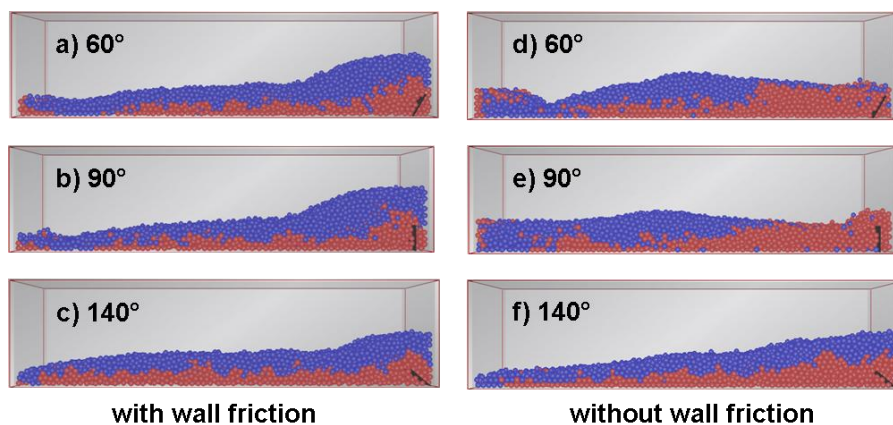
Figure 5.10. Case F: Final particle position at the end of the simulation for
r = 1.0 (with and without wall friction).

Fig. 5.11 shows blade relative velocities for all *r-value*s and selected blade-rake angles of 60°, 90°, and 140°. This figure shows blade-relative instantaneous velocities. The length of the vectors and the color of the field (from blue to red) represent the magnitude of velocities in increasing order. The results are plotted for blade position at x≈0.5 m, i.e., when the blade moved slightly more than half of the distance in the x direction (total length of the box is 0.8 m). Blue regions in Fig. 5.11 move with the blade, i.e., they have low blade-relative velocities, while red regions are more or less stagnant as they have a

blade-relative velocity of 0.5m/s to the left. (The blade has a velocity of 0.5m/s to the right).

The velocity profiles show that as the blade-rake angle decreased from 140° to 60°, for r=0.6, the blade-relative velocities in front of the blade reaches zero, because at acute and slightly obtuse blade-rake angles, the blade imposes a significant resistance on the particles. Thus, the particles in the blue zone move to the right as their blade-relative velocities approach zero. Simultaneously, strong heaps are formed for those smaller angles. The reason is that at angles close to and smaller than 90° particles are exposed to the maximal blade surface area, leading first to an accumulation of particles around the blade and then to heap formation. It is well known that strong heap formation leads to better mixing in bladed mixers as shown by Radl et al. [14]. Thus, it can be expected that for these cases mixing should be superior to the cases with a strongly obtuse angle (e.g., right column of Fig. 5.11), where the particles rather slide over the blade, thus not forming heaps.
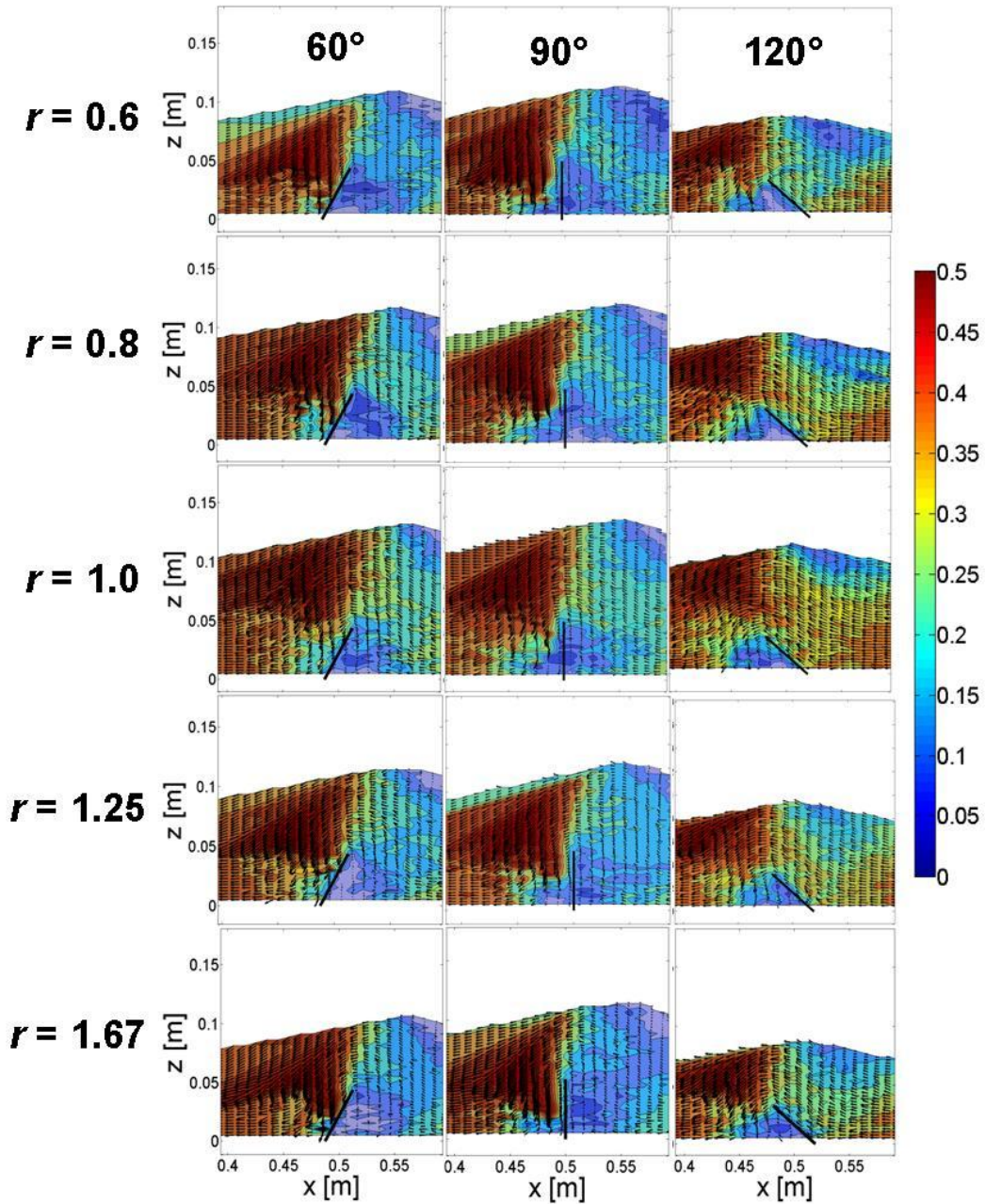
Figure 5.11. Blade relative velocities for all r-values of 0.6, 0.8, 1.0, 1.25 and 1.67 and selected blade-rake angles of 60°, 90° and 140°.

As *r* increases from 0.6 to 1.67 for a blade-rake angle of 140°, the blade-relative velocities in front of the blade are at maximum at *r*=1.0 and lowest for r=0.6 and 1.67. This is because at *r*=1.0 the two types of particles are of the same size, both having the largest diameters compared to other cases. All of the larger particles have lower instantaneous velocities, and hence, higher blade-relative velocities. Thus, they are more

stagnant than other cases, i.e., they slide across the blade easier than particle mixtures with two different particle sizes. The reason for this behavior is that in a mixture of two different sized particles, the smaller particles have higher instantaneous particle velocities, thus giving rise to overall decreased blade relative velocities, if blade speed is constant for all cases. That is why the mixing efficiency for $r < 1.0$ (i.e. $r=0.6$ and 0.8) is better than that for $r \geq 1.0$ (i.e. $r=1.0$, 1.25 and 1.67). The mixing efficiency for $r = 1.25$ and 1.67 is, however, less than that for $r = 1.0$ because for $r > 1.0$, the smaller particles are being blocked by a top layer of larger particles. The results show that particles of uniform size ($r=1$) flow differently than particles with a size variation. A difference between the flow of high and low r is not significant, however. Similar trends are observed for blade-rake angles of 60° and 90°.

Fig. 5.12 shows maximum mean instantaneous velocities (MMIV) along the x-direction (left to right of the box), i.e., x-components of the velocities (as y and z components were observed to be small and almost constant). MMIV were calculated by first taking the mean values of the instantaneous velocities of all particles (along the x-direction) at each time step, i.e., between 0.4s to 1.9 s, and then taking the maximum of these mean instantaneous velocities. MMIV, in fact, represents the highest mean instantaneous velocity along the x-direction of all particles attained in a simulation at any time-step. MMIV is an indicator of the mixing performance and corresponds well with the MGMMI calculations (discussed later). Therefore, MMIV may also be used to quantify mixing performance.
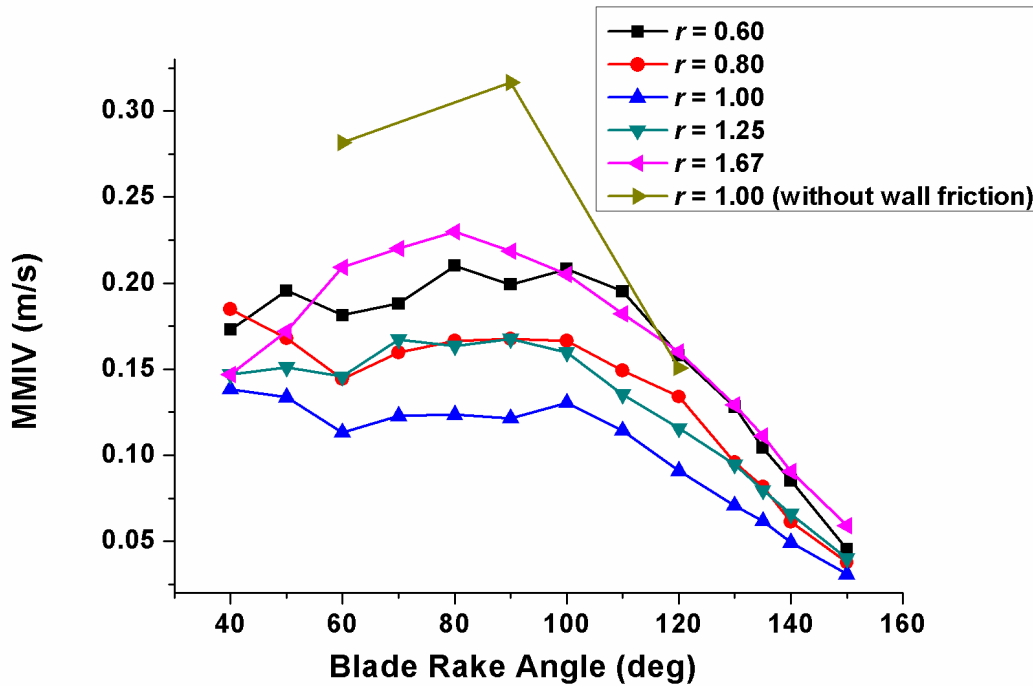
Figure 5.12. Variation of maximum mean instantaneous velocities (MMIV) with respect to blade-rake angle for different r-values (dp,top/dp,bot ratios).

The results show that all *r-value*s had the highest MMIV values at blade angle values between 80° to 100°, as summarized in Table 5.3.

Table 5.3. Blade-rake angle corresponding to highest MMIV values.

r values	Blade-rake angle
0.6	80°
0.8	90°
1.0	100°
1.25	90°
1.67	80°

Interestingly, the distribution is symmetric around r=1, as shown in Fig. 5.13. The figure shows that the highest MMIV values occur at about 80° blade-rake angle for *r* = 0.6, and as the *r* value increases the blade-rake angle values corresponding to highest MMIV also increase. It is 100° for *r* = 1.0. However, for *r* values greater than 1.0, the

blade angles corresponding to highest MMIV decreases. Thus, the system comprising of 8 mm and 10 mm particles exhibits the highest MMIV values at the same blade-rake angle no matter whether smaller particles are on top or larger particles are on top. Similarly, system comprising of 6 mm particles and 10 mm particles exhibit highest MMIV values at around 80° angle regardless of filling order. Thus, an important conclusion of this work may be that the angle should be selected based on the mixing objective.
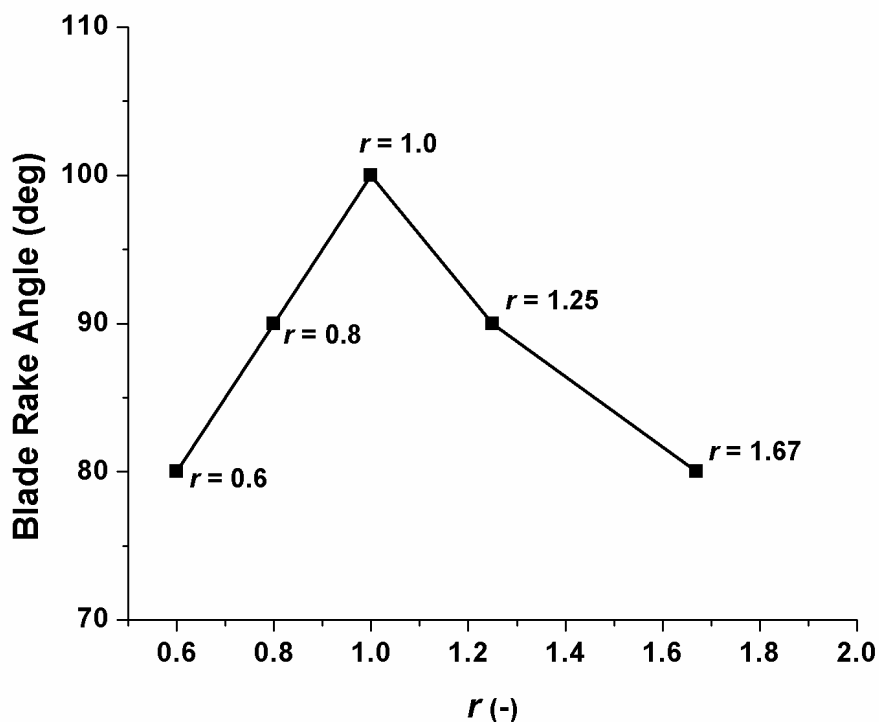
Figure 5.13. Variation of blade-rake angle values (corresponding to the highest values of MMIV) with respect to r.

The highest velocities were obtained for a system without wall friction due to the absence of any slowing down effect by the wall. As shown in Fig. 5.12, the highest MMIVs were obtained for the mixtures having a particle diameter of 6 and 10 mm (i.e., r being 0.6 and 1.67), followed by 8 and 10 mm (i.e., r being 0.8 and 1.25). Mixtures with only 10 mm particles have the lowest MMIV. This is because for a constant blade speed the smaller particles attain higher (instantaneous) velocities.

Fig. 5.14 shows the variation of mean interparticle force magnitude over time for blade-rake angles of 60°, 90°, and 140°. In this Figure, the normal force (Fig. 5.14 a) and the tangential force (Fig. 5.14b) are plotted for r=1.0. A mean interparticle force, e.g., the normal force, was calculated by taking the average of normal contact forces for all particles at a specific time-step and then averaging out this normal force from time step t=0.5 s to t=1.7 s. Note, that in calculating the interparticle forces only the interactions between particles were considered and not between the particles and the walls. In this case, for example, interactions between blue and blue particle, blue and red particles, and between red and red particles were considered only. The mean interparticle force had peaked before the blade movement began due to the particle dropping and settling phase at t < 0.4 s. After the beginning of the blade movement, the mean interparticle forces (both normal and tangential) increased with the simulation time, initially due to inertia because the particles were at rest and, later on, because they were trapped at the end-wall (in y-z plane) of the box. The magnitude of both normal and tangential forces was inversely proportional to the blade-rake angle, i.e., higher for acute blade-rake angles (<90°) and lower for obtuse (>90°) blade-rake angles. If the normal force is denoted by F_n and the tangential force by F_t, they vary in the following order: $F_{n, 60°} > F_{n, 90°} > F_{n, 140°}$ and $F_{t, 60°} > F_{t, 90°} > F_{t, 140°}$. Near the end of the simulation, i.e., at t>1.7 s, both normal and tangential forces exhibited a sudden rise for 60° angle, and to a lesser extent for 90° angle, whereas these forces were constant for the 140° blade-rake angle values.. The sharp increase in the interparticle forces at a smaller blade-rake angle is due to a "particle trap" at the end of the simulation/box. This particle trap is formed when the blade's angle is close to 90° or less near the right end wall in the y-z plane. In general, it can be concluded that the interparticle force profiles are smooth for large blade-rake angles.
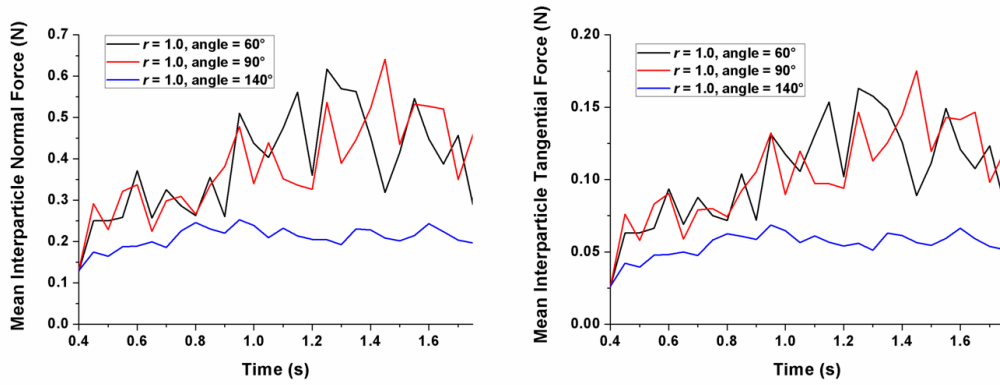
Figure 5.14. Variation of mean interparticle force with respect to simulation time for blade-rake angle of 60°, 90°, & 140° (left: Normal Force, right: Tangential Force).

Fig. 5.15 shows the variation of *time-averaged* mean interparticle contact force magnitude with respect to the blade-rake angle for all values of *r* and selected blade-rake angles of 60°, 90° and 140°. The magnitude of normal and tangential force for all particle contacts, i.e., blue and blue particles, blue and red particles, and red and red particles was averaged over all time steps. These mean interparticle force values were then averaged over a part of the simulation time, i.e., from t=0.5s to t=1.7s. The scale of the y-axis is different for both normal and tangential forces, as shown in Figs. 5.15a and 5.15b, respectively, because the magnitude of the normal force is three to four times greater than that of the tangential force. The results show an inverse relation between a blade-rake angle and the normal (Fig. 5.15a) and the tangential (Fig. 5.15b) forces. If interparticle force is denoted by F_{ip}, then: $F_{ip,60°}>F_{ip,90°}>F_{ip,140°}$. These results are consistent with those reported by Chandratilleke et al. [15] for a cylindrical mixer. They showed that both normal and tangential forces decrease with the value of a blade-rake angle. As the blade-rake angle increased, both normal and tangential interparticle contact forces decrease, implying that for smaller blade-rake angles the interparticle contact forces are higher. This is because at blade-rake angles smaller than 90° the particles are trapped in front of the blade. Although this is intuitively clear, this work quantifies the forces on particles as a function of blade angle for the first time. Thus, it may be an important conclusion for the mixing of shear sensitive materials (e.g., fragile crystals or brittle particles) to use obtuse blade angles in order not to change the particles' integrity. It is to be noted that the mean force is spatially averaged over all contacts in the particle bed.

Thus, the regions with the highest particle interaction forces may not be identified. Such a more refined analysis has been addressed to future work.
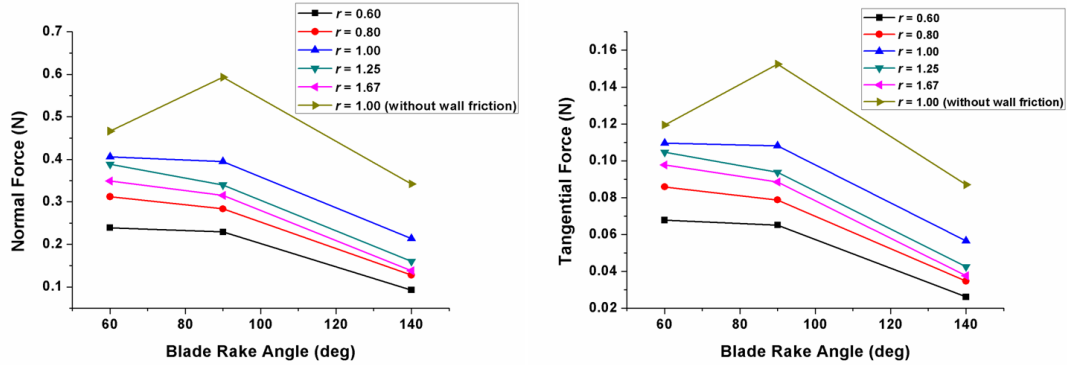
Figure 5.15. Variation of time-averaged mean interparticle force with respect to blade-rake angle and r-values (left: Normal Force, right: Tangential Force), Note: y-axis scale is different in both cases.

The absence of wall friction showed an increase in both normal and tangential forces in the acute and obtuse angle ranges (including blade angle of 90°) for $r = 1.0$. This is because the system without wall friction experience higher instantaneous particle velocities (Fig. 5.12), resulting in higher normal and tangential interparticle forces. However, the highest magnitude of interparticle force is exhibited at 90° followed by 60° and 140°. This is due to the absence of wall friction which greatly reduces the "particle trapping" effect at 60° and the particles are simply pushed over against the end-wall (in y-z plane) of the box.

As far as the effects of r on the interparticle force are concerned, both normal and tangential forces decreased with an increasing ratio of smaller particles in the system as shown in Fig. 5.16.

Fig. 5.16 was produced from Fig. 5.15 when time-averaged mean interparticle force values were averaged for all three angles of 60°, 90° and 140° and then plotted with respect to *r-value*s. Both figures are almost identical except the y-axis values which are 3-4 times higher for normal force compared to the tangential force. The highest forces, both normal and tangential, were observed for *r-value* of 1.0 followed by *r-value*s of >1.0, i.e., 1.25 and 1.67 as shown in Fig. 5.16a for the normal force and Fig. 5.16b for tangential

force. The systems with *r-value*s <1.0, i.e., 0.6 and 0.8 had the lowest normal and tangential force values, since at a constant blade speed the particle system with a higher number of larger particles experiences higher normal and tangential interparticle forces, which are smaller if the smaller particles are put on top.
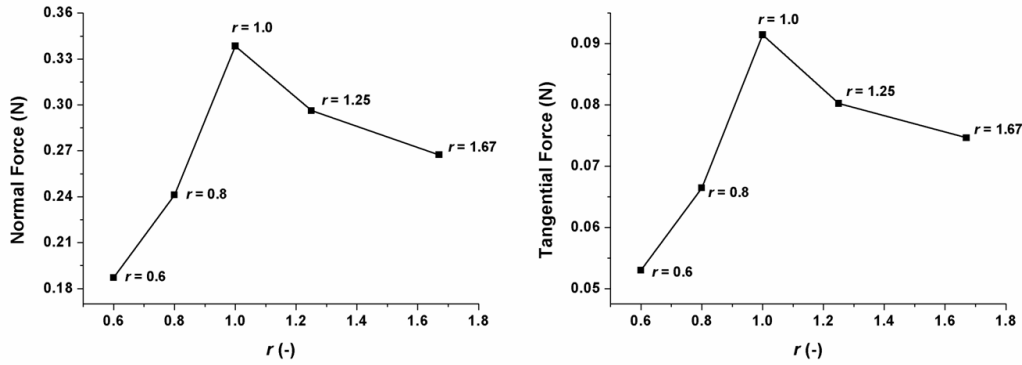
Figure 5.16. Variation of time-averaged mean interparticle force values (averaged for all three angles of 60°, 90° and 140°) with respect to r-values (left: Normal Force, right: Tangential Force), Note: y-axis scale is different in both cases.

Fig. 5.17 shows the variation of the average blade force as a function of time for *r*=1.0 and selected blade-rake angles of 60°, 90°, and 140°. Average blade forces were calculated by taking the average of the total force magnitude on the blade at all time-steps and then averaging these values from time step t=0.5 s to t= 1.7 s. In Fig. 5.17, average blade force values are plotted against the simulation time. Blade force values increase with time, except for the 140° blade-rake angle. The magnitude of the blade force was higher for smaller angles, i.e., if blade force is denoted by F_b, then $F_{b,60°} > F_{b,90°} > F_{b,140°}$. As discussed in previous sections, the interparticle forces for acute blade-rake angles and angles close to 90° were higher than the force for the obtuse angles due to a "particle trap" at the end of the simulation/box. This particle trap is formed when the blade has an angle close to 90° or less near the right end wall in the y-z plane. Thus, the blade (with a constant speed) experiences more force when passing through the particle bed. However, the blade force does not depend only on the interparticle contact force but on the number of contacts between particles and blade.
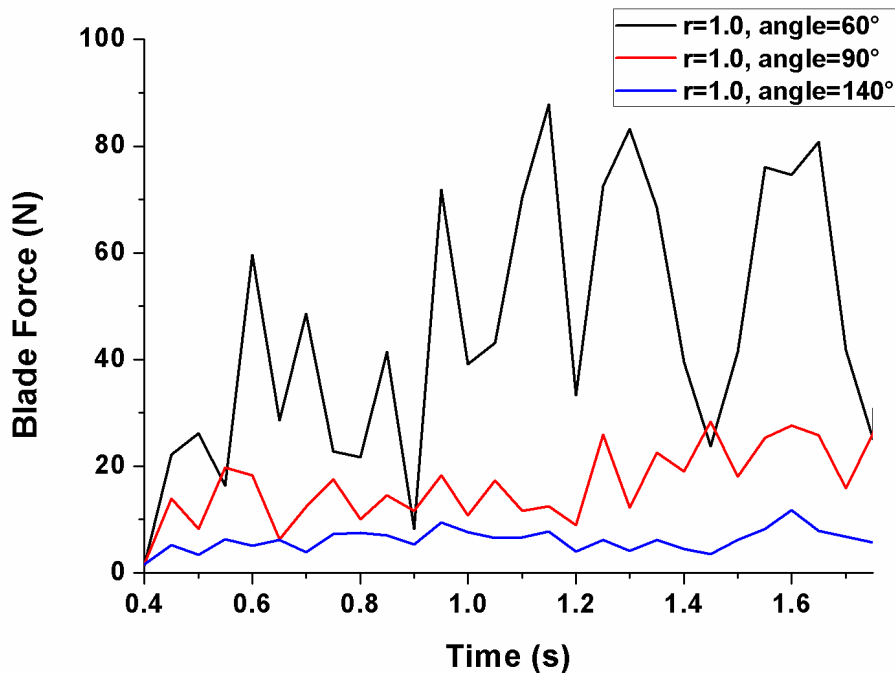
Figure 5.17. Variation of magnitude of the force on the blade vs. simulation time for r=1.0 and selected blade-rake angles of 60°, 90° and 140°.

The dependence of the time-averaged mean force on the blade-rake angle and the *r*-value was also investigated (Fig. 5.18). It is to be noted that only angles of 60° and higher have been included in this figure (as angles even more acute led to particle-locking phenomena – see below). In Fig. 5.15 it was shown that particle systems with a higher number of larger particles exhibit greater interparticle forces at the same constant blade speed. In Fig. 5.18 the blade force varies almost the same way as suggested in Fig. 5.15 except for the case without wall friction, where particles experience higher interparticle normal and tangential forces, but blade forces are lower. This is because in the absence of any resistance to the article bed movement in the form of wall friction. (This is also an important result for the mixing of fragile particles: although blade forces and torque might be low for systems with very low wall friction on smooth or solvent-lubricated walls, the inter-particle forces are still high).

For the same particle systems, i.e., 6 and 10mm (*r*=0.6 or 1.67) and 8 and 10mm (*r*=0.8 or 1.25), the blade force was nearly the same for obtuse blade-rake angles, including 90°. However, for acute angles, e.g., 60°, the blade force was higher for smaller

*r-value*s. This is because interparticle forces, as discussed previously, are larger for acute angles due to the formation of a "particle trap" at the end of the simulation/box. When smaller particles are on the top, the majority of larger particles are in the trap, thus increasing the blade force. When larger particles are at the top, they are not entrapped, and hence contribute to a lesser extent to the blade force.

Absence of wall friction shows no significant effect at higher blade rake angle values, as shown in Fig. 5.18. The blade force is almost the same at higher blade rake angles e.g. 140° for $r = 1.0$ as shown by the two lines, i.e., $r = 1.0$ and the same $r = 1.0$ but without wall friction. The effect of absence of wall friction is more visible at lower blade angles. The blade force is much less in the absence of wall friction in the acute blade angle range including the blade rake angle of 90°. It is significantly less at even lower angles, i.e., at 60° as expected. The reason for this low blade force is the absence of any resistance for the movement of particles in the system having no wall friction. At lower angles, the blade force is significantly lower because the 'particle trap' at these angles is much less effective in the absence of any wall friction.
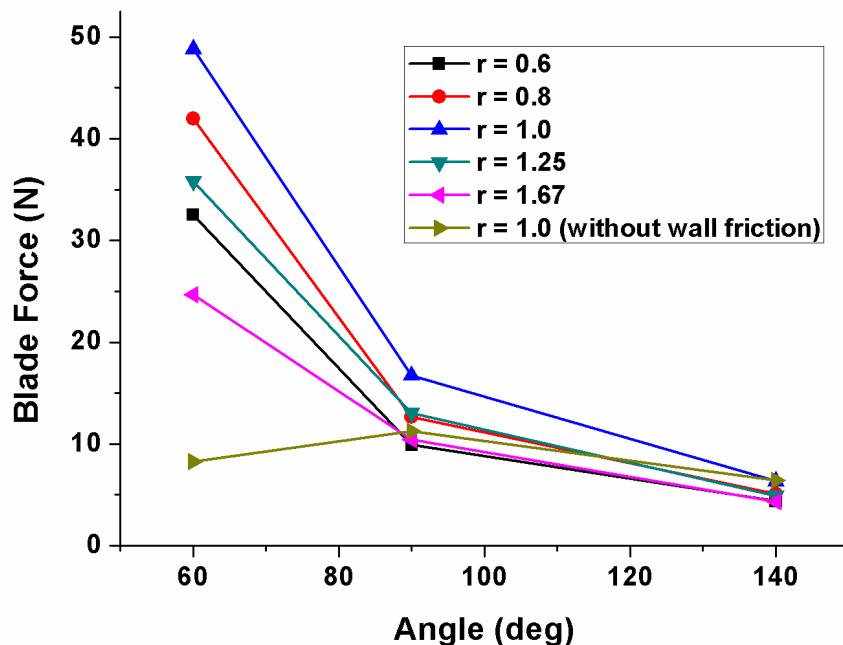
Figure 5.18. Variation of time-averaged mean blade force with respect to the blade-rake angle and r-values.

A study of small blade-rake angles (e.g., 40°) revealed that the particles experienced much higher interparticle and blade forces than at all other blade angles. This would correspond essentially to a locking of the mixer. Fig. 5.19 shows a variation of the time-averaged mean interparticle and blade forces with respect to different *r-value*s for the blade angle of 40°. Both interparticle and blade forces varied inversely with *r-value*s. The interparticle forces were significantly higher than in other cases, which resulted in erratic particle motion in some regions of the computational domain. Hence, it can be concluded that for angles below 60° the interparticle and the blade forces increase tremendously due to the particles trapped in front of the blade.
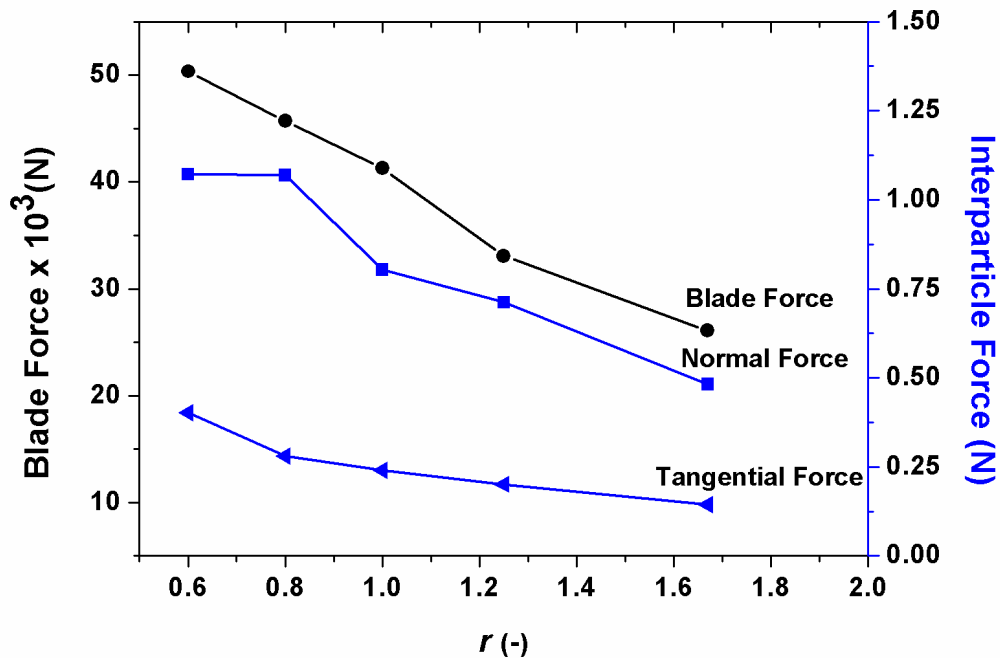
Figure 5.19. Variation of time-averaged mean interparticle force (right y-axis) and blade force (left y-axis) with respect to different r-values, for blade-rake angle of 40°.

Fig. 5.20 shows the effects of a blade-rake angle on mixing performance using MGMMI to quantify the mixing performance. Mixing is perfect when MGMMI is equal to 1.0. This Figure shows quite interesting results for a wide range of blade-rake angles and various ratios of the particle diameters.

When the top particles were smaller than the bottom ones, i.e., for *r* < 1.0, mixing performance, as indicated by the MGMMI, was poor for higher angles. The

mixing performance began to increase with lower angles until at around 70-80° when a maximum was reached. For even smaller angles the mixing performance decreased again. Thus, the mixing efficiency was the highest at a blade-rake angle of 70-80° for $r < 1.0$, i.e., for the ratios 0.6 and 0.8. Both cases, especially the case with r=0.6, however, showed a slight dip in the beginning, i.e., starting from blade angle of 150° until around 130°.

For $r = 1.0$, the trend was also almost the same. The mixing performance was almost inversely proportional to the blade-rake angle and increased up to 80° with decreasing angle. Then, mixing performance began to decrease at lower angles. In this case, the mixing performance was the highest at around 80°, i.e., at an angle almost similar to that for $r < 1.0$.
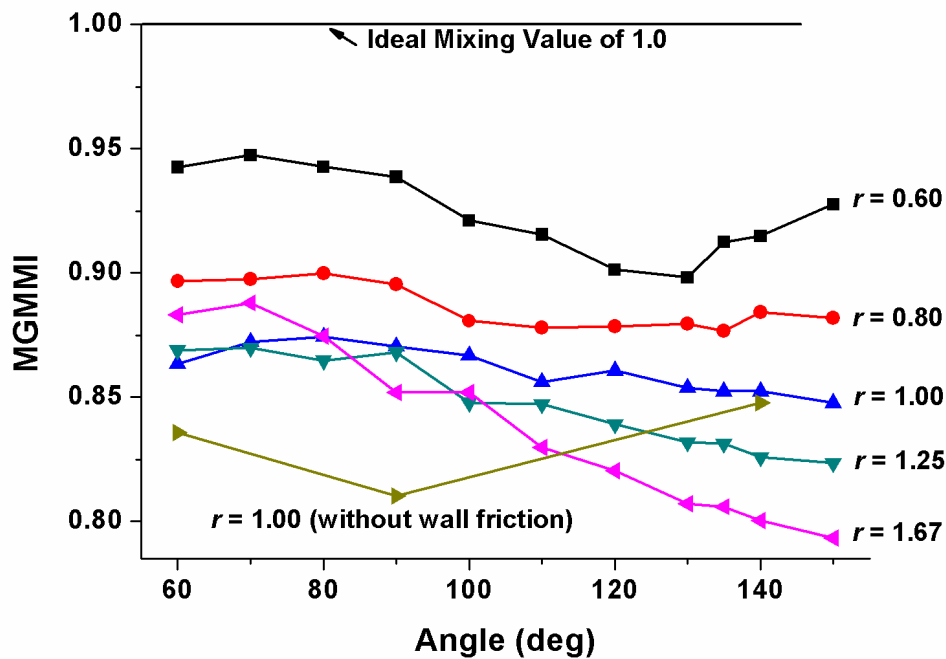
Figure 5.20. Effects of blade-rake angles and particle size on mixing performance using MGMMI.

When large particles were on top and smaller particles were on the bottom, i.e., for $r > 1.0$, mixing performance showed the same trend as for r=1.0, and the highest mixing performance was again at around 70°. The reason for the highest mixing performance at around 70-80° is that for more or less perpendicular positions more of

the blade surface area is interacting with the flow of particles, which increases the "resistance" to the particles, hence resulting in greater convective-shear mixing and overall better mixing performance than at other blade angles. At these lower angles the forces transmitted into the powder bed are significant, thus causing shear and diffusive mixing to occur. For even smaller angles, the forces increase. However, the flow itself is not conducive for mixing, as in front of the blade pockets of particles are formed that do not mix with the rest of the particles (recall the left column of Fig. 5.11). Thus, there is an optimal combination between flow and forces transmitted into the bed.

Furthermore, Fig. 5.20 illustrates that for bigger blade-rake angles the difference in mixing performance is more significant than for smaller blade angles for various *r-value*s. This means that at larger blade-rake angles the value of r plays an important role for the mixing performance and that filling-protocols do affect the performance of the mixer. Large particles should be filled first. If the mixing performance efficiency is denoted by η then $\eta_{r=0.6} > \eta_{r=0.8} > \eta_{r=1.0} > \eta_{r=1.25} > \eta_{r=1.67}$, although in the optimal angle range the differences decrease.

Mixing performance was also studied for same-sized particles ($r = 1.0$) without wall friction. The difference in mixing performance was not significant at higher angles, such as 140°. For smaller angles, i.e., 90° and 60°, the mixing performance was lower in the absence of wall friction as also observed by Remy et al. [9-11].

Fig. 5.21 shows the same results as Fig. 5.20, i.e., the effect of blade-rake angles on mixing performance using MGMMI. However, in this Figure the regions in the beginning and at the end of the box were removed for the calculation of the MGMMI, i.e., 15% of the box volume at both ends was eliminated. This Figure shows that for lower-values of r, i.e., r=0.6 and 0.8, the mixing performance was first lower at bigger angles, then increased up to 90° and finally decreased again at smaller angles. Fig. 5.21 also shows that the slope for higher *r-value*s, e.g., *r*=1.67, was larger than that for lower *r-value*s. Thus, for these combinations, the blade angle is very significant. The highest mixing performance suggested by this Figure is in the range of 70° to 90°. For all three cases with $r \geq 1.0$, the highest mixing performance is observed at 70°, whereas for *r*=0.6, it occurs at 90° and at around 80° for *r*=0.8. If the mixing performance efficiency is

denoted by η, then the same conclusion may be drawn as obtained from the discussion of Fig. 5.20, i.e., $\eta_{r=0.6} > \eta_{r=0.8} > \eta_{r=1.0} > \eta_{r=1.25} > \eta_{r=1.67}$ holds in most cases.
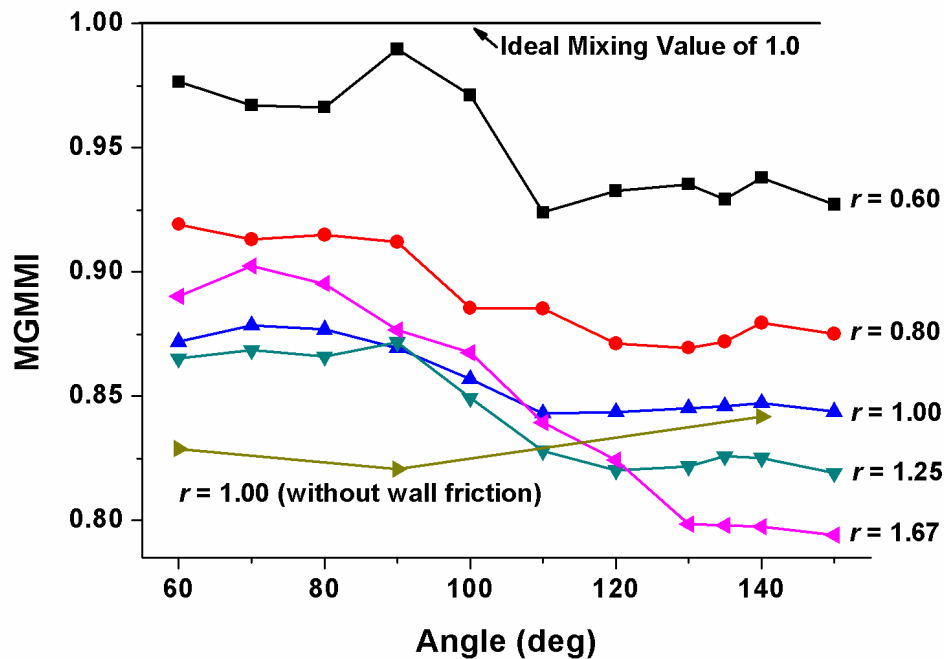
Figure 5.21. Effects of blade-rake angles and particle size on mixing performance using MGMMI while eliminating 15% region in the beginning and end of the box geometry to avoid end effects.

As already discussed above, mixing is usually better for r < 1 than for r > 1 due to sieving segregation mechanism, which favors cases with large particles at the bottom. The difference may, however, reduce at optimal range of angles.

5.5 Effect of Blade Speed

The effect of blade speed on different parameters, such as velocity field and the mixing index MGMMI, is discussed briefly here. From the literature it is well known that the bladed mixer performance is constant, if the number of revolutions is taken as the "time measure".

Fig. 5.22 shows the velocity profiles for three blade speed of a) 0.1 m/s, b) 0.25 m/s, and c) 0.5 m/s. This corresponds to a 5-fold increase in rotation rate. The results are plotted for a blade position at x≈0.5 m, i.e., when the blade has crossed more than

half of the distance in the x direction. The length of the vectors and the color of the field (from blue to red) as discussed previously represent the magnitude of velocities in increasing order. The maximum velocity is different in each case and corresponds to the respective blade speed. As can be seen, the bed height increases slightly with the increase of the blade speed. The blade-relative velocity of the blue region also increases with the increase of blade speed. Thus, a small difference in the velocity fields between the cases can be detected.
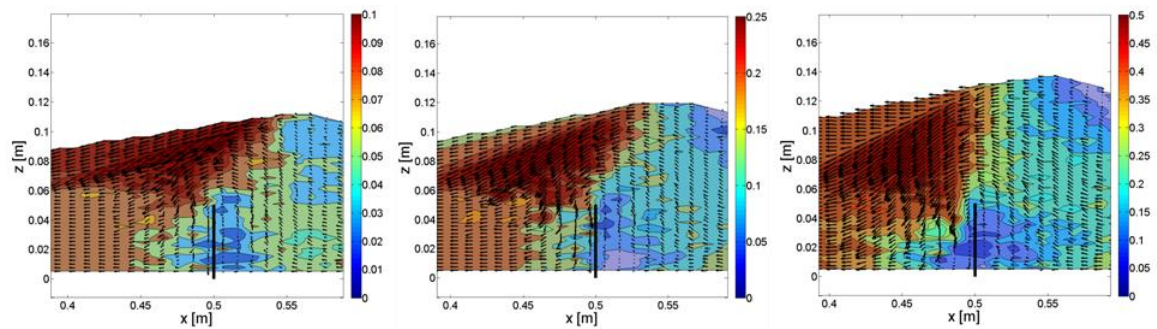
Figure 5.22. Velocity profiles for different blade speeds for blade-rake angle of 90° and r = 1.0 (left: blade speed = 0.1 m/s, center: blade speed = 0.25 m/s, right: blade speed 0.5 m/s)

Fig. 5.23 shows the effect of blade speed on the mixing index MGMMI. The mixing performance is slightly higher for slow blade speeds and decreases at higher blade speeds. However, the decrease is only about 1% and can thus be referred to as negligible. It can be concluded that slower blade speeds increase slightly the mixing performance under the same conditions of blade-rake angle, number or particles, bed height and friction coefficients etc. A more detailed study will focus on this issue.
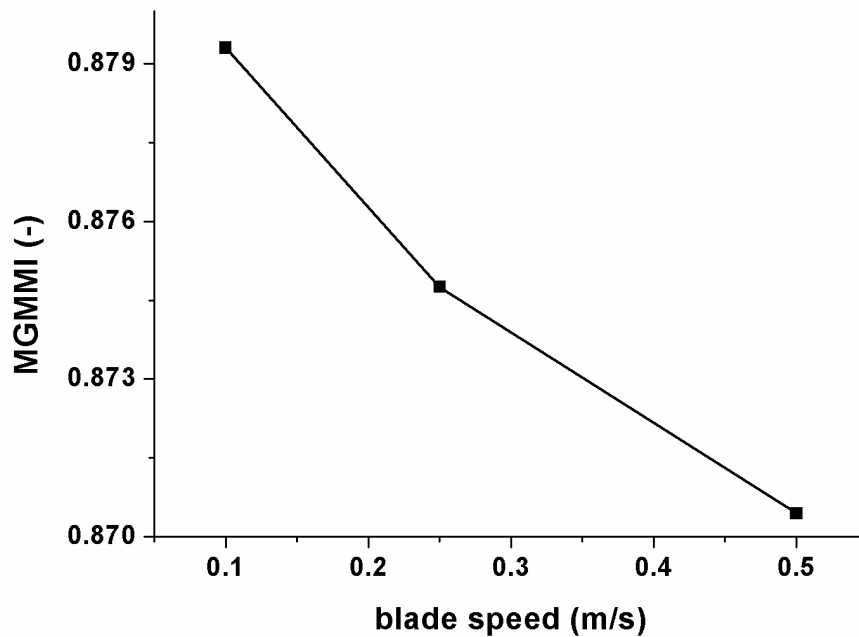
Figure 5.23. Effect of different blade speeds (blade speed variation) on MGMMI for 90° blade-rake angle and r = 1.0.

5.6 Conclusion

The study was intended to understand the impact of granular flow over single blade on mixing performance using DEM simulations. Specifically, the results of this work are:

- Interparticle forces had an inverse relation with the blade-rake angle and, for a constant blade speed, were higher for systems with larger particles. Thus, shear and normal-force sensitive materials (e.g., fragile crystals or brittle particles) should be mixed in blenders with obtuse blade angles in order not to change the particles' integrity.
- Blade forces varied inversely with respect to the blade-rake angle and were higher for systems comprising of larger particles and wall friction.
- At highly acute blade angles of < 60° locking of the mixer may be expected due to rapidly increasing blade forces and particle locking.

- For binary mixtures of different-sized particles, $r=(d_{p,top}/d_{p,bot}) < 1.0$ results in higher mixing performance at a given blade-rake angle than those having $r > 1.0$. This is true for acute and obtuse angle ranges. Thus, larger particles should be filled in a convective powder blender first.

- At a given *r-value* the highest mixing performance was approximately in the range of 70° to 90°, depending on the value of *r*. Thus, slightly acute blade positions are optimal.

- In addition, it was shown that MMIV can be used to quantify mixing performance to avoid complex calculation of mixing indices.

This study can help to understand and to improve the design of industrial convective mixers using two different-sized particles. Future studies will include different blade shapes as well the extension to realistic designs.

5.7 Nomenclature

abs	absolute (-)
C_n	normal damping coefficient (kg.s^{-1})
C_t	tangential damping coefficient (kg.s^{-1})
d_p	particle diameter (m)
$d_{p,top}$	diameter of particles at top, blue-colored (m)
$d_{p,bot}$	diameter of particles at bottom, red-colored (m)
E^*	reduced Young's modulus (-)
$\vec{F}$	force (N)
$\vec{F}_{cont,ij}$	contact force between particle *i* and *j* (N)
$\vec{F}_{drag,i}$	drag force on particle *i* (N)
$\vec{F}_{g,i}$	gravitational force on particle *i* (N)
$\vec{F}_n$	normal force (N)

$\vec{F}_{n-cont,ik}$	non-contact force on particle i by particle k (N)
$\vec{F}_{t}$	tangential force (N)
$\vec{F}_{total,i}$	total force on particle i (N)
I_{i}	moment of inertia (kg.m^2)
m	mass (kg)
m^{*}	reduced particle mass (-)
m_{r}	rolling friction torque (N.m)
$\vec{M}_{ij}$	torque (Nm)
N	total number of particles of type $a+b$ (-)
n	n number of particles of type a (-)
$\hat{n}_{c}$	unit normal vector at contact point (-)
r	$d_{p,top}/d_{p,bot}$
R^{*}	reduced particle radius (-)
t	time (s)
$\vec{v}_{c}$	relative velocity of the two particles at their contact point (m.s^{-1})
$\vec{v}_{c}^{t}$	relative tangential displacement at contact (m)
$\vec{x}$	position in x-direction (m)
x, y, z	position of a particle in x, y, or z direction (m)
$x_{ref}, y_{ref}, z_{ref}$	reference position in x, y, or z directions (m)

Greek Letters

a	blade-rake angle (degree)
δ_{n}	relative normal displacement at contact (m)

δ_{max}	maximum relative tangential displacement when particle starts sliding (m)
μ	friction coefficient (-)
μ_r	rolling friction coefficient (-)
μ'_r	rotational stiffness (N.m)
ρ_p	particle density (kg.m^{-3})
$\vec{\omega}_i$	angular velocity (s^{-1})
$\vec{\omega}_n$	relative angular velocity component in the contact plane (s^{-1})
$\hat{\omega}_n$	unit vector of $\vec{\omega}_n$ (s^{-1})

Subscripts

a, b	type of particles
d	drag
g	gravitational
i	particle i
j	particle j
n	number of type a particles

5.8 References

[1]   S. Adam, D. Suzzi, C. Radeke, J.G. Khinast, An integrated Quality by Design (QbD) approach towards design space definition of a blending unit operation by Discrete Element Method (DEM) simulation. European Journal of Pharmaceutical Sciences 42 (2011) 106-115.

[2]   P.M. Portillo, M.G. Ierapetritou, F.J. Muzzio, Characterization of continuous convective powder mixing processes. Powder Technology 182 (2008) 368-378.

[3]   P.M.C. Lacey, Developments in the theory of particle mixing. Journal of Applied Chemistry 4 (1954) 257–268.

[4]   P.J. Cullen, Food Mixing: Principles and Applications. New York, Wiley-Blackwell (2009).

[5]   J. Bridgwater, Fundamental powder mixing mechanisms. Powder Technology 15 (1976) 215-236.

[6]   R.L. Stewart, J. Bridgwater, D.J. Parker, Granular flow over a flat-bladed stirrer. Chemical Engineering Science 56 (2001) 4257-4271.

[7]   R.L. Stewart, J. Bridgwater, Y.C. Zhou, A.B. Yu, Simulated and measured flow of granules in a bladed mixer - a detailed comparison. Chemical Engineering Science 56 (2001) 5457-5471.

[8]   S.L. Conway, A. Lekhal, J.G. Khinast, B.J. Glasser, Granular flow and segregation in a four-bladed mixer. Chemical Engineering Science 60 (2005) 7091-7107.

[9]   B. Remy, J.G. Khinast, B.J. Glasser, Discrete element simulation of free flowing grains in a four-bladed mixer. AIChE Journal 55 (2009) 2035-2048.

[10]   B. Remy, J.G. Khinast, B.J. Glasser, The effect of mixer properties and fill level on granular flow in a bladed mixer. AIChE Journal 56 (2009) 336-353.

[11]   B. Remy, T.M. Canty, J.G. Khinast, B.J. Glasser, Experiments and simulations of cohesionless particles with varying roughness in a bladed mixer. Chemical Engineering Science 65 (2010) 4557-4571.

[12]   Y.C. Zhou, A.B. Yu, J. Bridgwater, Segregation of binary mixture of particles in a bladed mixer. Journal of Chemical Technology and Biotechnology 78 (2003) 187-193.

[13]   Y.C. Zhou, A.B. Yu, R.L. Stewart, J. Bridgwater, Microdynamic analysis of the particle flow in a cylindrical bladed mixer. Chemical Engineering Science 59 (2004) 1343-1364.

[14]   S. Radl, E. Kalvoda, B.J. Glasser, J.G. Khinast, Mixing characteristics of wet granular matter in a bladed mixer. Powder Technology 200 (2010) 171-189.

[15]   G.R. Chandratilleke, A.B. Yu, R.L. Stewart, J. Bridgwater, Effects of blade-rake angle and gap on particle mixing in a cylindrical mixer. Powder Technology 193 (2009) 303-311.

[16] K. Malhotra, A.S. Mujumdar, H. Imakoma, M. Okazaki, Fundamental particle mixing studies in an agitated bed of granular materials in a cylindrical vessel. Powder Technology 55 (1988) 107-114.

[17] K. Malhotra, A.S. Mujumdar, Particle mixing and solids flowability in granular beds stirred by paddle-type blades. Powder Technology 61 (1990) 155-164.

[18] K. Malhotra, A.S. Mujumdar, M. Miyahara, Estimation of particle renewal rates along the wall in a mechanically stirred granular bed. Chemical Engineering and Processing 27 (1990) 121-130.

[19] K. Malhotra, A.S. Mujumdar, M. Okazaki, Particle flow patterns in a mechanically stirred two-dimensional cylindrical vessel. Powder Technology 60 (1990) 179-189.

[20] B.F.C. Laurent, J. Bridgwater, D.J. Parker, Motion in a particle bed agitated by a single blade. AIChE Journal 46 (2000) 1723-1734.

[21] H.P. Zhu, Z.Y. Zhou, R.Y. Yang, A.B. Yu, Discrete particle simulation of particulate systems: Theoretical developments. Chemical Engineering Science 62 (2007) 3378-3396.

[22] P.A. Langston, U. Tüzün, D.M. Heyes, Continuous potential discrete particle simulations of stress and velocity fields in hoppers: transition from fluid to granular flow. Chemical Engineering Science 49 (1994) 1259-1275.

[23] P.A. Langston, U. Tüzün, D.M. Heyes, Discrete element simulation of granular flow in 2D and 3D hoppers: dependence of discharge rate and wall stress on particle interactions. Chemical Engineering Science 50 (1995) 967-987.

[24] P.A. Langston, U. Tüzün, D.M. Heyes, Discrete element simulation of internal stress and flow fields in funnel flow hoppers. Powder Technology 85 (1995) 153-169.

[25] Y.C. Zhou, B.D. Wright, R.Y. Yang, B.H. Xu, A.B. Yu, Rolling friction in the dynamic simulation of sandpile formation. Physica A 269 (1999) 536-553.

[26] H.P. Zhu, A.B. Yu, Averaging method of granular materials. Physical Review E 66 (2002) 021302.

[27] B.N. Asmar, P.A. Langston, A.J. Matchett, A generalized mixing index in distinct element method simulation of vibrated particulate beds. Granular Matter 4 (2002) 129-138.

[28] A. Sarkar, C.R. Wassgren, Simulation of a continuous granular mixer: Effect of operating conditions on flow and mixing. Chemical Engineering Science 64 (2009) 2672-2682.

[29] H.P. Zhu, Z.Y. Zhou, R.Y. Yang, A.B. Yu, Discrete particle simulation of particulate systems: A review of major applications and findings. Chemical Engineering Science 63 (2008) 5728-5770.

[30] C.A. Radeke, B.G. Glasser, J.G. Khinast, Large-scale powder mixer simulations using massively parallel GPU architectures. Chemical Engineering Science 65 (2010) 6435-6442.

[31] G.D.R. MiDi, On dense granular flow, The European Physical Journal E 14 (2004) 341-365.

[32] H. Zhenghua, L. Xiang, L. Huilin, L. Guodong, H. Yurong, W. Shuai, X. Pengfei, Numerical simulation of particle motion in a gradient magnetically assisted fluidized bed. Powder Technology 203 (2010) 555-564.

[33] W. Shuai, L. Xiang, L. Huilin, L. Guodong, W. Jiaxing, X. Pengfei, Simulation of cohesive particle motion in a sound-assisted fluidized bed. Powder Technology 207 (2011) 65-77.

[34] L. Xiang, W. Shuyan, L. Huilin, L. Goudong, C. Juhui, L. Yikun, Numerical simulation of particle motion in vibrated fluidized beds. Powder Technology 197 (2010) 25-35.

[35] Y. Tatemotoa, Y. Mawatarib, K. Noda, Numerical simulation of cohesive particle motion in vibrated fluidized bed. Chemical Engineering Science 60 (2005) 5010-5021.

[36] F. K. van Willigen, B. Demirbas, N.G. Deen, J.A.M. Kuipers, J.R. van Ommen, Discrete particle simulations of an electric-field enhanced fluidized bed. Powder Technology 183 (2008) 196-206.

6 Single-Blade Convective Powder Mixing: the Effect of the Blade Shape and Angle

The objective of this work was to investigate and optimize some of the parameters on which granular flows depend. For this purpose monodisperse particles of two sizes were used: half of the simulations were performed with 10 and 10 mm particles and half with 2 and 2 mm particles. For the first time, the effects of a blade shape were investigated using the Discrete Element Method (DEM) simulations. Three blade shapes were investigated, i.e., concave, convex and straight. Similarly, for the first time the DEM method was used to study the blade force on various sections of the blade (bottom, middle and top). Mixing performance with respect to the blade shape and blade-rake angle was investigated using Modified Generalized Mean Mixing Index (MGMMI) and maximum mean-instantaneous velocities (MMIV). A wide range of angles, i.e., 40°, 50°, 60°, 70°, 80°, 90°, 100°, 110°, 120°, 130°, 135°, 140° and 150°, was used. In addition, velocity profiles for all cases and the effects of the interparticle contact forces on the blade shape and blade-rake angle were studied.

Keywords: Blade shape, blade-rake angle, blade force, mixing performance, DEM, MMIV, MGMMI

6.1 Introduction

Solid-particle mixing, or powder blending, is an important industrial process, which is crucial for guaranteeing the quality of many products in the chemical and pharmaceutical industries. In the latter case, blending quality directly relates to the content uniformity of pharmaceutical tablets, as poor blending may lead to either super-potent tablets or blanks, endangering the heath of the patients. As a consequence, the understanding of granular mixing, or powder blending, has been a focus of intense interest for many decades. Lacey et al. [1] have defined three types of mixing mechanisms: convective, diffusive and shear mixing. Convective mixing is due to the movement of a large particle group and has a high effective mixing rate on a larger scale. Diffusive mixing is due to the random motion of solid particles and exhibits a slow rate compared to convective mixing. Yet it is responsible for mixing on the micro-scale. Shear mixing is due to the development of slip-failure planes in the powder mixture, e.g., when a chunk of powder slips down along this plane. Shear mixing can occur in convective and high-shear mixers, as well as in tumbling mixers, where a layer of powder avalanches down along a slope plane [2].

In the pharmaceutical industry, a wide variety of industrial mixers (blenders) are employed for solid particle (granular) mixing to blend the small quantities of active pharmaceutical ingredients (APIs) with usually larger amounts of excipients. Most powder blenders can be classified as tumbling and convective mixers. A tumbling blender consists of a closed vessel rotating around one or two axes. There are three commonly-used tumbling blenders classified according to the vessel geometries, i.e., a double cone, a V-blender and a bin blender [3]. Compared to tumbling mixers, convective-bladed mixers have been investigated in more detail using both experimental and simulation techniques. In convective blenders, mixing is achieved by rotating internals, such as blades, paddles or screws in a static vessel [2]. Furthermore, it is important to distinguish the mixers with respect to their mode of operation. Most mixers described above are batch systems, while only a few continuous powder mixing systems have been commercialized. These continuous mixers include ribbon blenders or screw-transport blenders. More details of industrial powder mixing can be found in the literature [2-3].

As stated above, mixers can be classified as tumbling and convective systems. Because of low shear, a tumbling mixer may not be effective for cohesive powders and powder materials that tend to segregate. Thus, convective blenders are more effective and should be applied in the case of cohesive agglomerating powders.

Convective mixers, which are the focus of the current work, have been investigated by using both experimental and simulation techniques [4-18]. Several publications have reported the results using a convective batch mixer with two [4,5,11,12,18] and four [13-17] blades. Some of these publications have employed only experimental techniques [4,13], while others used only simulations [11-12, 14-15, 17-18]. A limited number of publications compared the results via both simulation and experimental techniques [6,16]. Stewart et al. [4] investigated the granular flow over two opposite flat blades using positron emission particle tracking. They observed three-dimensional recirculation zones and found a linear dependence of the particle speed on the blade speed. They also observed that the size of the recirculation zones and the number of blade passes during which the particles remain in these zones decreased with the increase in the fill level and the blade speed. They compared their experimental results with the simulation results in another paper [5]. Some publications have also reported experimental studies of two-dimensional flow over a flat blade in a cylindrical vessel [6] or using paddle type blades [7-9]. Laurent et al. [10] used a single blade to examine the motion in a particle bed via positron emission particle tracking. Zhou et al. [12] investigated the effects of sliding and rolling friction coefficients on the three-dimensional recirculating particle zones. Conway et al. [13] used particle image velocimetry technique to study the velocity fields of a 4-bladed mixer near the top and the wall in near-monodisperse and polydisperse granular materials. They observed three-dimensional recirculating zones and studied mixing and segregation with respect to shear rates. Remy et al. [14] investigated the effect of the blade orientation in 4-bladed mixers on the particle flow patterns and mixing kinetics using DEM simulations, as well as the effects of friction coefficients on mixing. They also studied normal and shear stresses and their dependence on the mixer's height and the friction coefficients of the particles. In another study, Remy et al. [15] investigated the effects of the fill level and other mixer properties (e.g., the vertical blade position from the mixer bottom, wall friction, the mixer diameter and the blade speed) on granular flow characteristics and on mixing.

Remy et al. [16] also studied the effects of varying roughness and the varying blade speed on the granular flow of cohesionless particles using simulations and experiments. Radl et al. [17] studied mixing characteristics of wet granular matter in 4-bladed mixers and observed better mixing rates and performance than those of dry granular matter under certain conditions [17].

In a recent paper by Chandratilleke et al. [18], the blade-rake angle of a cylindrical mixer was investigated using four blades for three blade-rake angles, i.e., 45°, 90°, and 135°. The mixing performance in this work was quantified using Lacey's mixing index. They reported 90° as the angle showing the highest mixing rate. In another recent study, Siraj et al. [19] investigated the effects of the blade-rake angle and particle size ratio $(d_{p,top}/d_{p,bot})$, of polydisperse particles on powder-mixing performance in a rectangular box with a single blade. They quantified the mixing performance via the Modified Generalized Mean Mixing Index (MGMMI) and studied the velocity profiles of various blade angles and the particle size ratios, as well as the variation of the interparticle and blade forces associated with the change in the blade-rake angle and the particle size ratios.

The goal of this work is a more detailed understanding of powder blending. However, instead of investigating the whole mixer, the objective was to gain a detailed understanding of the particle flow across a single blade by studying the impact of single-blade orientation and shape on blending performance and mixing. Thus, the goal of this work was to study the particle flow over a single blade and its impact on mixing as a function of the blade shape and orientation. DEM simulations were carried out to simulate the flow across a single blade.

The geometry of our studies was similar to that used by Siraj et al. in a recent study on single blade mixing [19]. A simple rectangular box with a single blade with three different shapes was used that allows the movement of the blade only in x-direction. Monodisperse particles of two sizes, i.e., 2 mm and 10 mm, were used. The number of particles for the 2 mm case was 15,000 and for 10 mm particles 600. Three blade shapes, i.e., convex, concave and straight blades, were used. The blade rake angles studied were 40°- 150° with 10°-intervals.

6.2 Numerical Method

DEM is a versatile tool for the simulation of granular flows, as it gives a detailed picture of the flow by discretely keeping track of each individual particle. The method is based on the description of interparticle forces and the (linear and rotational) momentum balance for all particles. Every particle is treated discretely and is solved for all the forces acting on it. These forces include contact forces, body forces, hydrodynamic forces and non-contact or cohesive forces, as shown in Figure 6.1.
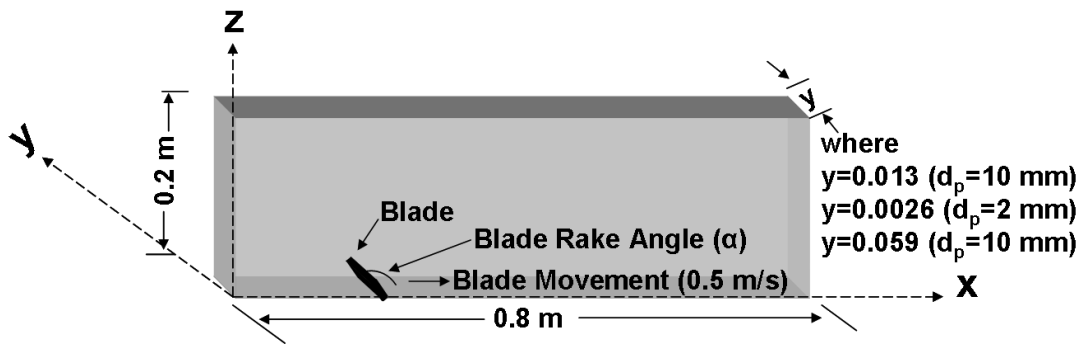
Figure 6.1. Geometry of box used for the simulations.

These forces are then integrated over time to obtain the position and velocity of each particle. Newton's second law of motion for a particle i becomes:

$$m_i \frac{d^2 \vec{x}_i}{dt^2} = \vec{F}_{total,i} = \sum_j \vec{F}_{cont,ij} + \sum_k \vec{F}_{n-cont,ik} + \vec{F}_{g,i} + \vec{F}_{drag,i} \qquad (6.1)$$

Where, m_i is the mass of particle I, and $\vec{x}_i$ is the position of the particle. Integration of this equation gives velocity, and double integration yields the position of particle i. $\vec{F}_{total,i}$ is the sum of all forces acting on particle i and $\sum_j \vec{F}_{cont,ij}$ is the sum of all contact forces between particles i and j. $\sum_k \vec{F}_{n-cont,ik}$ is the sum of all non-contact or cohesive forces between particles i and k. $\vec{F}_{drag,i}$ is the drag force exerted by the surrounding fluid. In granular flows, however, fluid-particle interactions are negligible compared to the contact and other forces. Therefore, the drag force or $\vec{F}_{drag,i}$ can be ignored. $\vec{F}_{g,i}$ is the gravitational force exerted on particle i.

The rotational momentum balance is:

$$I_i \frac{d\vec{\omega}_i}{dt} = \sum_j \vec{M}_{ij} \tag{6.2}$$

In Eq. 6.2, I_i is the moment of inertia, ω_i is the angular velocity, and $\vec{M}_{ij}$ is the torque acting on particle i by particle j.

Various models and numerical schemes are available for solving these equations for translational and rotational motion of each particle. The first term on the right-hand side of Eq. 6.1, i.e., $\sum_j \vec{F}_{cont,ij}$, is the most critical part comprising normal and tangential force components. In our work a simplified Hertz-Mindlin and Deresiewicz model [20-25] was used, which combines the following models for the normal and tangential forces:

- Normal force

$$\vec{F}_n = -\frac{4}{3}E^* \sqrt{R^*}(\delta_n)^{3/2} - C_n(8m^* E^* \sqrt{R^* \delta_n})^{1/2}.(\vec{v}_c.\hat{n}_c)\hat{n}_c \tag{6.3}$$

- Tangential force

$$\begin{aligned}\vec{F}_t = &-\mu|\vec{F}_{n,e}|(1-(1-|\vec{v}_c^t|/\delta_{max})^{3/2})\hat{v}_c^t \\ &+ 2C_t(1.5\mu m^*|\vec{F}_{n,e}|.\sqrt{1-|\vec{v}_c^t|/\delta_{max}}/\delta_{max})^{1/2}.(\vec{v}_c \times \hat{n}_c)\times\hat{n}_c\end{aligned} \tag{6.4}$$

The simulations were performed using EDEM developed by DEM Solutions, and the model selected was the Hertz-Mindlin model, as mentioned above. For more details of the implementation refer to our recent publication [19].

The mixing performance was quantified using a modified generalized mean mixing index [19] i.e.,

$$MGMMI = 1 - \frac{abs(1-GMMIx_a) + abs(1-GMMIy_a) + abs(1-GMMIz_a)}{3} \tag{6.5}$$

For two types of particles a and b, the generalized mean mixing index of a type particles, i.e., $GMMI_a$ is calculated as the sum of mean positions of n number of a type particles divided by the sum of mean positions of all N number of $a+b$ type of particles. $GMMI_a$ is calculated in x, y or z directions, depending on whether positions x, y or z are used in Eq. 6.5.

$$GMMIx_a = \frac{\left[\sum_{p=1}^{n} \frac{(x_p - x_{ref})}{n} \right]}{\left[\sum_{q=1}^{N} \frac{(x_q - x_{ref})}{N} \right]} \qquad GMMIy_a = \frac{\left[\sum_{p=1}^{n} \frac{(y_p - y_{ref})}{n} \right]}{\left[\sum_{q=1}^{N} \frac{(y_q - y_{ref})}{N} \right]} \qquad GMMIz_a = \frac{\left[\sum_{p=1}^{n} \frac{(z_p - z_{ref})}{n} \right]}{\left[\sum_{q=1}^{N} \frac{(z_q - z_{ref})}{N} \right]}$$

where x_{ref}, y_{ref}, and z_{ref} are the reference positions in x, y and z directions that are zero in our box case (i.e., x_{ref}, y_{ref}, and z_{ref} constitute the origin).

GMMI was originally introduced by Asmar et al. [26] and was later modified, used and explained in a study by Siraj et al. [19].

6.3 Simulation Set-up

Details of the parameters used for the simulations are given in Table 6.1. Each case comprised mono-sized particles unlike our previous study where three particle sizes and their combinations were used [19]. Simulations were run using either 10 mm red and blue particles or 2 mm red and blue particles. The effects of the particle diameter were discussed previously by Remy et al [14] and Siraj et al. [19].

Table 6.1. Parameters used for simulations.

Parameter	Value	Units
Box dimensions (length × width × height)	0.8×0.013×0.2 (2-D cases using 10 mm particles) 0.8×0.0026×0.2 (2-D cases using 2 mm particles) 0.8×0.059×0.2 (3-D cases using 10 mm particles)	m
Blade Shape	concave, convex, straight	-
Blade rake angles used	40, 50, 60, 70, 80, 90, 100, 110, 120, 130, 135, 140, 150	deg
Material (Particle /Blade/Container)	Glass/Steel/Steel	-
Particle Diameter (d_p)	2, and 10	mm
Number of particles	600 (2-D cases using 10 mm particles) 15000 (2-D cases using 2 mm particles) 2720 (3-D cases using 10 mm particles)	-
Particle Density, glass (ρ_p)	2456	kg/m³
Poisson Ratio	0.25	-
Shear Modulus	2.2×10^8	Pa
Coefficient of Restitution	0.3 (for glass-steel) and 0.5 (for glass-glass),	-
Coefficient of Static Friction	0.5 and 0.0 for cases without wall friction	-
Coefficient of Rolling Friction	0.01 and 0.0 for cases without wall friction	-

Figure 6.1 shows the box geometry. Three types of rectangular boxes were considered. All boxes had the same dimension in x-dir (length) and z-dir (height) but had varying widths in y direction, depending on the particle size and the case of simulation 2D versus 3D. In 2D simulations only one layer of particles exist, while in the 3D simulations the particle bed has a certain depth. The 2D simulations were employed to mimic a situation with a cut-view section of a flow across the blade in 3-D. Two types of boxes were employed for the study in 2-D with particle sizes of 10 mm and 2 mm, depending on the size of the particles. The total number of particles in the first case was 600 and in the second case 15000. The difference in the number of particles is due to their diameters, since for the same fill level and box length the number of smaller particles is much higher (15,000 in this case) than that of larger particles. The third box

was used to study the same effects in 3-D using 10 mm particles. The dimensions of the boxes are provided in Table 6.1.

Figure 6.2a shows the considered blade-rake geometry angles for all three blade shapes, i.e., concave, convex and straight. Figure 6.2b shows the construction of the convex and concave blade geometries. The blade width of 0.05 m was divided into five equal sections, each 0.01 m long, which were numbered from 1 to 5 beginning from the bottom. The angle of the bottom section (i.e., blade 1) with the base of the simulation box was taken as the blade rake angle for the curved blade geometries. For the convex shape, the angle of each subsequent blade section was increased by 5°, whereas for the concave shape it was decreased by 5°, as shown in Figure 6.2b. In general, angles smaller than 90° are termed *acute*, while the angles larger than 90° are called *obtuse*. In all simulations, the gap between the bottom of the box and the blade was zero.

_____
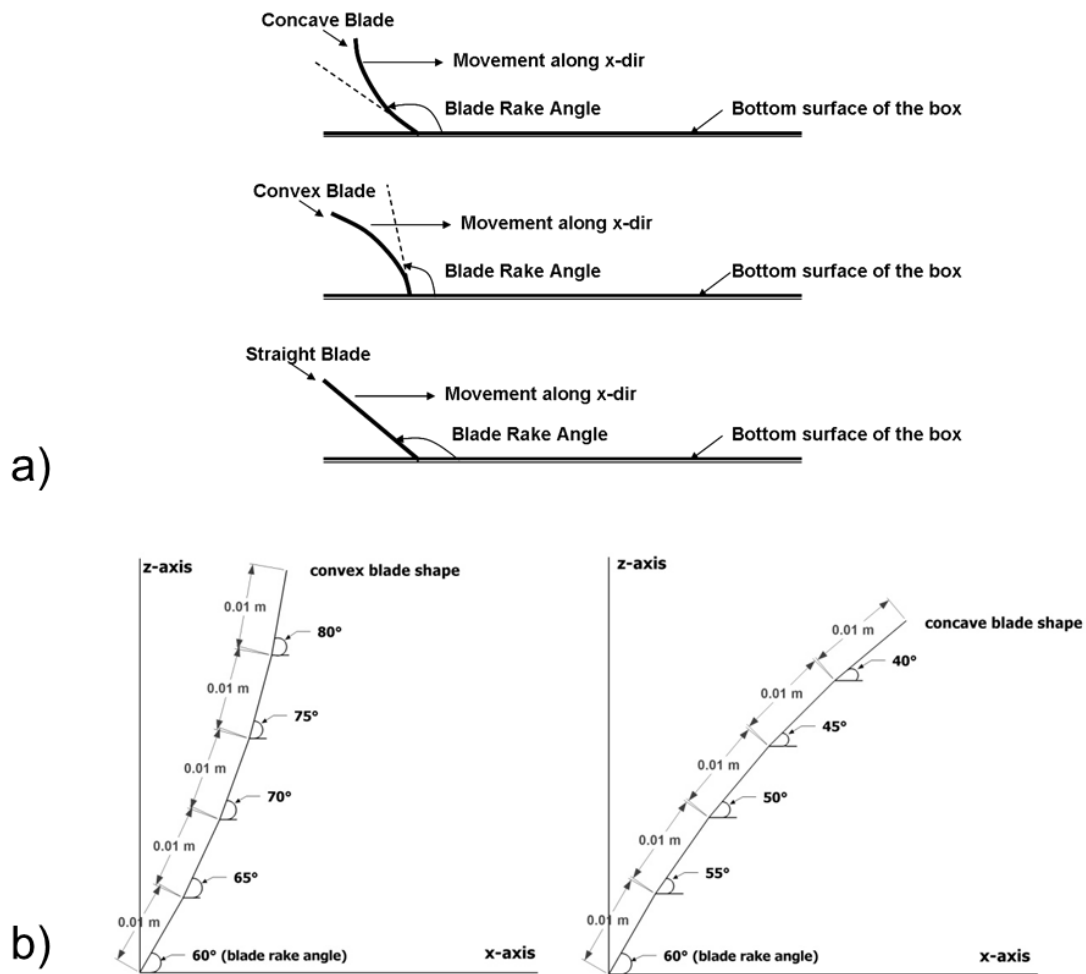
Figure 6.2. a) Three blade shapes and blade rake angle, b) Construction of convex and concave blade shapes.

The starting point for all simulations was achieved by dropping particles in the box, and the procedure was the same as used in our previous study [19], i.e., first filling in one type of particles and then adding the second type on top.

The various simulations that were run are summarized in Table 6.2. Case-A, Case-B and Case-C used 10 mm particles for concave, convex and straight blade shapes, respectively, with a blade speed of 0.5 m/s, including the wall friction effects. Case-D involved 10 mm particles, a straight blade shape with the same blade speed (0.5 m/s) but without wall friction, mimicking a layer in moving bed with no lateral velocity gradients or lateral friction. Case-E comprises simulations with 10 mm particles and a straight blade shape and wall friction with a reduced blade speed of 0.05 m/s. For Case-F the

same 10 mm particles and a straight blade shape with the blade speed of 0.5 m/s were used, and the wall friction effects were included. However, in this case a 3-D box was considered, allowing five 10 mm-particles in a side-by-side arrangement. Case-G, Case-H and Case-I utilized 2 mm particles with concave, convex and straight blade shapes, respectively, with a blade speed of 0.5 m/s and including wall friction. Finally, in Case-J 2 mm particles and a straight blade shape with the blade speed of 0.5 m/s were considered without the wall friction effects.

Table 6.2. Simulation cases – summary.

Category	Particle Diameter (mm)	No. of Particles	Blade Shape	Blade-rake Angle (deg)
Case-A (with wall friction) blade speed=0.5 m/s	10	600 (300 blue + 300 red)	Concave	40, 50, 60, 70, 80, 90, 100, 110, 120, 130, 135, 140, 150
Case-B (with wall friction) blade speed=0.5 m/s	10	600 (300 blue + 300 red)	Convex	40, 50, 60, 70, 80, 90, 100, 110, 120, 130, 135, 140, 150
Case-C (with wall friction) blade speed=0.5 m/s	10	600 (300 blue + 300 red)	Straight	40, 50, 60, 70, 80, 90, 100, 110, 120, 130, 135, 140, 150
Case-D (without wall friction) blade speed=0.5 m/s	10	600 (300 blue + 300 red)	Straight	50, 60, 70, 80, 90, 100
Case-E (with wall friction) blade speed=0.5 m/s	10	600 (300 blue + 300 red)	Straight	60, 90, 140
Case-F (3-D with wall friction) blade speed=0.5 m/s	10	2720 (1360 blue + 1360 red)	Straight	50, 60, 70, 80, 90, 100
Case-G (with wall friction) blade speed=0.5 m/s	2	15000 (7500 blue + 7500 red)	Concave	40, 50, 60, 70, 80, 90, 100, 110, 120, 130, 135, 140, 150

Category	Particle Diameter (mm)	No. of Particles	Blade Shape	Blade-rake Angle (deg)
Case-H (with wall friction) blade speed=0.5 m/s	2	15000 (7500 blue + 7500 red)	Convex	40, 50, 60, 70, 80, 90, 100, 110, 120, 130, 135, 140, 150
Case-I (with wall friction) blade speed=0.5 m/s	2	15000 (7500 blue + 7500 red)	Straight	40, 50, 60, 70, 80, 90, 100, 110, 120, 130, 135, 140, 150
Case-J (without wall friction) blade speed=0.5 m/s	2	15000 (7500 blue + 7500 red)	Straight	50, 60, 70, 80, 90, 100

In all simulations half of the particles were blue and the rest were red. The particles were assumed to be made of glass, whereas the blade and the box were made of steel, as in an industrial mixer. Except for Case-E, the blade was given a translational motion of 0.5 m/s in x- direction (after 0.4s of settling time). The blade movement was stopped at t=1.9 s for the blade speed of 0.5 m/s and at t=15.4 s for the blade speed of 0.05 m/s at the same x-position in the box.

The dimensionless shear rate I is one of the most important parameters determining the granular flow regime [27]:

$$I = \frac{\dot{\gamma} \cdot d_p}{\sqrt{P/\rho}} \tag{6.6}$$

Here $\dot{\gamma}$ is the shear rate, d_p is the particle diameter, P is the characteristic normal stress (i.e., the particle pressure) and ρ is the bulk density. The dimensionless parameter I describes the relative importance of inertia to the normal stress in the particle bed. For vertical free surface flows, the characteristic normal stress can be approximated [27] by:

$$P = \rho \cdot g \cdot h \tag{6.7}$$

and the shear rate can be approximated [27] by:

$$\dot{\gamma} = V/h \tag{6.8}$$

where h and V are the characteristic bed height and bed velocity, respectively. Inserting these approximations into the definition of the dimensionless shear rate yields:

$$I = \frac{V \cdot d_p}{\sqrt{g \cdot h^3}}$$

(6.9)

If the parameter I is above 10^{-2}, the quasi-static regime (under which the effective friction coefficient is constant) is no longer valid, and the transition to the dense inertial regime has reached [27]. As discussed by Remy et al. [15] and others, in the quasi-static regime of granular flows the blade speed has no significant impact on mixing.

As summarized in Table 6.3, the dimensionless shear rate I was 0.0942 for 2-D cases with 10 mm particles and the blade speed of 0.5 m/s, 0.018 for 2-D cases with 2 mm particles and the blade speed of 0.5 m/s, 0.1087 for 3-D cases with 10 mm particles and the blade speed of 0.5 m/s, and 0.0094 for 2-D cases with 10 mm particles and the blade speed of 0.05 m/s. Thus, the process was not in the quasi-static regime for all cases with the blade speed of 0.5 m/s, regardless of whether the particles were 10 mm or 2 mm. For lower blade speeds (Case E) the quasi-static regime was reached. However, the influence of speed was minor, as shown below.

All cases (A-J) were studied with blade-rake angles of 40° to 150° with 10° intervals (plus a simulation at 135°) as shown in Table 6.2.

Table 6.3. Different I values.

Category	I (dimensionless shear rate) values
2-D for 10 mm particles and blade speed of 0.5 m/s	0.0942
2-D for 2 mm particles and blade speed of 0.5 m/s	0.0180
3-D for 10 mm particles and blade speed of 0.5 m/s	0.1087
2-D for 10 mm particles and blade speed of 0.05 m/s	0.0094

Finally, Figure 6.3a shows snapshots for three blade shapes at 140° blade-rake angle in the initial state (after settling of 10 mm particles) for the blade-rake angle of 140°.

Figure 6.3b shows the same cases for 2 mm particles. As observed in the earlier study [19], the interface between the blue and red particles after particle filling was only approximately planar.
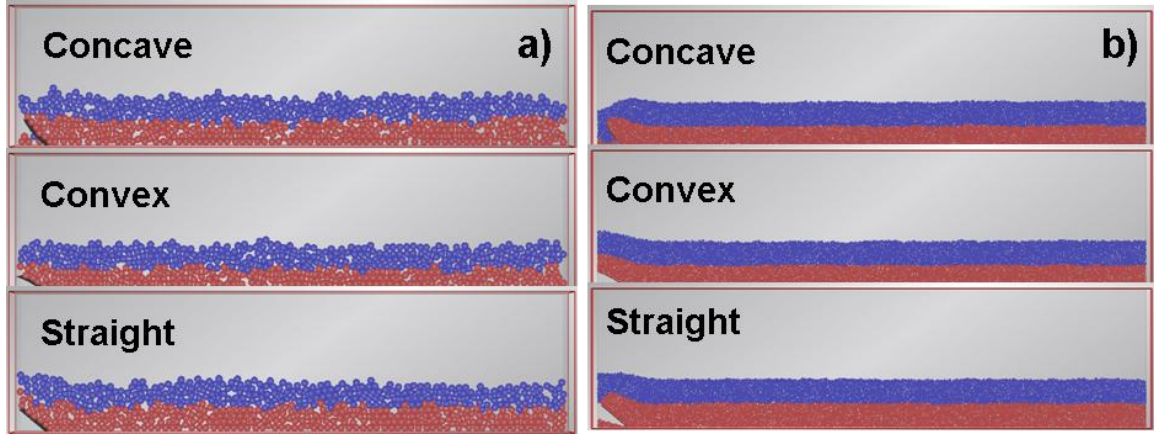
Figure 6.3. Simulation for blade-rake angle of 140° at initial state; a) 10 mm particles,   b) 2 mm particles.

6.4 Results and Discussion

6.4.1 General

First, the effect of a single blade pass through the box (from left to right) is visualized as a snapshot at the end of the simulation for several selected cases. Figures 6.4 to 6.7 illustrate the effects of a single blade pass as it moved from left to right in the box.

Figure 6.4 shows selected 2-D simulations for 10 mm particles. For larger blade angles (e.g., at 140°) the particle bed-height variation and the impact on mixing was minimal. Additionally, blade shape had little impact. For smaller blade angles, the impact of shape was significant and the bed height variations were maximal at angles around 80°-100°. This was consistent with the results reported in the previous study [19]. The bed-height variation was the smallest for convex shape, followed by the straight and then for concave shapes. If the bed-height is denoted by h, then the bed height variation is $(\Delta h)_{concave} > (\Delta h)_{straight} > (\Delta h)_{convex}$.
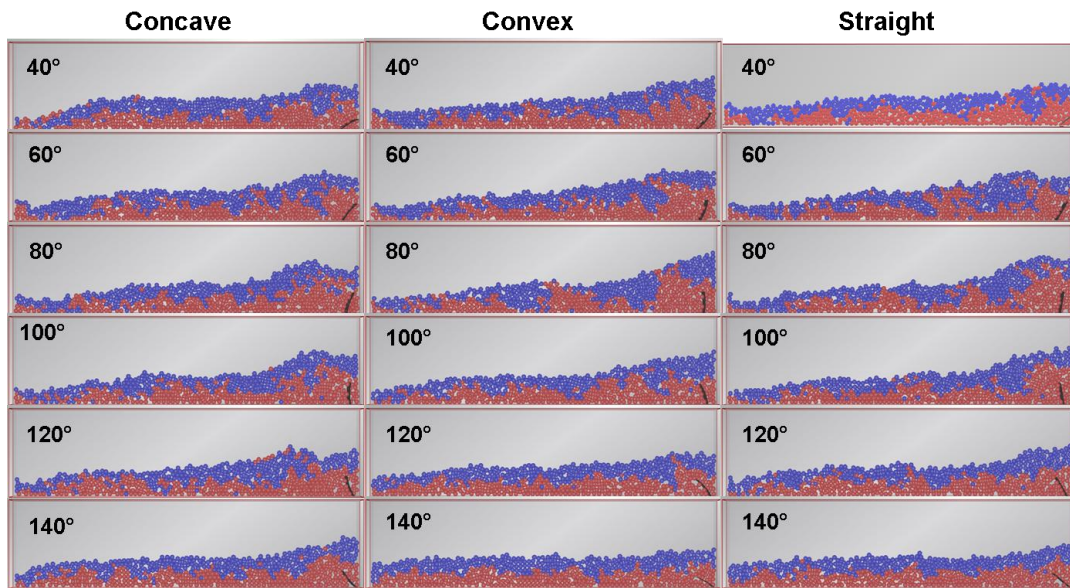
Figure 6.4. Final state for selected blade-rake angles and three blade shapes (concave, convex, and straight) for 10 mm particles.

As already mentioned above, the convex and concave blade shapes comprised five blade segments. Most of the straight-blade simulations (for 10 mm particles) were run using both single one-piece blade (0.05 m) and five blade segments (0.01 m each). The straight blade with the five blade segments was constructed in such a way that all five segments were at the same angle, unlike the curved-shape blades. However, different sections of the blade do not experience the same force. This is consistent with the results previously reported by Chandratilleke et al. [18] in the figure showing force network for 45° (p. 309). They also observed the largest force near the bottom of the blade at 45° blade angle. The 'total force' in our case for either single one-piece or five blade segments is almost the same (see Table 6.4, first data row and last two columns).

Table 6.4. Total blade force (N) values for blade rake angle of 40°.

Particle Size	Total blade force (N) using different particle shapes for α=40°			
(diameter, mm)	**Concave** (comprising 5 blade segments)	**Convex** (comprising 5 blade segments)	**Straight** (comprising 5 blade segments)	**Straight** (using single one-piece blade)
10	4788	4659	4502	4666
2	1682	1040	-	1438

For smaller particles, i.e., 2 mm, the effect of the blade-rake angle on the bed height variation was insignificant, as shown in Figure 6.5. The effect of the blade shape on the bed height variation for smaller particles was also minor. Furthermore, popping-up of the particles for highly acute angles, e.g. at 40°, was not observed for smaller particles (2 mm diameter) for all three blade shapes (see Figure 6.5) for either single one-piece or five-segment blades.
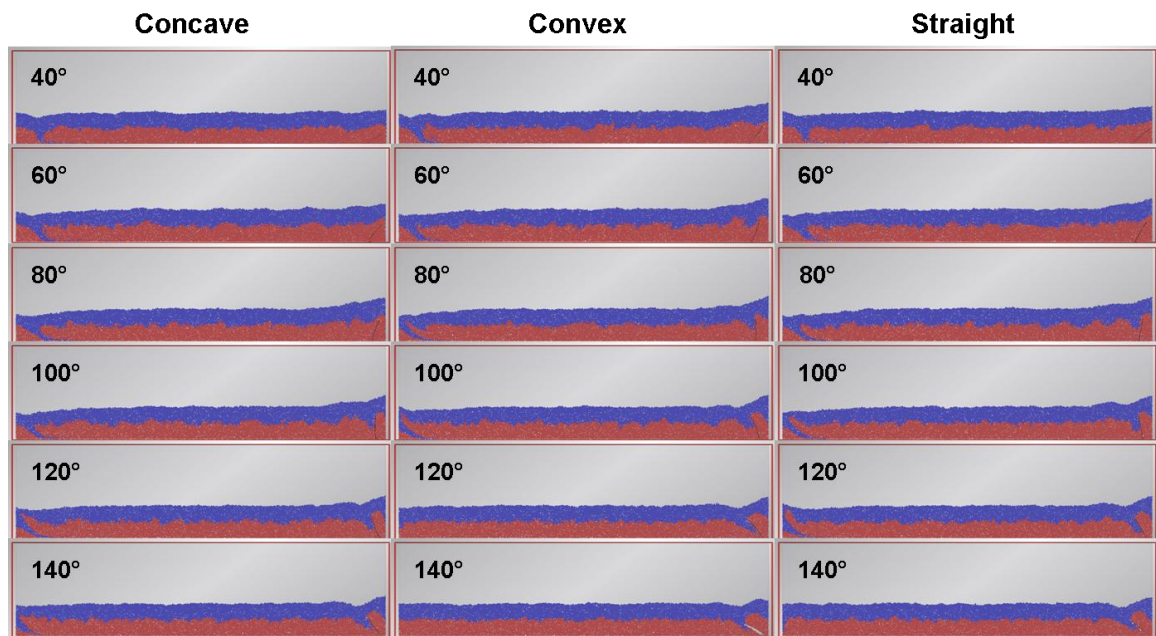
Figure 6.5. Final state for selected blade-rake angles and three blade shapes (concave, convex, and straight) for 2 mm particles.

For the strong acute angle of 40°, the total blade force for the larger particles (for all blade shapes) was almost 3-4 times higher than that for the smaller particles (compare the first and the second data rows of Table 6.4). The reason may be that the blade (as it moves to the right) forms a particle-trap for particles in front of the blade at the angle of 40°. The blade, the bottom surface and the walls of the box form a wedge-like region that traps the larger 10 mm particles (particle interlocking) more effectively than the smaller 2 mm ones. Similarly to the opening of hoppers, for which the opening size is recommended to be 3-4 times the largest particle size to avoid particle interlocking [29], the reason is likely to be particle-interlocking and bridge formation. Therefore, larger particles at strong acute angles near the bottom of the blade lead to a greater blade force at the bottom.

Six blade angles were used for 3-D studies, from 80° to 130° with 10° interval, but only three representative cases are shown in Figure 6.6. Again, the particle bed-height variation was slightly smaller for larger blade angles (see Figure 6.6), compared to smaller blade rake angles.

Figure 6.7 shows selected simulation cases for 10 mm and 2 mm particles without including the wall friction effects.
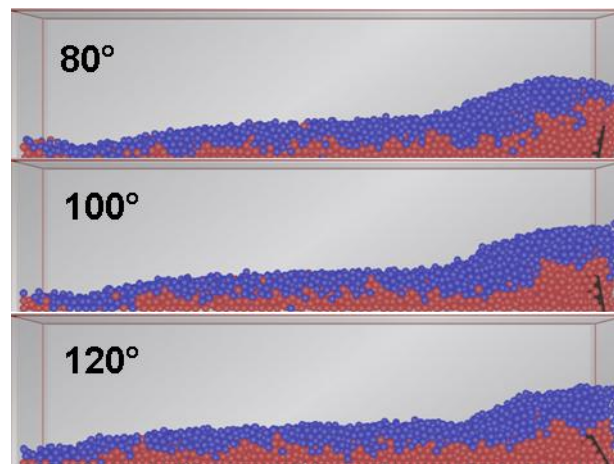
Figure 6.6. Final state of selected 3-D simulations with a straight blade shape.

In both cases (i.e., for the smaller and larger particles), it was observed that the whole particle bed was transported with the blade movement from left to right. However, in the case of larger particles, the particles accumulated at the right end of the box at the end of the simulation. For the smaller particles, the bed moved back (to the left) again and finally to the right to maintain its final position as shown in Fig. 6.7.

10 mm particles   **2 mm particles**
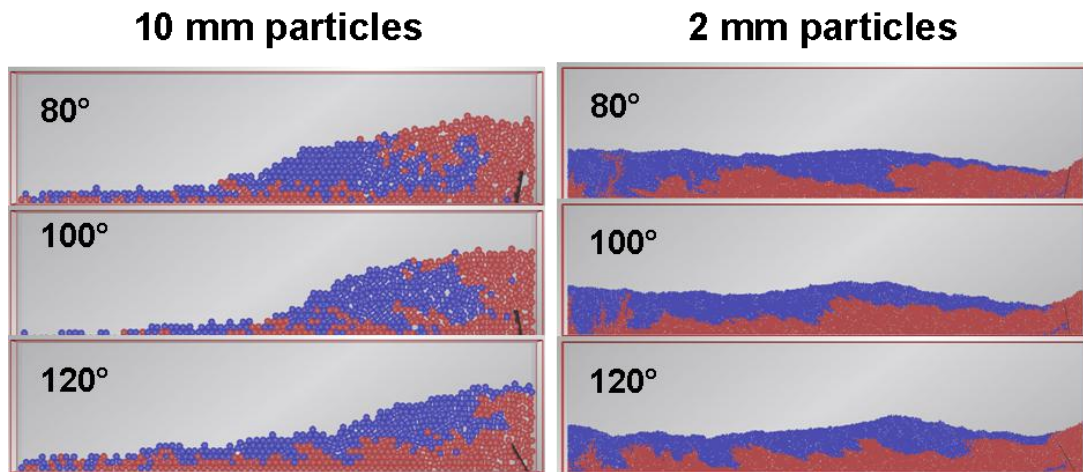
Figure 6.7. Final state for selected simulation cases for straight blade shape without wall friction.

The difference in behavior may be explained by the fact that for small particles the number of particle-wall interactions is significantly larger than for the larger particles. Furthermore, as shown below interparticle normal forces were increased for the case of 10mm particles (see Fig. 6.15a).

6.4.2 Velocity Profiles

Figure 6.8 shows particle positions and instantaneous velocities at the blade position of x≈0.5m, i.e., after the blade had moved a little more than half the distance along the x-direction for a) 10mm particles and b) 2mm particles. As can be seen the size of the voids or the "undisturbed region", as termed by Bagster et al. [28], is a function of blade shape, blade angle, blade speed and particle size. The voids were relatively small for larger particles and were significantly larger for the smaller particles (Figure 6.8b). This is because smaller particles have higher blade-relative velocities as they leave the blade (see Fig. 6.9) and since the trajectory of a moving object is strongly dependent on initial velocity and increases with the increase in initial velocity therefore smaller particles make larger voids behind the blade. In general, for low and intermediate angles, the size of the void is the smallest for the concave shape, and is larger in the case of convex and straight blade shapes. Apparently, the tip of the concave blade is more aligned with the flow, thus cutting through the particle bed. For low angles the opposite is true and the void region

is larger for concave blades, as in this case the concave shape poses more resistance to the flow (see Fig. 6.8a & 6.8b).
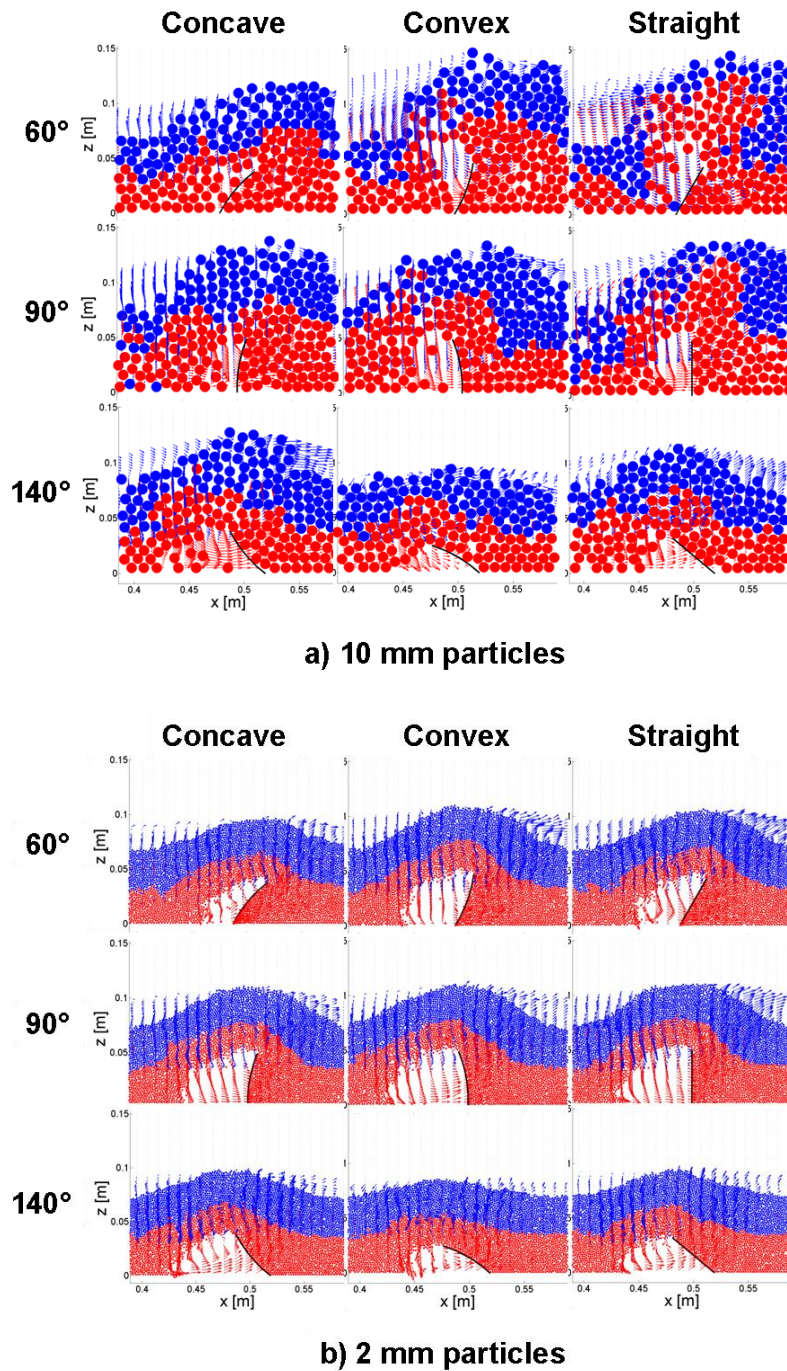
Figure 6.8. Particle instantaneous velocities for different blade shapes and selected blade-rake angles of 60°, 90° and 140° for: a) 10 mm particles, b) 2 mm particles. (vectors: projected direction of velocity).

_____

Figure 6.9 shows the blade-relative velocity profiles for all three blade shapes (i.e., concave, convex and straight) and selected blade-rake angles for: a) 10 mm particles and b) 2 mm particles including wall friction effects. In this reference system, the particle bed moves to the left. Blade-relative velocities were computed by comparing the instantaneous velocities of the particles with the blade velocity. The color of the field (blue to red) and length of the vectors represent the magnitude of blade-relative velocities in increasing order. The results are plotted for the blade position at x≈0.5 m, i.e., after the blade moved (slightly more than) half the distance in x-direction. As can be seen in the Figure, there are stagnant regions (blue) that move with the blade and regions where the blade moves through the powder (red).

a) 10 mm particles
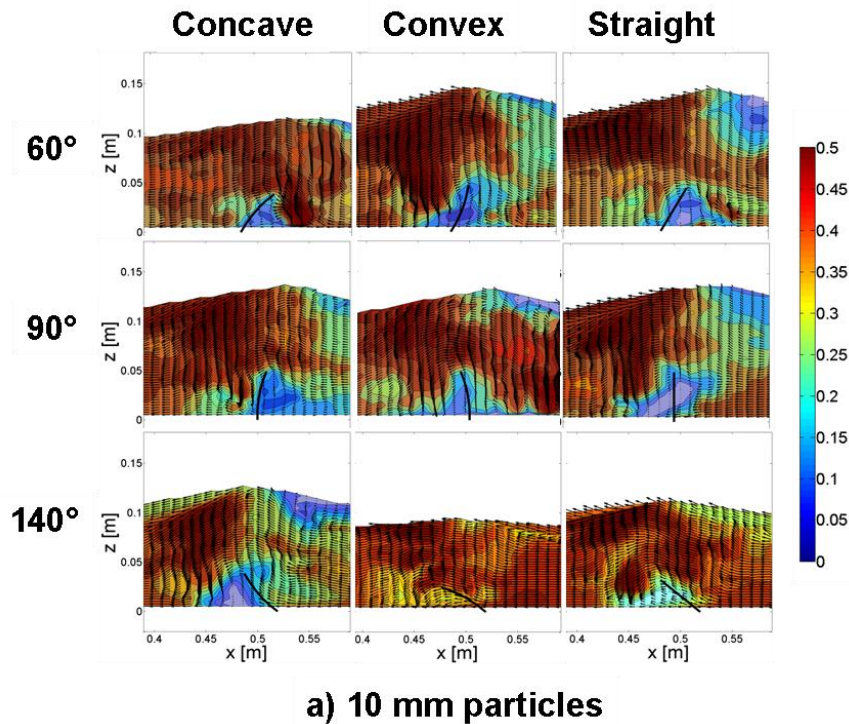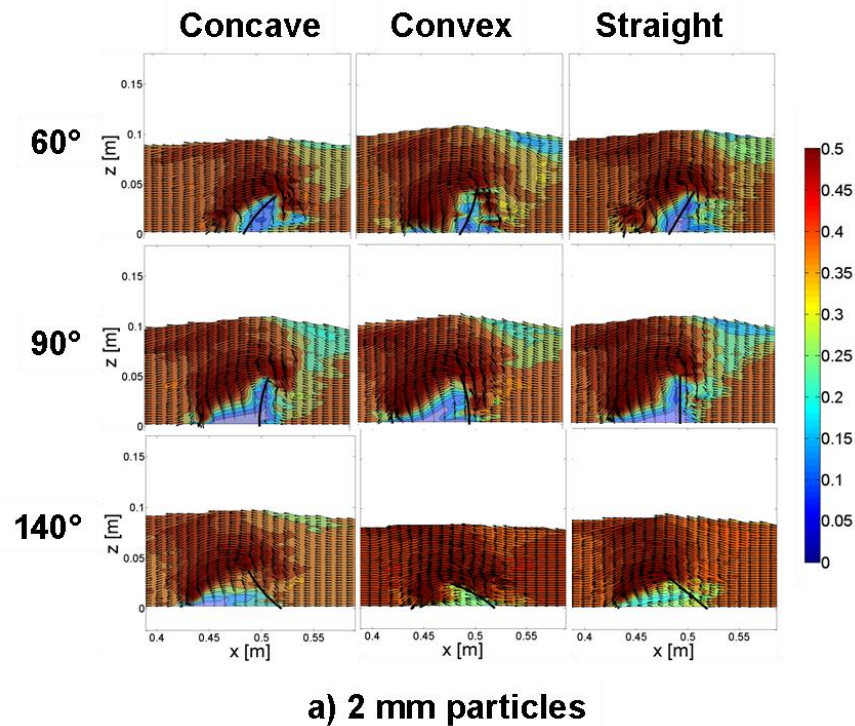
a) 2 mm particles

Figure 6.9. Blade-relative velocities for different blade shapes and selected blade-rake angles of 60º, 90º and 140º for: a) 10 mm particles, b) 2 mm particles. (Color code: magnitude of velocity; vectors: projected direction of velocity).

As can be seen from Figure 6.9a (10mm particles), the stagnant zone (i.e., its shape and location) is a strong function of angle and shape. For the smallest acute angle the stagnant zone is in front of the blade, as particles are pushed by the blade. As can be seen, the blade shape also has an impact, as for example for the convex shape a stagnant zone is formed also behind the blade. Also, convex and straight shapes lead to higher heaps that show a recirculation zone on top of the heap that is also shown as a blue zone. For an angle of 90° the zone is still in front of the blade, although for the convex shape particles tend to slide over the blade and the stagnant zone behind the blade is pronounced. For large obtuse angles, stagnant zones are behind the blade, although for convex shapes the blade tends to "slice through the bed".

For the small particles (Fig. 6.9b) the behavior is very similar to the case of large particles, i.e., stagnant zones and the recirculation have the same location with similar trends, although the recirculation zone on top of the bed is less pronounced. In addition, it is worth to note that the "approach velocity" of the particle bed (i.e., the velocity field

at the very right border) is a function of the blade angle. Here it can be seen that the velocity is reduced for all cases where the blade poses the largest resistance (see below for forces exerted on the powder bed). This depends both on the angle and the shape. For example, for large angles the concave shape poses the largest resistance, while for the small angles the opposite is true, i.e., convex shapes have a larger resistance.

6.4.3 Blade Force

Figure 6.10 shows the time-averaged blade-force on various sections of the concave blade as a function of blade angle for 10 mm particles. The time-averaged blade force values were calculated by taking the total blade force magnitude at all time-steps and then averaging these values from the time step t=0.5 s to t=1.7 s. If $\left|\vec{F}_b\right|$ is the total blade force magnitude and $\left|\vec{F}_b\right|'$ is the time-averaged total blade force magnitude then

$$\left|\vec{F}_b\right|' = \frac{\sum_{t=0.5}^{1.7}\left(\left|\vec{F}_b\right|_t\right)}{\Delta t}$$

where Δt= 1.2 s. The blade was divided into five equally-spaced parts; the first part at the bottom was numbered 1 and the top part was numbered 5 for all curved blade shapes and selected straight shapes. This classification is used in Figure 6.10 and Figure 6.13.

Figure 6.10 clearly indicates that the blade force for all top, middle and bottom sections decreases with blade-rake angle. At angles less than 90° very high blade forces were observed, especially at the bottom part of the blade because, as discussed in our previous study [19] and, as described above, an effective particle trap was formed at acute angles. At strong acute angles, e.g., 40°, this particle trap also led to significant particle interlocking for the larger 10 mm particles, as stated in previous sections.

Figure 6.10. Total blade force on different parts of the blade for 10 mm particles with respect to blade angle and blade shapes: a) concave, b) convex, c) straight.

These results reveal that most of the force transmitted to the powder bed stems from the bottom part of the blade. At angles larger than 100°, the blade forces were not

significantly different in various parts of the blade. Similar results were obtained for the convex and straight shaped blades, as shown in Figure 6.10b and 6.10c.
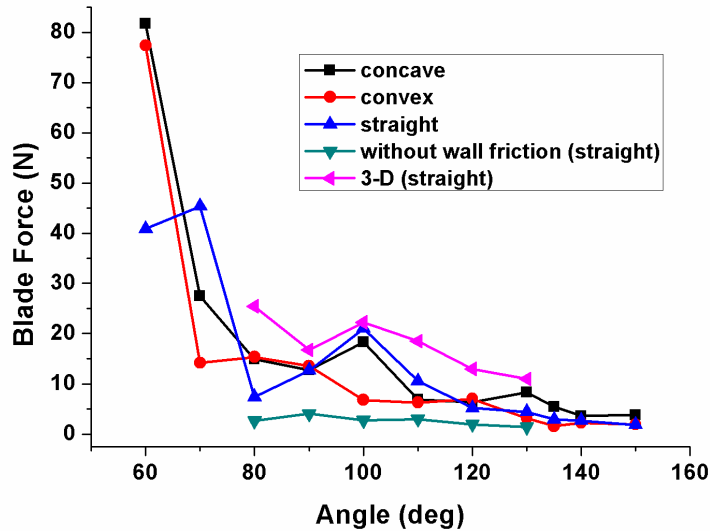
Figure 6.11. Time-averaged blade force variation on different type of blades with respect to blade angle, blade shape, wall friction, and 3-D case for dp = 10 mm.

Figure 6.11 shows the time-averaged blade-force (integrated over all sections of the blade) for all cases (i.e., concave, convex, and straight blade shapes) with 10 mm particles, including the 3-D and the no-wall-friction cases. The Figure illustrates that in all cases there was a significant increase in the blade force values when the blade angle values were below 90°. For the concave and straight blade shapes (both 2-D and 3-D) there was a small peak at the blade angle of 100°, and the blade force decreased with increasing blade angle. The blade force for 3-D cases was higher than for the corresponding 2-D cases for the same-size particles and at similar fill levels. The reason was that for 3-D cases (with the box depth of around five times greater than that for 2-D cases) the number of particles was almost five times higher (2720) than that for 2-D cases (600). However, wall friction occurred only for the same amount of particles than in the 2D case (i.e., the particles are the wall). As can be seen from the curve without wall friction, wall friction effects are significant.

As expected, without wall friction the blade forces were almost independent of angle and were lower than forces with wall friction.
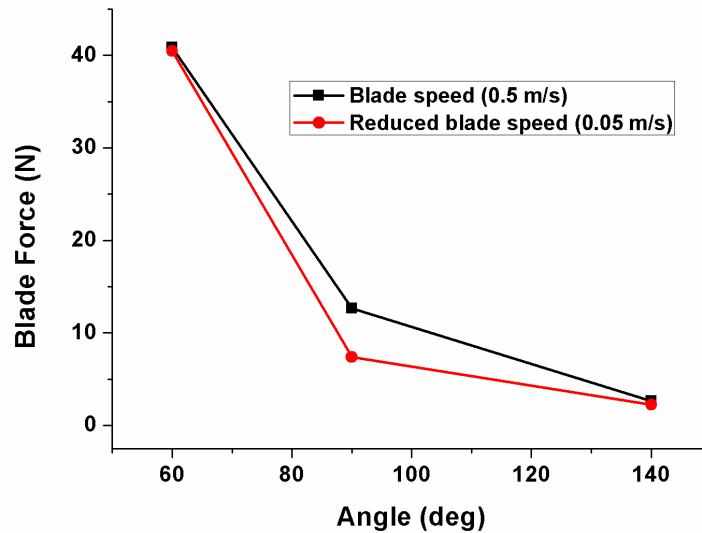
Figure 6.12. Effect of blade speed on time-averaged blade force variation with respect to blade angle for dp = 10 mm and involving straight blade shape.

Figure 6.12 shows the effect of the blade speed on the time-averaged blade force for 10 mm particles involving the straight blade shape with blade speeds of 0.5 m/s and 0.05 m/s. The Figure indicates that the average blade force values were slightly lower for the reduced blade speed cases, although the effect of the blade speed on the blade force was not significant, except for the case of 90°. Apparently, at a slower blade speed the particle bed offers slightly less resistance (as particles do not have to be accelerated as much, while frictional forces remain the same) to the flow for the same particle size and fill level.

Figure 6.13a shows the variation of the time-averaged blade-force on various sections of the concave-shaped blade with respect to the blade angle for 2 mm particles. The Figure displays almost same trend as for a similar case using 10 mm particles (Figure 6.10). The blade force was maximal in the bottom blade part and contributed the most to the total blade force, and again the lower angles showed much higher blade force due to the formation of particle trap at these angles as discussed earlier (Figure 6.10). The blade

_____

forces in the 2mm case were very high and significantly greater than those for the corresponding 10 mm particles due to larger number of particles resulting in higher interparticle forces as will be discussed later.
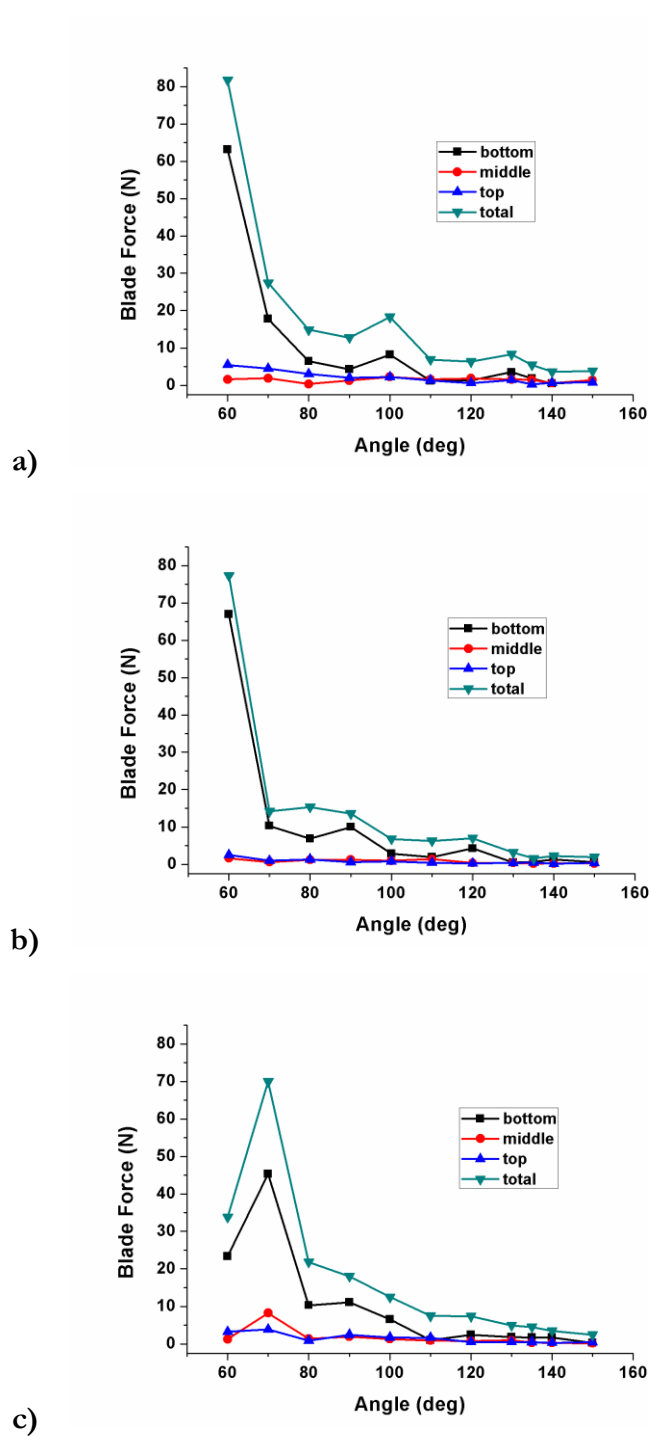

a)

b)

c)
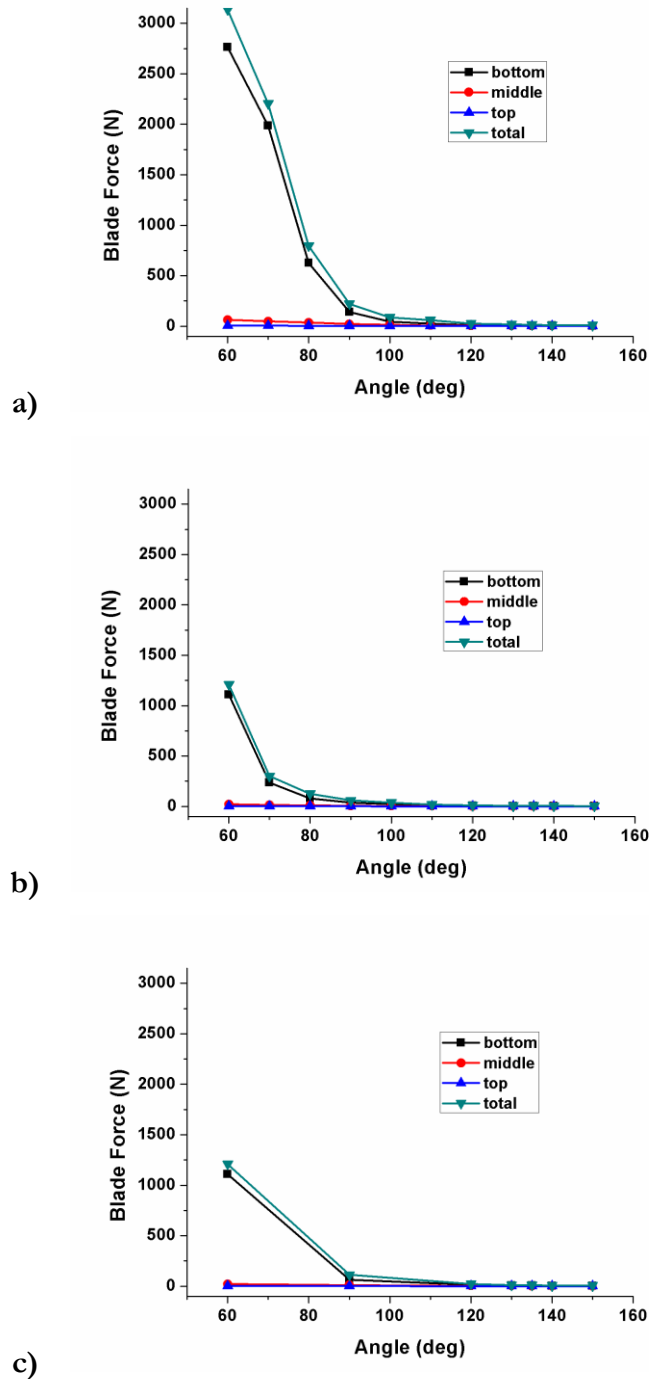
Figure 6.13. Total Blade force on different parts of blade for 2 mm particles with respect to blade angle and blade shapes: a) concave, b) convex, c) straight.

Figure 6.13b and 6.13c show the variation of the time-averaged blade-force in various sections of convex-shaped and straight blade for 2 mm particles. The blade force in these cases had a similar trend, yet did not increase as much due to less particle-trapping.

Finally, Figure 6.14 shows a variation of the time-averaged blade-force with respect to the blade's angle and shape and wall friction for 2 mm particles. It is clear that the blade force for all three shapes, i.e., concave, convex and straight, showed a sharp increase in the acute angle range. However, for the concave shape, as discussed earlier, the force was very high due to the particle-trapping effect, which is much more pronounced for the concave shape than for the straight shape, and which was least effective for the convex shape. In addition, for higher angles, the blade force for the concave shape was slightly greater than that for the straight or convex shapes. The least blade force was observed during simulations involving no wall friction effects because in the absence of wall friction for 2-D cases frictional forces were significantly reduced.
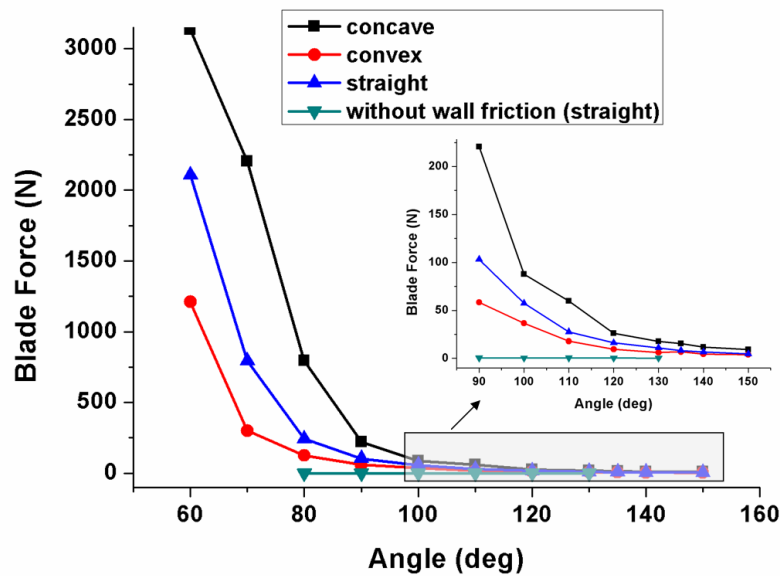
Figure 6.14. Variation of the time-averaged blade force with respect to blade angle, blade shape, and wall friction for dp = 2 mm.

In summary, if the blade force is denoted by F_b and the blade force for the cases without wall friction is denoted by $F_{b, wwf}$ then $F_{b, concave} > F_{b, straight} > F_{b, convex} > F_{b, wwf}$.

Thus, concave blades should exhibit the best mixing if the forces-transmitted translate into good mixing as shown in our previous papers. Furthermore, the blade force was much higher for the smaller particles than for the larger particles at the same fill levels (compare Figure 6.11 and Figure 6.14).

6.4.4 Interparticle Force

Figure 6.15 shows the time-averaged interparticle contact forces for a) normal and b) tangential forces as a function of blade angle and shape for 10 mm particles. The interparticle forces, both normal and tangential, were calculated by taking the sum of all interparticle forces, i.e., between red and red, red and blue, and blue and blue particles at all time-steps and then averaging these normal or tangential forces over time steps from t=0.5 s and t=1.7 s. In calculating the interparticle forces, only contact forces between particles were considered, i.e., contact forces of particles with the blade and walls were ignored.
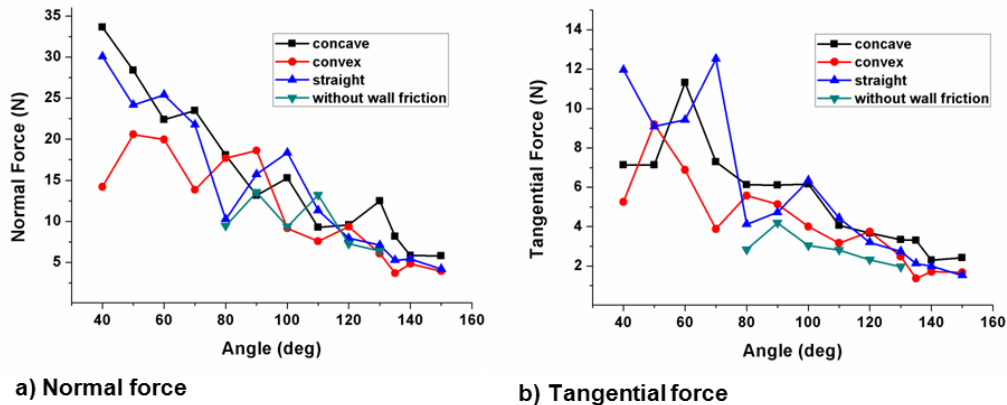
Figure 6.15. Time-averaged interparticle contact forces as a function of blade angle, blade shape for dp = 10 mm.

The Figure shows that the normal interparticle force was 3-4 times higher than the tangential force, which is with a result of the friction law. Both normal and tangential forces increased with the decrease in the blade-rake angle values. As expected, the interparticle normal and tangential forces were lower for the convex blade shape because the convex shape significantly reduces the particle trapping effect even at strongly acute

angles. The difference between normal contact force (Figure 6.15a) for the different blade shapes and for the cases involving no wall friction was not very clear, although the concave and straight shaped blade had a strong variability of forces with respect to the angle and were higher than the convex shape. Study of tangential forces also reveal similar trend (Figure 6.15b) but in this figure, the case with no wall friction showed lesser tangential contact forces compared to the corresponding straight blade shape with wall-friction.

Figure 6.16 shows a variation of the time-averaged interparticle contact force for the straight-shaped blades with respect to the blade angle, the blade speed, and 3-D cases using 10 mm particles. The cases with slower blade speeds (0.05 m/s) exhibited lower interparticle contact forces (normal and tangential) than the cases with the blade speed of 0.5 m/s. The 3-D cases showed higher interparticle normal and tangential forces compared to the 2-D cases with the same blade shape, particle size, fill-level and wall friction effects because, as discussed in the blade force section, that for the 3-D cases (with the box depth of around five times greater than that for 2-D cases) the number of particles is almost five times higher than that for 2-D cases. However, wall friction occurred only for the same amount of particles than in the 2D case (i.e., the particles are the wall).

a) Normal Force

b) Tangential Force
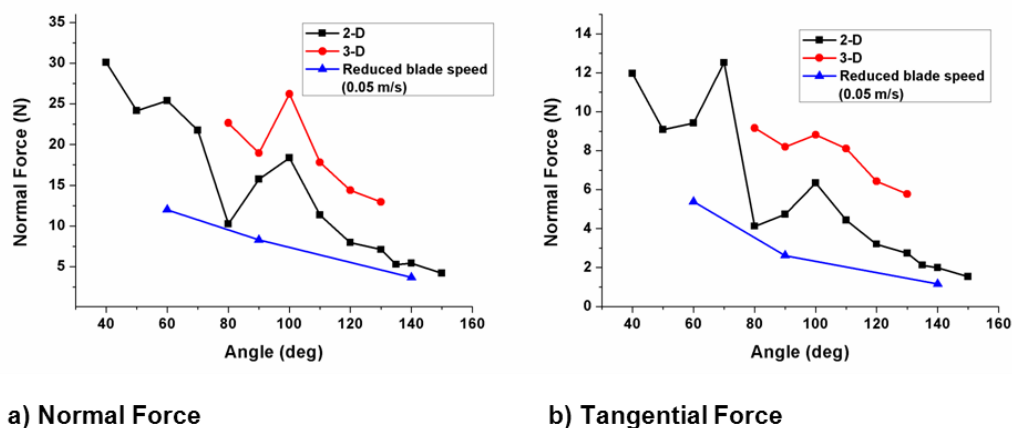
Figure 6.16. Time-averaged interparticle contact forces as a function of blade angle for $d_p = 10$ mm and for straight-shaped blades.

Figure 6.17 shows a variation of the time-averaged interparticle force with respect to the blade angle, the blade shape and wall friction for 2 mm particles. Compared to Figure 6.19, the curves are much smoother, as averaging is performed over much higher number of particles. Both normal and tangential forces, the former being approximately 3-4 times higher than the latter, increased sharply at around blade-rake angle values of 100° and less. The interparticle force values, as discussed above, were higher in the acute angle range because of the region formed in front of the blade where the particles coming were trapped and movement was restricted to only one direction, i.e., towards the right side of the box. Interparticle contact forces were the highest for the concave blade shape due to the curvature that offers strong resistance to the particle flow. The normal and tangential forces were the lowest for the convex blade shape because of the upward curvature of the blade, which allows an easy movement of the particles over the blade. The interparticle force values for the straight blade shape were in between those for the concave and convex shapes that offer a maximal and a minimal resistance, respectively. However, at large obtuse blade-rake angles, the difference in the interparticle force values was not significant for the three blade shapes investigated. The cases involving a straight blade shape without wall friction showed no significant difference in the interparticle force values with respect to blade angle until blade angle of 80°, since in the absence of wall friction the particles, although trapped, could still move easily in one direction, i.e., towards the right side of the box.

a) Normal Force   b) Tangential Force
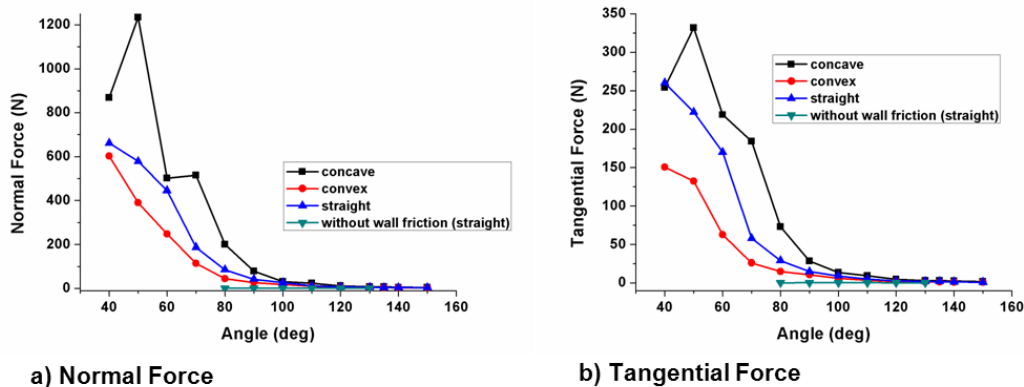
Figure 6.17. Time-averaged interparticle force variation with respect to blade angle, blade shape, and wall friction for dp = 2 mm.

In summary, convex blades result in the lowest resistance, thus minimizing torque and energy input, and thus costs. However, it is not clear, if mixing performance is a function of interparticle forces, i.e., if convex blades result in poor mixing. This is investigated in the next section.

6.4.5 Mixing Performance

Our previous study [19] showed that the maximal mean-instantaneous velocity (MMIV) of particles along the direction of the blade movement (x-direction) could be used as a good indicator of the mixing performance without involving complicated mixing indices. As previously reported [19], MMIV were calculated by first obtaining the mean values of the instantaneous velocities of all particles (along the x-direction) at each time step, i.e., between 0.4s to 1.9 s, and then calculating the maximum of these mean instantaneous velocities. Thus, the MMIV represents the highest mean instantaneous velocity (along the direction of the blade movement) attained in a simulation at any time-step.

Figure 6.18 shows MMIV variation with respect to the blade angle and shape and 3-D for 10 mm particles. The highest MMIVs were obtained for angles below 100°, which was consistent with our previous study [19]. At these blade angles the forces transmitted to the particle bed are high, thus causing improved shear and diffusive mixing, leading to an overall better mixing performance. For very small angles, the forces were very high. However, the flow did not lead to improved mixing, as in front of the blade pockets of particles are formed that do not mix with the rest of the particles.
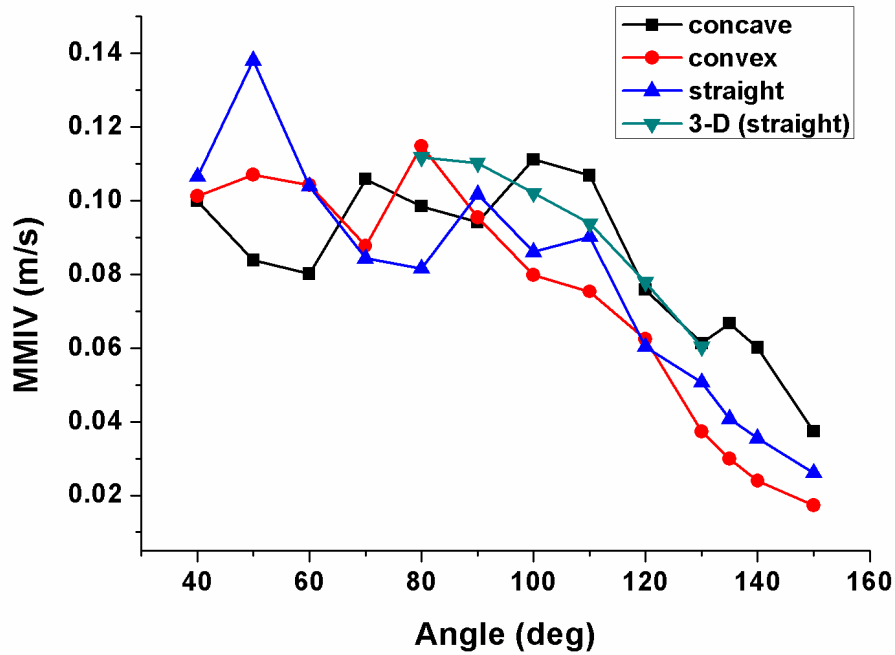
Figure 6.18. MMIV variation with respect to blade angle, blade shape and 3-D for d_p = 10 mm.

A difference between the three blade shapes, i.e., concave, convex and straight, was not clear from Figure 6.18 mainly because few particles (600) were used for the simulations, leading to poor statistics. Figure 6.19 shows MMIV variation with respect to the blade angle and shape for 2 mm particles. In the obtuse angle range and then up to around 70°, the concave shape had the highest MMIVs, followed by the straight and then the convex shapes. As discussed above, this is due to the concave curvature of the blade which disturbs the particle bed the most, and hence enhances mixing performance. The convex shape, on the other hand had the lowest MMIV values. For low angles, however, this trend reversed.
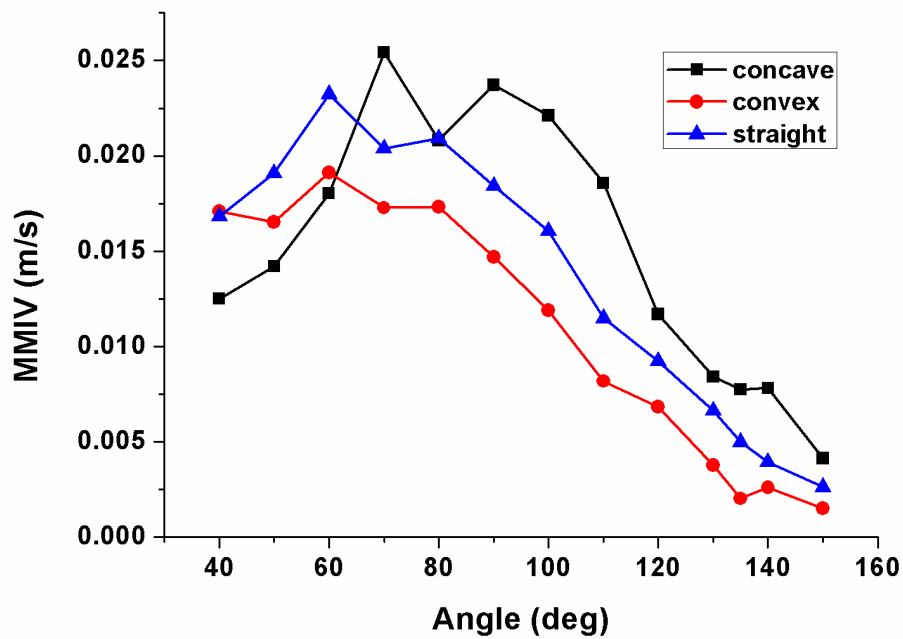
Figure 6.19. MMIV variation with respect to blade angle and blade shape, for $d_p = 10$ mm.

Finally, Figure 6.20 shows MGMMI variation with respect to the blade angle, the blade shape, 3-D and the blade speed for 10 mm particles. A value of MGMMI=1 indicates that a binary mixture is perfectly mixed, and the lower the MGMMI value is, the poorer is the mixing performance.
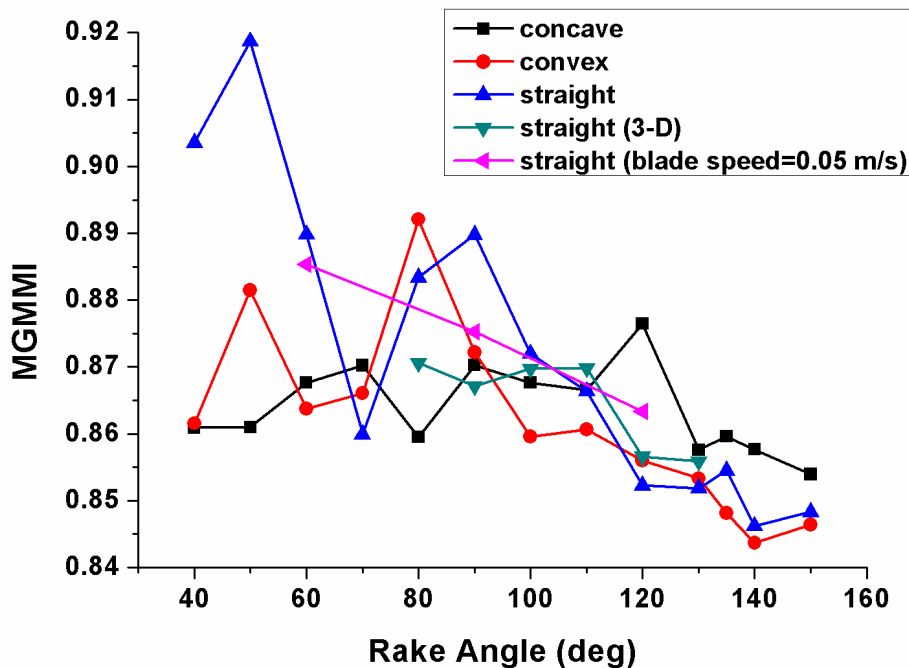
Figure 6.20. MGMMI variation with respect to blade angle, blade shape, 3-D, and blade speed for dp = 10 mm.

As can be seen in the Figure, the MGMMI decreases with angle for 10mm particles, although there is significant variability in the results due to the low number of particles. From the data it appears that for obtuse angles the highest mixing efficiency was obtained for concave shapes, while for acute angles the highest mixing index is observed for convex blades. This is explained by the fact that depending on the angle, different shapes give maximum exposure to the bed. The straight shape showed – on average - mixing index values between those for the concave and convex shapes. The effect of the blade speed, with a reduced blade speed of 0.05 m/s, was not evident and values were almost the same compared to the cases with a higher blade speed of 0.5 m/s.

Figure 6.21 shows MGMMI variation with respect to the blade angle and shape for 2 mm particles. The curves are smoother that in the case of 10mm particles, and interestingly, the mixing index increases with angle, albeit very little. Again the data show that for obtuse angles the highest mixing efficiency was obtained for concave shapes, while for acute angles the highest mixing index is observed for convex blades. Straight

blades are in between convex or convex blades. Nevertheless, from Figure 21 it can be concluded that blade shape has little effect on the mixing performance.
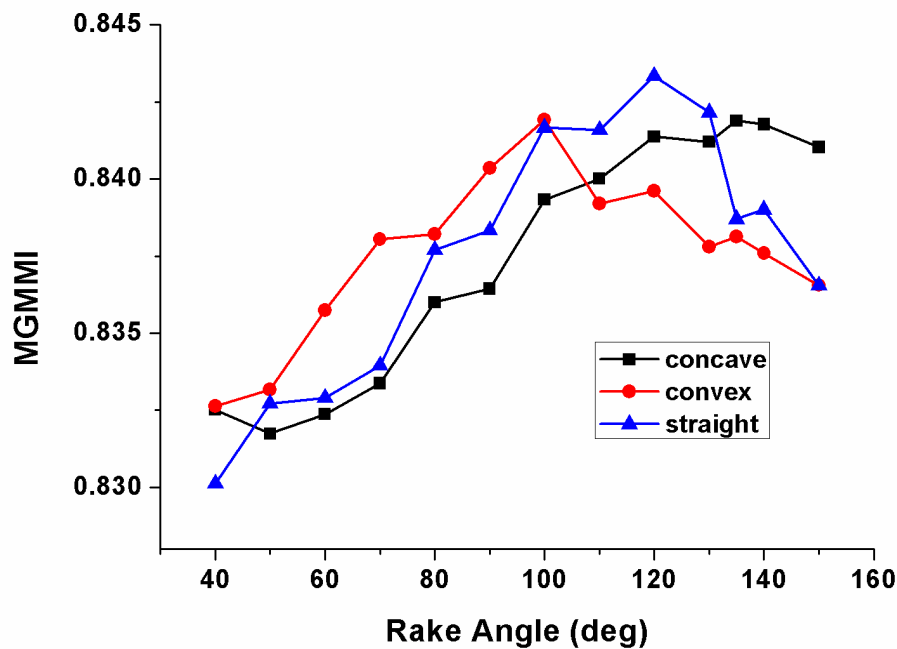
Figure 6.21. MGMMI variation with respect to blade angle and blade shape for $d_p = 10$ mm.

6.5 Conclusion

The objective of the study was to investigate the flow across a single blade using DEM simulations and to study the impact of blade shape and angle on the flow and mixing of 2mm and 10mm particles. The main results of our study are:

- The maximal blade force was observed for the concave blade shape, followed by the straight and then the convex shapes. Thus, convex blades result in energy minimization of an industrial mixer. The maximum of the forces were always exerted on the bottom part of the blade, thus providing information on the construction of industrial mixers (e.g., reinforcement and hardening of the bottom part).

___

- Average interparticle forces depend inversely on the blade-rake angle values. The interparticle forces were higher at lower angles, and especially at strongly acute angles. These forces were higher for the concave blade shapes followed by the straight and then the convex shapes. Thus, to prevent damage to the particles, shear and normal-force sensitive materials should be mixed in blenders with obtuse blade angles and convex or straight blade shapes.

- In past publications we could show that strong interparticle forces are required for effective granular mixing. Here, we could show that mixing efficiency depends on the blade angle: for acute angles convex blades give the best mixing performance, although concave blades impose the maximum forces on the bed. This is explained by the formation of pockets of particles that are compressed in the case of low angles and concave shape. Thus, for low angles, particle/blade forces and mixing do not correlate. For high angles, nevertheless, concave blades give the best mixing.

In summary, our study can assist in the understanding of the flow across single blades and how shape and angle impact the interparticle forces, blade forces and particle mixing, elucidating the effect of the blade shape and angle under diverse operating conditions. Future work will address an experimental confirmation of this study.

6.6 Nomenclature

abs	absolute (-)
C_n	normal damping coefficient (kg.s^{-1})
C_t	tangential damping coefficient (kg.s^{-1})
d_p	particle diameter (m)
E^*	reduced Young's modulus (-)
$\vec{F}$	force (N)
$\vec{F}_{cont,ij}$	contact force between particle i and j (N)
$\vec{F}_{drag,i}$	drag force on particle i (N)

$\vec{F}_{g,i}$	gravitational force on particle i (N)
$\vec{F}_{n}$	normal force (N)
$\vec{F}_{n-cont,ik}$	non-contact force on particle i by particle k (N)
$\vec{F}_{t}$	tangential force (N)
$\vec{F}_{total,i}$	total force on particle i (N)
I_{i}	moment of inertia (kg.m^2)
m	mass (kg)
m^{*}	reduced particle mass (-)
$\vec{M}_{ij}$	torque (Nm)
N	total number of particles of type $a+b$ (-)
n	n number of particles of type a (-)
$\hat{n}_{c}$	unit normal vector at contact point (-)
$\vec{R}$	vector of the mass center of the particle to contact plane (m)
R^{*}	reduced particle radius (-)
t	time (s)
$\vec{v}_{c}$	relative velocity of the two particles at their contact point (m.s^{-1})
$\vec{v}_{c}^{t}$	relative tangential displacement at contact (m)
wwf	without wall friction (-)
$\vec{x}$	position in x-direction (m)
x, y, z	position of a particle in x, y, or z direction (m)
$x_{ref}, y_{ref}, z_{ref}$	reference position in x, y, or z directions (m)

Greek Letters

a blade-rake angle (degree)

δ_n relative normal displacement at contact (m)

δ_{max} maximum relative tangential displacement when particle starts sliding (m)

μ friction coefficient (-)

ρ_p particle density (kg.m^{-3})

$\vec{\omega}_i$ angular velocity (s^{-1})

Subscripts

a, b type of particles

d   drag

g   gravitational

i particle i

j particle j

n number of type a particles

6.7 References

[1]   P.M.C. Lacey, Developments in the theory of particle mixing. Journal of Applied Chemistry 4 (1954) 257–268.

[2]   P.J. Cullen, Food Mixing: Principles and Applications. New York, Wiley-Blackwell (2009).

[3]   F.J. Muzzio, A. Alexander, C. Goodridge, E. Shen, T. Shinbrot. Solids Mixing Part A: Fundamentals of Solids Mixing. In: Edward L. Paul, Victor A. Atiemo-Obeng, Suzanne M. Kresta, ed. Handbook of Industrial Mixing: Science and Practice: John Wiley & Sons, Inc. (2004) 887–983.

[4]   R.L. Stewart, J. Bridgwater, D.J. Parker, Granular flow over a flat-bladed stirrer. Chemical Engineering Science 56 (2001) 4257-4271.

[5]   R.L. Stewart, J. Bridgwater, Y.C. Zhou, A.B. Yu, Simulated and measured flow of granules in a bladed mixer - a detailed comparison. Chemical Engineering Science 56 (2001) 5457-5471.

[6]   K. Malhotra, A.S. Mujumdar, H. Imakoma, M. Okazaki, Fundamental particle mixing studies in an agitated bed of granular materials in a cylindrical vessel. Powder Technology 55 (1988) 107-114.

[7]   K. Malhotra, A.S. Mujumdar, M. Okazaki, Particle flow patterns in a mechanically stirred two-dimensional cylindrical vessel. Powder Technology 60 (1990) 179-189.

[8]   K. Malhotra, A.S. Mujumdar, Particle mixing and solids flowability in granular beds stirred by paddle-type blades. Powder Technology 61 (1990) 155-164.

[9]   K. Malhotra, A.S. Mujumdar, M. Miyahara, Estimation of particle renewal rates along the wall in a mechanically stirred granular bed. Chemical Engineering and Processing 27 (1990) 121-130.

[10]   B.F.C. Laurent, J. Bridgwater, D.J. Parker, Motion in a particle bed agitated by a single blade. AIChE Journal 46 (2000) 1723-1734.

[11]   Y.C. Zhou, A.B. Yu, J. Bridgwater, Segregation of binary mixture of particles in a bladed mixer. Journal of Chemical Technology and Biotechnology 78 (2003) 187-193.

[12]   Y.C. Zhou, A.B. Yu, R.L. Stewart, J. Bridgwater, Microdynamic analysis of the particle flow in a cylindrical bladed mixer. Chemical Engineering Science 59 (2004) 1343-1364.

[13]   S.L. Conway, A. Lekhal, J.G. Khinast, B.J. Glasser, Granular flow and segregation in a four-bladed mixer. Chemical Engineering Science 60 (2005) 7091-7107.

[14]   B. Remy, J.G. Khinast, B.J. Glasser, Discrete element simulation of free flowing grains in a four-bladed mixer. AIChE Journal 55 (2009) 2035-2048.

[15]   B. Remy, J.G. Khinast, B.J. Glasser, The effect of mixer properties and fill level on granular flow in a bladed mixer. AIChE Journal 56 (2009) 336-353.

[16] B. Remy, T.M. Canty, J.G. Khinast, B.J. Glasser, Experiments and simulations of cohesionless particles with varying roughness in a bladed mixer. Chemical Engineering Science 65 (2010) 4557-4571.

[17] S. Radl, E. Kalvoda, B.J. Glasser, J.G. Khinast, Mixing characteristics of wet granular matter in a bladed mixer. Powder Technology 200 (2010) 171-189.

[18] G.R. Chandratilleke, A.B. Yu, R.L. Stewart, J. Bridgwater, Effects of blade-rake angle and gap on particle mixing in a cylindrical mixer. Powder Technology 193 (2009) 303-311.

[19] M.S. Siraj, S. Radl, B.J. Glasser, J.G. Khinast, Effect of Blade Angle and Particle Size on Powder Mixing Performance in a Rectangular Box. Powder Technology 211 (2011) 100-113.

[20] H.P. Zhu, Z.Y. Zhou, R.Y. Yang, A.B. Yu, Discrete particle simulation of particulate systems: Theoretical developments. Chemical Engineering Science 62 (2007) 3378-3396.

[21] P.A. Langston, U. Tüzün, D.M. Heyes, Continuous potential discrete particle simulations of stress and velocity fields in hoppers: transition from fluid to granular flow. Chemical Engineering Science 49 (1994) 1259-1275.

[22] P.A. Langston, U. Tüzün, D.M. Heyes, Discrete element simulation of granular flow in 2D and 3D hoppers: dependence of discharge rate and wall stress on particle interactions. Chemical Engineering Science 50 (1995) 967-987.

[23] P.A. Langston, U. Tüzün, D.M. Heyes, Discrete element simulation of internal stress and flow fields in funnel flow hoppers. Powder Technology 85 (1995) 153-169.

[24] Y.C. Zhou, B.D. Wright, R.Y. Yang, B.H. Xu, A.B. Yu, Rolling friction in the dynamic simulation of sandpile formation. Physica A 269 (1999) 536-553.

[25] H.P. Zhu, A.B. Yu, Averaging method of granular materials. Physical Review E 66 (2002) 1-10.

[26] B.N. Asmar, P.A. Langston, A.J. Matchett, A generalized mixing index in distinct element method simulation of vibrated particulate beds. Granular Matter 4 (2002) 129-138.

[27]   G.D.R. MiDi, On dense granular flow. The European Physical Journal E 14 (2004) 341-365.

[28]   D.F. Bagster, J. Bridgwater, The Flow of Granular Material Over A Moving Blade. Powder Technology 3 (1970) 323-338.

[29]   http://www.solidshandlingtech.com/ask_joe_articles/arching_part_one.htm; 2011. Online (12.07.2011).

[30]   Y.C. Zhou, B.H. Xu, A.B. Yu, Numerical investigation of the angle of repose of monosized spheres. Physical Review E 64 (2001) 021301.

7 Effect of Bed-height and Number of Blade Passes on Powder Mixing Performance

This study focuses on the effects of bed-height and number of blade passes on the powder mixing performance. Number of particles in this study were significantly higher as well as the length of the box than in the previous two chapters/studies [1-2].

The simulations were carried out in a two-dimensional setup using three fill-levels and up to 15 blade passes. Blade and interparticle forces were observed to have a direct relation with the fill-level while mixing performance had an inverse relation and decreased with the increase in fill-level.

Number of blade passes had different results on blade forces and normal and tangential interparticle forces. However, mixing performance increased almost exponentially in the beginning with the increase in number of blade passes and after around 12 blade passes, the change in mixing performance was not significant.

Keywords: Particle mixing, mixing index, MGMMI, blade force, interparticle force.

7.1 Introduction

Solid particle mixing is an important industrial phenomenon and crucial in chemical and pharmaceutical industry. In the latter case, it is critically important because the active pharmaceutical ingredient has to be mixed properly with the excipients due to strict drug regulatory laws. These industries mostly employ convective mixers for this purpose.

However, typical blenders can be divided in two types, i.e., tumbling and convective blenders. A tumbling blender consists of a closed vessel rotating about its axis. There are generally three types of tumbling blenders according to vessel geometries, i.e., the double cone, the V-blender, and the bin blender [3]. In convective blenders, mixing is achieved by rotating internals, such as blades, paddles or screws, in a static vessel [4]. The detail of industrial powder mixing can be found in the texts [3-4]. Continuous mixers include ribbon blenders, screw cone blenders etc. Batch mixers include e.g. vertical cylindrical mixers with two or four blades.

Lacey et al. [5] have defined three types of mixing mechanisms including convective, diffusive, and shear mixing. Convective mixing is due to the movement of large group of particles and the rate of mixing is high in this case. Diffusive mixing is due to the random motion of the solid particles and its rate is slow compared to convective mixing. Shear mixing is due to the development of slip-failure planes in the powder mixture e.g., when a chunk of powder slips down along this plane. Shear mixing can occur both in convective and high-shear mixers and also in tumbling mixers where a layer of powder avalanches down along a slope plane [4].

As discussed before, mixers can be classified as tumbling mixers and convective mixers. A tumbling mixer because of low shearing, however, may not be that effective against cohesive powders and powder materials that tend to segregate.

Among these two types of mixers, convective mixers have been investigated in detail using both experimental and simulation techniques [6-20] as compared to tumbling batch mixers. Several publications have reported the results using a convective batch mixer with two [6,7,13,14,20] and some using four [15-19] blades. Some of these publications employed only experimental techniques [6,15] while some used simulations

[13,14,16,17,19,20] only. Some publications compared the results using both simulation and experimental techniques [8,18].

Stewart et al. [6] investigated granular flow over two opposite flat blades using positron emission particle tracking. They observed three-dimensional recirculation zones and found a linear dependence of particle speed on the speed of blade. They also observed that the size of the recirculation zones and the number of blade passes that the particles spend in these zones decreased with the increase in fill level and blade speed. They compared their experimental results with the simulation results in another paper [7]. Some publications have also reported experimental studies for two-dimensional flow over a flat blade in a cylindrical vessel [8] and in some publications using paddle type blades [9-11]. Photographs were taken and videos were made in order to monitor the movement of the particles. They observed a difference in flow in the main bed and the flow at the end wall. Laurent et al. [12] also used a single blade to observe the motion in a particle bed but using positron emission particle tracking. Zhou et al. [14] investigated the effects of sliding and rolling friction coefficients on the promotion of three-dimensional recirculating particle zones. Conway et al. [15] used particle image velocimetry (PIV) technique to study the velocity fields near the top and the wall for near-monodisperse and polydisperse granular materials. They observed three-dimensional recirculating zones and studied mixing and segregation with respect to shear rates. Remy et al. [16] investigated the effect of blade orientation on particle flow patterns and mixing kinetics using DEM simulations in addition to the effects of friction coefficients on mixing. They also studied normal and shear stresses and their dependence on mixer height and friction coefficients of particles. In another study, Remy et al. [17] investigated the effects of fill level and other mixer properties e.g. vertical blade position from bottom, wall friction, mixer diameter, and blade speed on granular flow characteristics and on mixing. Remy et al. [18] also investigated the effects of varying roughness and the effects of varying blade speed on granular flow of cohesionless particles using simulations and experimentally. Radl et al. [19] investigated the mixing characteristics of wet granular matter and observed better mixing rates and performance as compared to dry granular matter under certain conditions [19].

In a recent paper by Chandratilleke et al. [20], blade-rake angle for a cylindrical mixer was investigated using four blades for three blade-rake angles, i.e., 45°, 90°, and 135°. The mixing performance in this work was quantified using Lacey's mixing index. They reported 90° as the angle showing the highest mixing rate. In a recent study, Siraj et al. [1] investigated the effects of blade-rake angle and particle size ratio ($d_{p,top}/d_{p,bot}$) of polydisperse particles on powder mixing performance in a rectangular box. They quantified the mixing performance by using the Modified Generalized Mean Mixing Index (MGMMI). They also studied the velocity profiles for different blade angles and particle size ratios. In addition, the variation of interparticle force and blade force with the change in the blade-rake angle and particle size ratios was also studied.

The goal of this work is to study the particle flow across a single blade and its impact on blade force and interparticle forces as well as mixing as a function of bed-height and number of blade passes. With this objective in mind, we studied the mixing performance variation with bed-height and number of blade passes. DEM simulations were carried out in order to simulate the flow across a single blade.

7.2 Numerical Method

The distinct/discrete element method or DEM is a powerful tool for the simulations of granular flows and gives a detailed picture of the flow by keeping track of each individual particle discretely.

DEM method is based on force and momentum balance for all particles but every particle is treated discretely and is solved for all the forces acting on it. These forces include contact forces, body forces, hydrodynamic forces and non-contact or cohesive forces. These forces are then integrated over time to get position and velocity of each individual particle.

Newton's second law of motion can be translated into force balance equation for a particle i in the following way:

$$m_i \frac{d^2 \vec{x}_i}{dt^2} = \vec{F}_{total,i} = \sum_j \vec{F}_{cont,ij} + \sum_k \vec{F}_{n-cont,ik} + \vec{F}_{g,i} + \vec{F}_{drag,i} \qquad (7.1)$$

Here, m_i is the mass of the particle i and $\vec{x_i}$ is the position of the particle. Integration of this equation gives velocity, and double integration gives the position of the particle i. $\vec{F}_{total,i}$ is the sum of all forces acting on the particle i whereas $\sum_j \vec{F}_{cont,ij}$ is the sum of all contact forces between particle i and j. $\sum_k \vec{F}_{n-cont,ik}$ is the sum of all non-contact or cohesive forces between particle i and k. $\vec{F}_{drag,i}$ is the drag force exerted by the surrounding fluid. In granular flows, however, fluid-particle interactions are negligible compared to contact and other forces. Therefore, drag force or $\vec{F}_{drag,i}$ can be ignored. $\vec{F}_{g,i}$ is the gravitational force exerted on the particle i.

The momentum balance is

$$I_i \frac{d\vec{\omega_i}}{dt} = \sum_j \vec{M}_{ij} \tag{7.2}$$

In Eq. 7.2, I_i is the moment of inertia, ω_i is the angular velocity, and $\vec{M}_{ij}$ is the torque acting on particle i by particle j.

Different models and numerical schemes are available to solve these equations for translational and rotational motion of each particle. The first term on the right hand side of Eq. 7.1, i.e., $\sum_j \vec{F}_{cont,ij}$, is the most critical part comprising normal and tangential force components.

Simplified Hertz-Mindlin and Deresiewicz model [21-26] was used for our simulations.

- Normal force

$$\vec{F}_n = -\frac{4}{3} E^* \sqrt{R^*} (\delta_n)^{3/2} - C_n (8m^* E^* \sqrt{R^* \delta_n})^{1/2} . (\vec{v_c}.\hat{n_c})\hat{n_c} \tag{7.3}$$

- Tangential force

$$\vec{F}_t = -\mu | \vec{F}_{n,e} | (1 - (1 - | \vec{v_c^t} | / \delta_{max})^{3/2})\hat{v_c^t}$$
$$+ 2C_t (1.5 \mu m^* | \vec{F}_{n,e} | . \sqrt{1 - | \vec{v_c^t} | / \delta_{max}} / \delta_{max})^{1/2} . (\vec{v_c} \times \hat{n_c}) \times \hat{n_c} \tag{7.4}$$

The following basic steps are involved in almost all DEM simulations [19];

1. Collision detection through particle-particle and particle-wall contacts/overlaps.

2. Application and calculation of contact forces to all collisions.

3. Calculation of other forces, body (gravitational) and hydrodynamic (fluid drag) for all particles (fluid drag was neglected in this work).

4. Determination of unknowns in equations 7.1 & 7.2 to calculate particles' translational and rotational accelerations.

5. Numerical integration of the acceleration to find particles' new positions and velocities.

The simulations were performed using EDEM developed by DEM Solutions and the model used was Hertz-Mindlin as mentioned above.

The mixing performance was quantified using a modified GMMI, i.e., MGMMI [1].

$$MGMMI = 1 - \frac{abs(1 - GMMIx_a) + abs(1 - GMMIy_a) + abs(1 - GMMIz_a)}{3} \tag{7.5}$$

For two types of particles a and b, the generalized mean mixing index of a type particles, i.e., $GMMI_a$ is calculated by the sum of mean positions of n number of a type particles divided by the sum of mean positions of all N number of $a+b$ type of particles. $GMMI_a$ is calculated in x, y, or z directions depending upon whether positions x, y or z are used in Eq. 7.5.

where

$$GMMIx_a = \frac{\left[\sum\limits_{p=1}^{n} \frac{(x_p - x_{ref})}{n}\right]}{\left[\sum\limits_{q=1}^{N} \frac{(x_q - x_{ref})}{N}\right]} \quad GMMIy_a = \frac{\left[\sum\limits_{p=1}^{n} \frac{(y_p - y_{ref})}{n}\right]}{\left[\sum\limits_{q=1}^{N} \frac{(y_q - y_{ref})}{N}\right]} \quad GMMIz_a = \frac{\left[\sum\limits_{p=1}^{n} \frac{(z_p - z_{ref})}{n}\right]}{\left[\sum\limits_{q=1}^{N} \frac{(z_q - z_{ref})}{N}\right]}$$

x_{ref}, y_{ref}, and z_{ref} are the reference positions in x, y and z directions and were zero in our box case. GMMI was originally introduced by Asmar et al. [27] and was later modified, used and explained in a study by Siraj et al. [1].

7.3 Simulation Setup

Parameters and their determination are important in a simulation as they serve the input in the form of the coefficients of modeling equations. Detail of the parameters used in our simulations is given in Table 7.1.

Table 7.1. Parameters used for simulations.

Parameter	Value	Units
Box dimensions (length × width × height)	1.2 × 0.048 × 0.395	m
Blade dimensions (width × height)	0.032 × 0.032	m
Blade clearance from bottom	0.01	m
Blade rake angle	90	deg
Blade speed	0.15	m/s
Material (Particle /Blade/Container)	Glass/Steel/Steel	-
Particle Diameter (d_p)	4	mm
Fill levels (bed heights)	30, 42(~blade height), and 59	mm
Number of particles	32490 (30 mm bed height, half red half white) 45480 (42 mm bed height, half red half white) 63890 (59 mm bed height, half red half white)	-
No. of blade passages	Single passage for 30 and 59 mm bed height 1,2,3…,20 blade passages for 42 mm bed height (~blade height)	-
Particle Density, glass (ρ_p)	2456	kg/m³
Poisson Ratio	0.25	-
Shear Modulus	2.2×10^8	Pa
Coefficient of Restitution	0.3 (for glass-steel) and 0.5 (for glass-glass)	-

Parameter	Value	Units
Coefficient of Static Friction	0.5	-
Coefficient of Rolling Friction	0.01	-

Figure 7.1 shows the box geometry. A rectangular box was used with dimensions as shown in the figure. The blade rake angle used was 90° whereas three fill levels were used for the study. First fill-level was 30 mm (below the height of the blade), second fill-level was 42 mm (blade height) and third fill-level was 59 mm (above blade height).
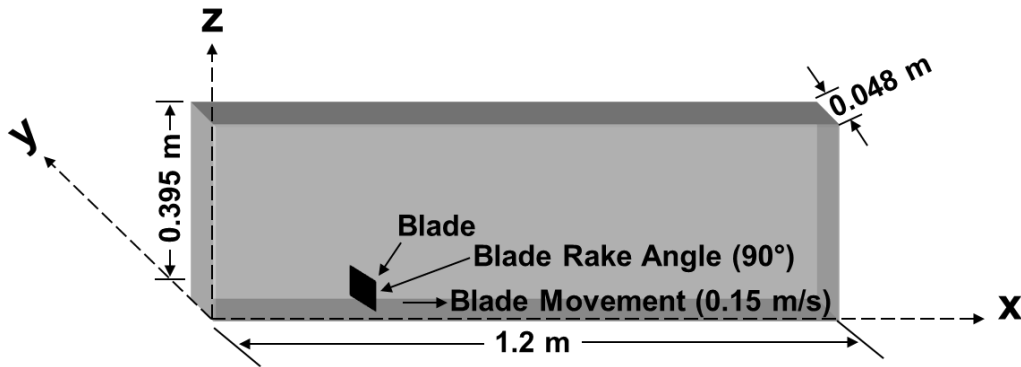
Figure 7.1. Geometry of the box used for simulations.

Each case comprised of mono-sized particles of 4 mm diameter. The length, width and the height of the box was same in all simulations. The number of particles used, were 32490, 45480 and 63890 for all three fill-levels in the increasing bed-height respectively.

As discussed by Siraj el al. [1] and Remy et al. [17], that in the quasi-static regime, the blade speed does not have significant impact on mixing. The dimensionless shear rate is one of the most important parameters to be known that determine the granular flow regime [28]:

$$I = \frac{\dot{\gamma} \cdot d_p}{\sqrt{P/\rho}} \tag{7.6}$$

Where $\dot{\gamma}$ is the shear rate, d_p is the particle diameter, P is characteristic normal stress (i.e., the particle pressure) and ρ is the bulk density. The dimensionless parameter I describes

_____

the relative importance of inertia to the normal stress in the particle bed. For vertical free surface flows, the characteristic normal stress can be approximated [28] by:

$$P = \rho \cdot g \cdot h \qquad (7.7)$$

and the shear rate can be approximated [28] with:

$$\dot{\gamma} = V/h \qquad (7.8)$$

Here, h and V are characteristic bed height and bed velocity respectively. Inserting these approximations into the definition of the dimensionless shear rate yields:

$$I = \frac{V \cdot d_p}{\sqrt{g \cdot h^3}} \qquad (7.9)$$

If the parameter I is above 10^{-2}, the quasi-static regime (where the effective friction coefficient is constant) is no longer valid, and the transition to the dense inertial regime has been reached [28].

Table 7.2. Fr and I values for different simulation setups.

Simulation type	Dimensionless Shear Rate, $I = \dfrac{V \cdot d_p}{\sqrt{g \cdot h^3}}$	Froude Number, $Fr = V/\sqrt{g.h}$
d_p = 4 mm, V = 0.15 m/s, h = 30 mm	0.277	0.037
d_p = 4 mm, V = 0.15 m/s, h = 42 mm	0.234	0.022
d_p = 4 mm, V = 0.15 m/s, h = 59 mm	0.197	0.013

As summarized in Table 7.2, dimensionless shear rate I in our case was 0.277 for bed-height of 30 mm, 0.234 for bed-height of 42 mm and 0.197 for bed-height of 59 mm.

Thus, the process is not in the quasi-static regime for all cases having blade speed of 0.15 m/s and 4 mm diameter particles. As can be seen from Table 7.2, both dimensionless shear rate (*I*) and Froude number (*Fr*) show an inverse relation with the bed-height and decrease with the increase in bed-height.

_____

Tardos et al. [29] has published a regime map for granular flows as a function of a dimensionless parameter defined by:

$$\dot{\gamma}^* = \dot{\gamma}\sqrt{\frac{d_p}{g}} \qquad\qquad (7.10a)$$

Alternatively, using Eq. 7.8 to replace value of $\dot{\gamma}$

$$\dot{\gamma}^* = \frac{V}{h}\sqrt{\frac{d_p}{g}} \qquad\qquad (7.10b)$$

As shown evident from Figure 7.2, this map separates the quasi-static regime from 'intermediate' regime which corresponds to the dense inertial regime defined by Midi GDR et al. [28] and is discussed above.
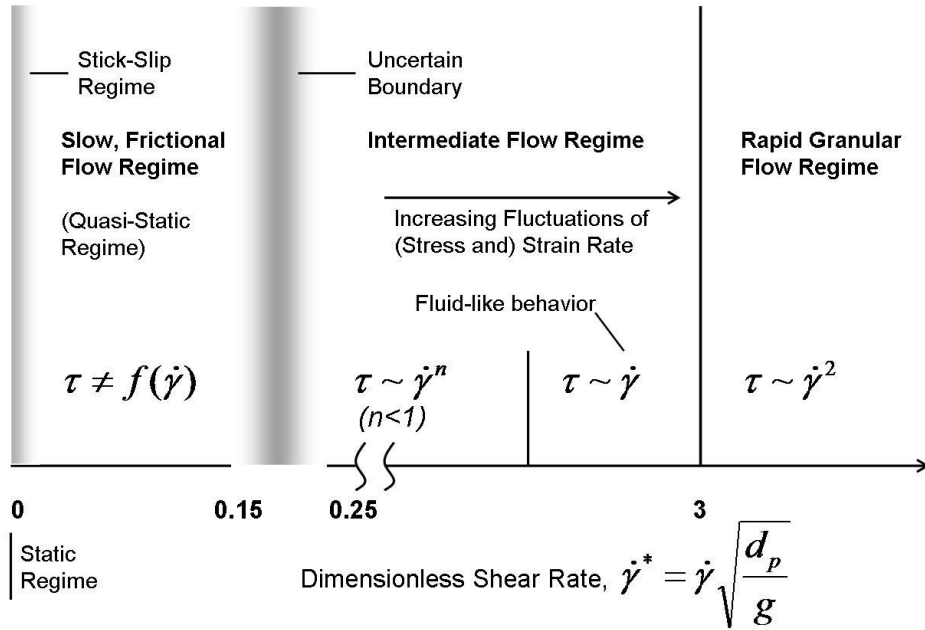

Figure 7.2. Regime map of granular flow (Reproduced from Tardos et al. [29]).

As can be seen from Table 7.2, the dimensionless shear rate in Eq. 7.9 depends strongly on the bed height.

Another important dimensionless quantity in granular flows is Froude number (*Fr*). It is defined as the ratio of inertial forces to gravitational forces, i.e., $Fr = V / \sqrt{g.h}$.

Here, V again is the particle bed velocity (which, in turn, is equal to blade velocity), h is the particle bed height, and g is the acceleration due to gravity. As can be seen from above equation, the Froude number (Fr) is not influenced by the particle size unlike the dimensionless shear rate.

Figure 7.3 shows initial state of three simulation cases (from a to c) with increasing particle bed-height respectively.

a) Initial state, fill-level 30 mm (32490 particles).

b) Initial state, fill-level 42 mm (45480 particles).

c) Initial state, fill-level 59 mm (63890 particles).
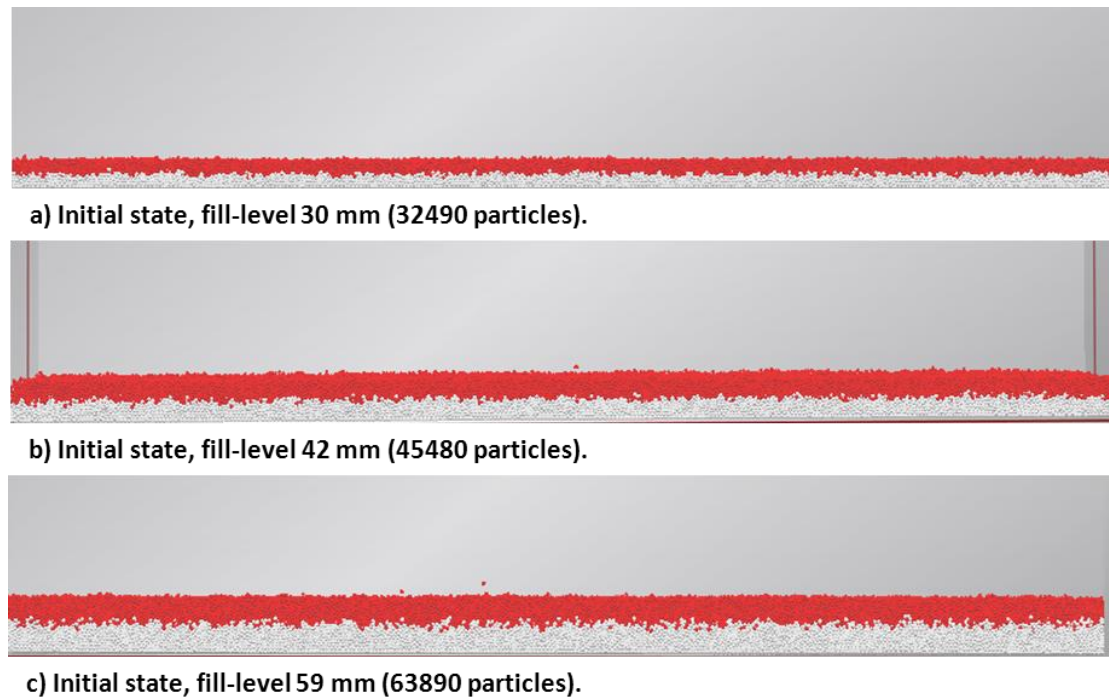
Figure 7.3. Initial state of simulation cases for three fill levels.

In all cases, white particles were put first at the bottom of the box while red particles were put on the top later. Diameter was 4 mm for all particles. In the first case, 32490 particles were used whereas 45480 particles were used for the second case and 63890 for the last case. As observed in the earlier study [1], the interface between white and red particles is only approximately planar.

7.4 Results and Discussion

First, the snapshots of the simulation cases after single and multiple blade passes will be discussed for varying fill-levels or bed-heights.

_____

Figure 7.4 shows the effect of a single blade pass as it moves from left to right of the box. It shows final state of the simulation cases for three fill-levels after single blade pass. The visual inspection shows that the bed-height variation holds an inverse relation with the fill-level and is maximum for the least bed-height and minimum for maximum bed-height.

a) Final state, fill-level 30 mm (32490 particles) after single blade pass.

b) Final state, fill-level 42 mm (45480 particles) after single blade pass.

c) Final state, fill-level 59 mm (63890 particles) after single blade pass.

Figure 7.4. Final state of simulation cases for three fill levels after single blade pass.

Figure 7.5 shows snapshots for a fixed bed-height or fill-level (equal to blade height) against varying blade passes. The first blade pass is complete when the blade moves from left to right of the box while second blade pass is from right to left of the box.
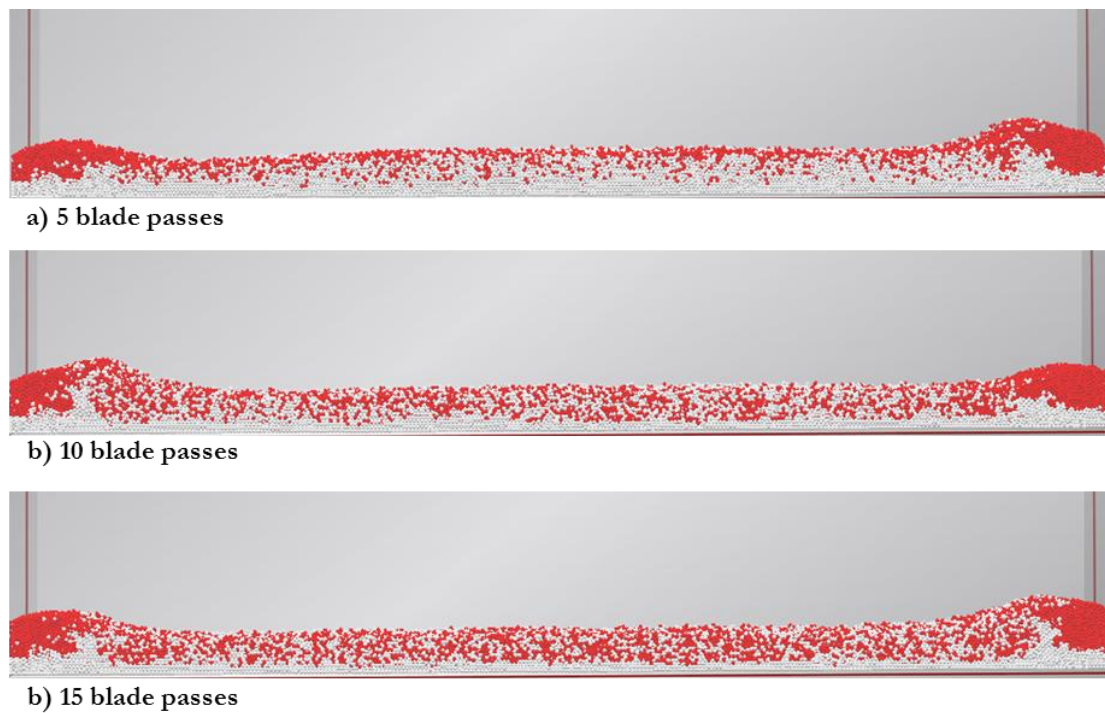
Figure 7.5. Final state of simulation cases after 5, 10 and 15 blade passes for fill-level of blade height (42 mm).

Thus all odd-numbered blade passes represent forward motion of the blade, i.e., from left to right of the box whereas all even-numbered blade passes represent backward motion of the blade, i.e., from right to left of the box. As can be seen from Fig. 7.5, the mixing performance increase with the increase of number of blade passes as expected. Particles accumulated at both ends of the box indicate the terminal wall-effects and the fact that a certain gap was maintained at both ends to avoid higher stress development due to trapping of particles at these ends as explained in a recent study by Siraj et al. [1]. An undisturbed layer at the bottom of the box is due to the blade clearance of 0.01 m (or 10 mm) in all cases unlike previous studies by the author with no blade clearance [1,2]. This clearance of 10 mm is equal to 2.5 times the particle diameter.

Figure 7.6 shows the blade force variation with particle fill-levels or bed-heights. The time-averaged blade force values were calculated like in previous studies [1,2], i.e., by taking the total blade force magnitude at all time-steps and then averaging these values from the time step t=0.6 s to t=6.0 s in case of first blade pass.

As can be expected, the blade force increases with the increase of particle fill-level or increase in bed-height. The blade force increases with the increase of bed-height keeping all other conditions like blade rake angle, blade shape etc. constant unlike our previous studies [1,2] where different blade shape and angles were used.
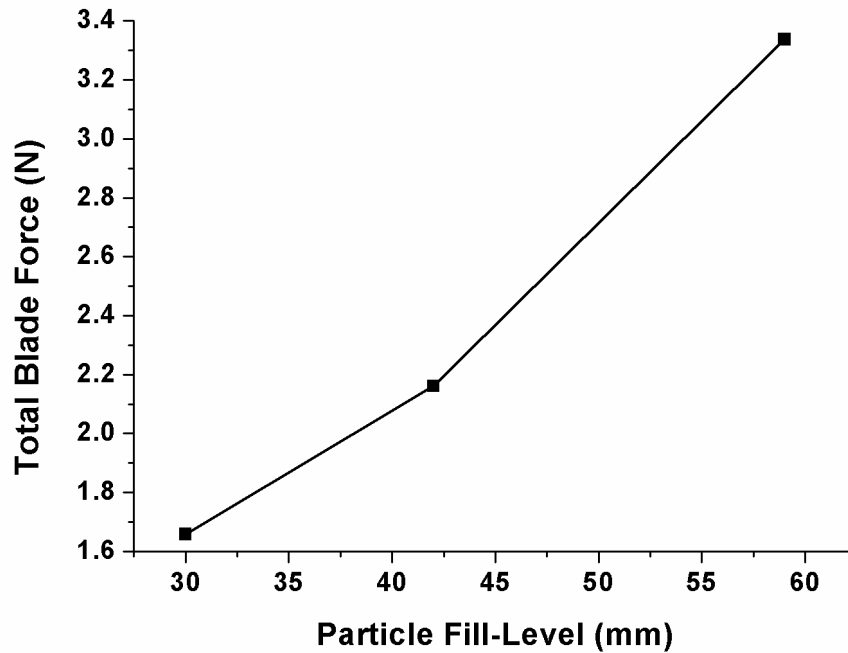
Figure 7.6. Blade force variation with particle fill level.

Figure 7.7 shows blade force variation with the number of blade passes for a fixed bed-height of 42 mm. The figure shows an interesting oscillating trend of blade force variation with the number of blade passes. Each subsequent oscillating peak in the blade force variation curve shows a dampening effect in the amplitude than the preceding peak with the increase in number of blade passes.
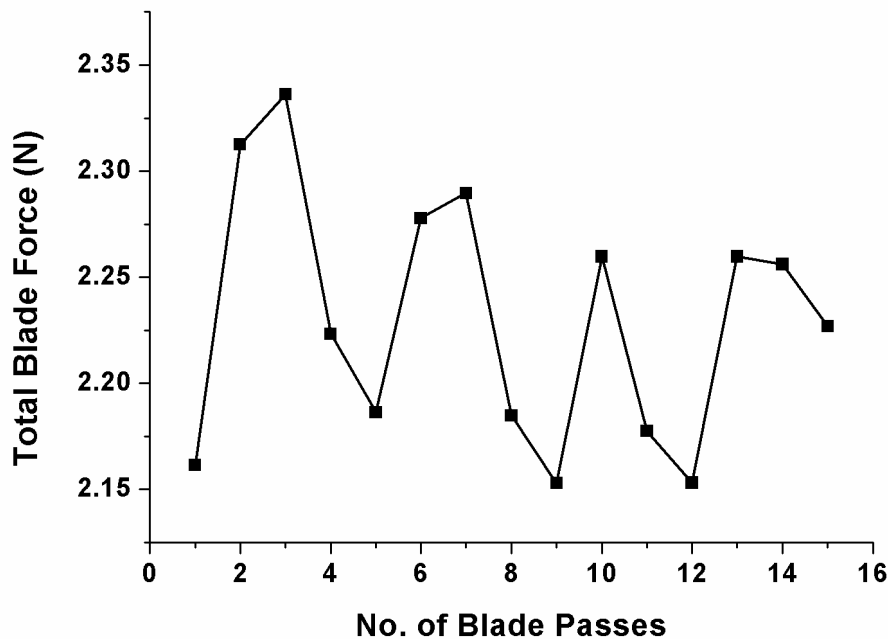
Figure 7.7. Blade force variation with No. of blade passes.

This is probably due to the inertia of the particle bed and because of initial and final blade position effects. The bed height is almost uniform initially when the blade moves from left to right for the first time. Therefore, the blade force during the first blade pass is lower than in the second pass. This is because the blade has to move a heap of particles accumulated due to sweeping of the particles at the end as the blade moved from left to right in the first pass and so on. After around three passes, the blade force effect is reversed and its value decreases than in the preceding pass. This is probably due to a repeated or cyclic pile-up of particles after around every three passes but with a reduced effect indicated by lower amplitude of each subsequent cycle.

Figure 7.8 shows interparticle normal force variation with the change in particle fill-level or bed-height.
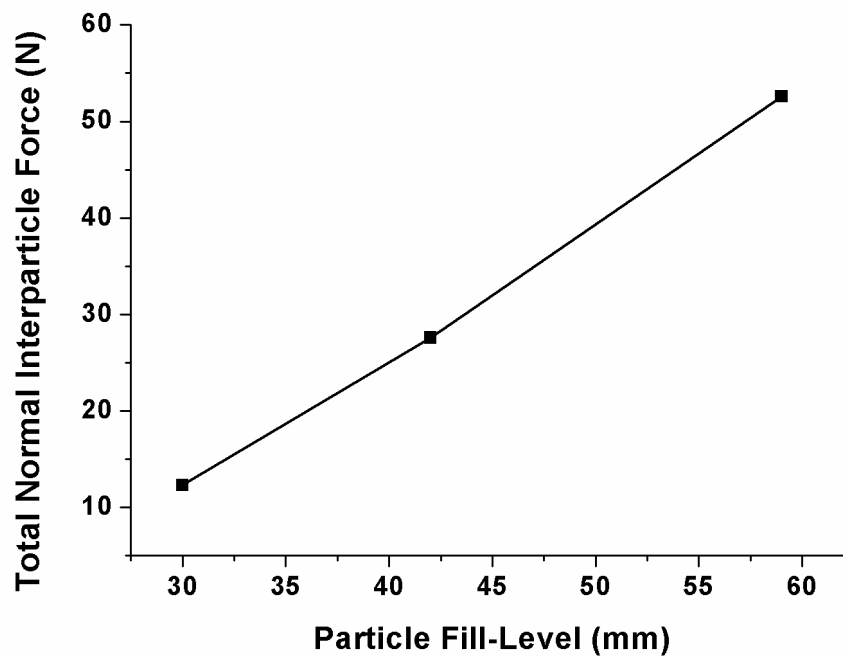
Figure 7.8. Interparticle normal force variation with fill level.

The trend shows an increase in normal contact forces as we increase the number of particles or bed-height in a fixed volume. The procedure for calculation of both normal and tangential forces is same as highlighted in the previous studies [1,2]. These forces were calculated by taking the sum of all interparticle forces, i.e., between white and white, white and red, and red and red particles at all time-steps and then averaging these normal or tangential forces over time steps from t=0.6 s and t=6.0 s for the first blade pass. For a constant blade angle and shape etc., the normal contact forces obviously increase with the increase in particle fill-level due to increased particle bed-height over a fixed volume.

Figure 7.9 shows interparticle tangential force variation with the change in particle fill-level.
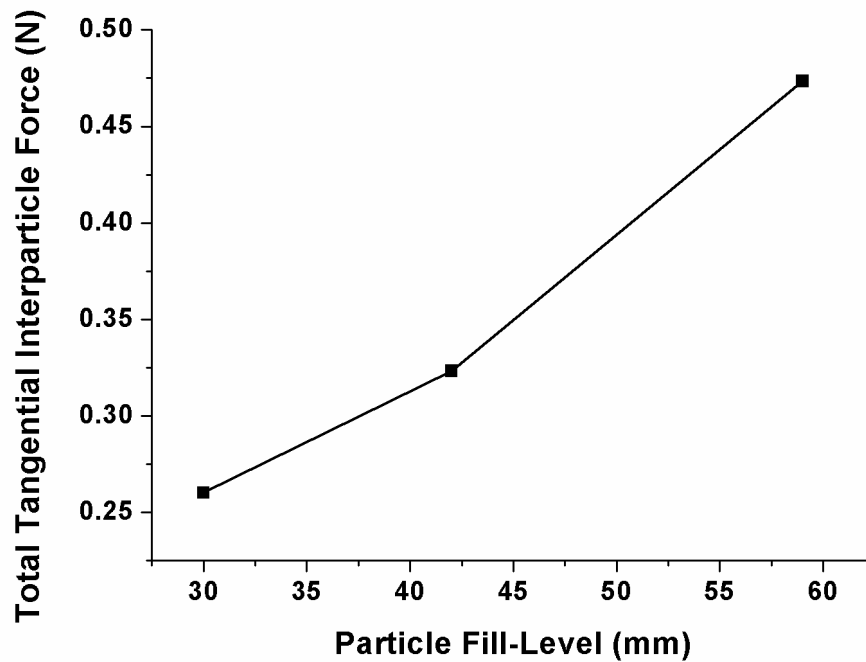
Figure 7.9. Interparticle tangential (shear) force variation with fill level.

The tangential force varies almost in the same way like normal force as shown in Fig. 7.8. The only difference is the force magnitude which is much higher in the case of normal forces. However, the magnitude of tangential forces in these cases is much lower than the normal forces as compared to previous studies [1,2]. This is probably due to an increased width of the box compared to particle diameter. The width of the box is 12 times the particle dia in this case (i.e., 0.048/0.004).

As discussed above, the interparticle (both normal and tangential) forces increase with the increase in particle fill-level due to an increased particle bed-height over a fixed volume.

Figure 7.10 shows interparticle normal force variation with the increase in number of blade passes for a fixed bed-height. The particle fill-level or bed-height in this case was fixed to 42 mm. The trend in the figure shows an interesting relationship, the normal contact force decreases almost exponential with the number of blade passes (up to 7 blade passes) and then shows a cyclic change after almost every three blade passes. The amplitude of this cyclic normal force changes after 7 blade passes is almost same.
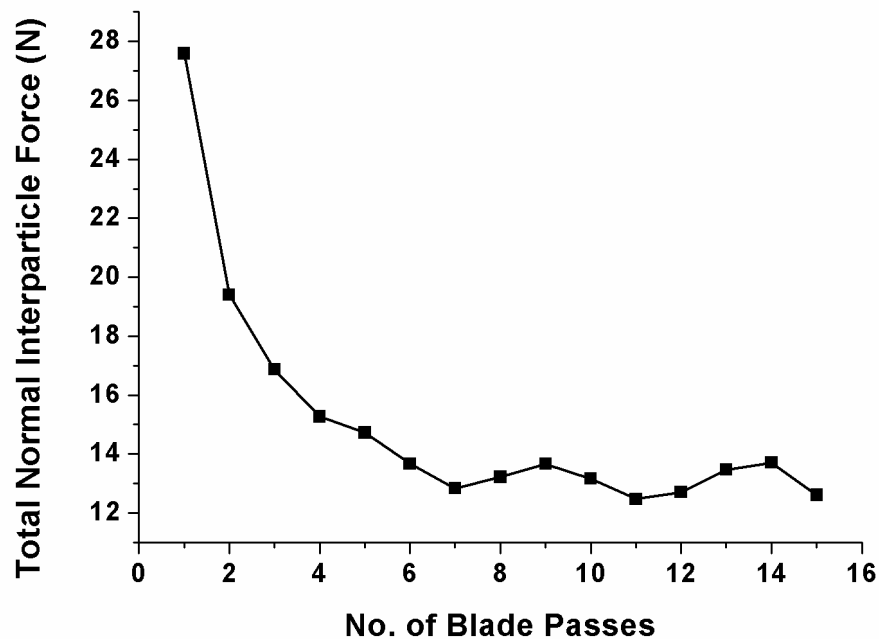
Figure 7.10. Interparticle normal force variation with No. of blade passes.

This is probably due to inertia of the particle bed. The particle bed is stationary in the beginning hence requires higher blade force as shown in Fig. 7.7. However, as the blade movement progresses continuously in forward and backward directions, the particles are in a kind of constant motion bringing the normal contact forces to an equilibrium value after around 7 blade passes.

Figure 7.11 shows interparticle tangential force variation with the increase in number of blade passes over a fixed bed-height.
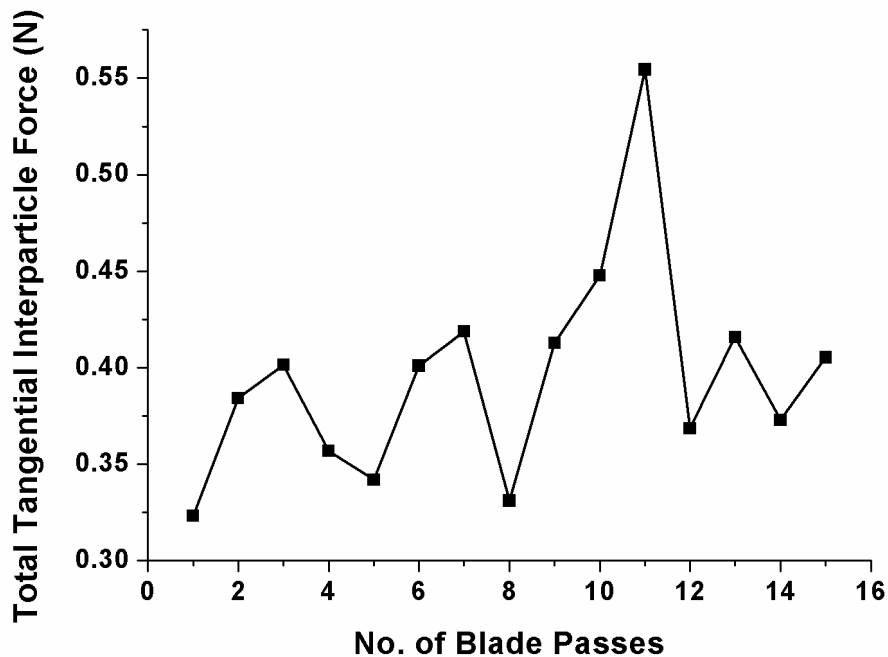
Figure 7.11. Interparticle tangential (shear) force variation with No. of blade passes.

Tangential force varies in almost a similar way like normal force as explained above. The only difference is the absence of initial exponential decrease in the magnitude of tangential contact force. It also shows an oscillating trend of blade force variation with the number of blade passes. It shows a cyclic change after almost every three blade passes like normal force curve, the only difference being the magnitude of tangential force which is much lower than the normal force.

Figure 7.12 shows mixing performance change with the change in particle fill-level. The mixing performance as indicated by MGMMI decreases with the increase in fill-level. This has also been studied in-depth for cylindrical mixers by Remy et al. [17].

_____
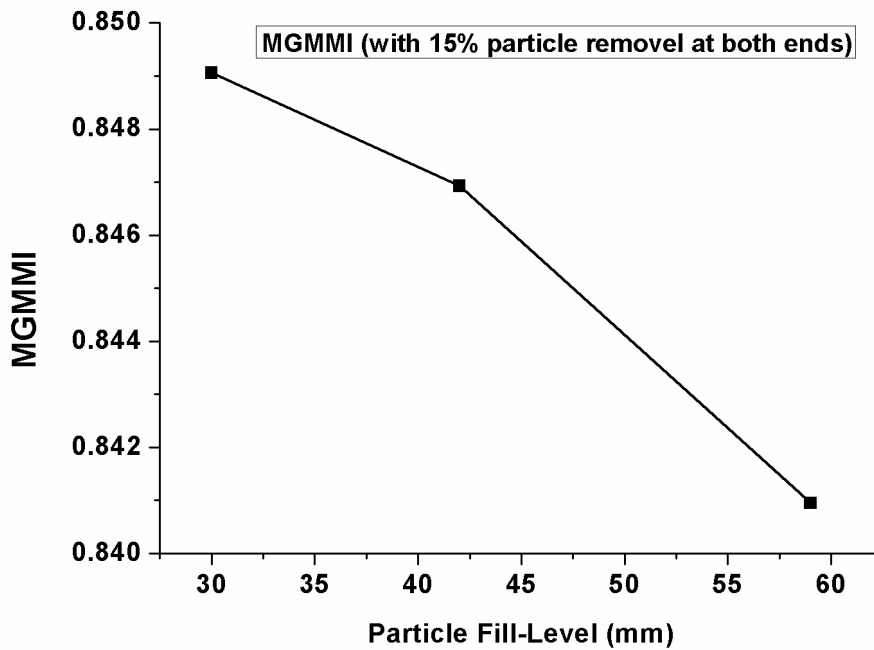
Figure 7.12. Mixing index variation with fill level.

This is due to the fact that at higher fill-levels or bed-heights the size of recirculation zone and diffusivities of particles reduce.

Figure 7.13 shows mixing performance variation with the increase of number of blade passes. The MGMMI was calculated by removing particles present in the 15% region at both ends of the box to avoid particle accumulation effects at these ends as evident from Fig. 7.5.

The trend for MGMMI variation with the number of blade passes shows an increase in the mixing performance at much higher rates in the beginning and then reaches an asymptotic value of mixing index after certain number of blade passes. This is obviously due to the fact that initially the two types of particles are completely separated or having minimum MGMMI value and thus have much higher diffusivities in the beginning which exhibit the much higher mixing performance during initial blade passes.
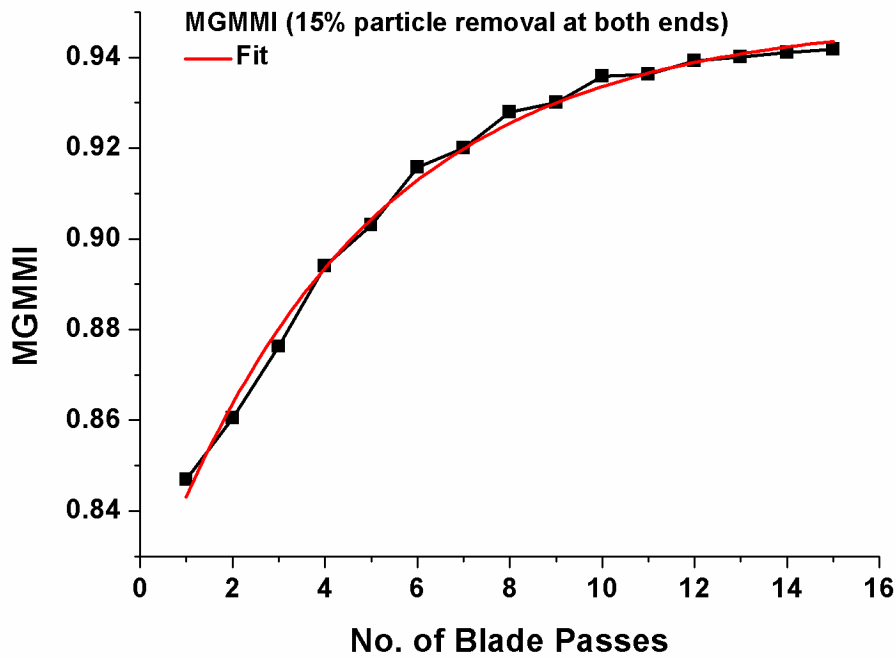
Figure 7.13. Mixing index variation with No. of blade passes.

The trend shown by MGMMI variation with the number of blade passes shows a typical exponential decay curve as shown by the exponential curve fit line indicated by red. The equation for this fit is:

$$(MGMMI)_{n+1} = (MGMMI)_n + A\,(e^{-n/t}) \tag{7.11a}$$

In this equation n is nth blade pass and A is constant in this equation and is equal to initial amplitude (MGMMI) of the curve. If t is replaced in terms of distance and velocity of the blade, i.e., $t=d/v$ then

$$(MGMMI)_{n+1} = (MGMMI)_n + A e^{-\frac{nv}{d}} \tag{7.11b}$$

This equation is valid when all other conditions like blade angle, blade shape, etc. are constant because MGMMI is also dependent on blade angle and blade shape etc. as concluded in our previous work [1,2].

It is clear from Eq. 7.11b that the after n number of blade passes the second additive term on the right hand side of the equation is dependent on nth value, i.e.,

number of blade pass, blade speed and the distance moved by the blade through particle bed. This additive term shows an inverse relation with *n* (the *nth* number of blade pass) and blade speed, i.e., it reduces at higher *n* values and higher blade speeds. The inverse relationship of mixing performance and blade speed was also concluded in our previous work [1] which showed decrease in MGMMI with the increase in blade speed. For a fixed *nth* blade pass, the additive term is higher if the distance through which blade is moved is larger. This is quite understandable that for a fixed volume and fixed blade speed, the mixing performance should be higher during any *nth* blade pass if the distance through which the blade is moved is larger.

7.5 Conclusion

In this study blade and interparticle forces were observed to have a direct relation with the fill-level, i.e., higher fill levels showed higher blade and interparticle contact forces.

The mixing performance had an inverse relation with the fill-level and MGMMI values decreased with the increase in fill-level or bed-height.

Number of blade passes were observed to have different results on blade forces and both normal and tangential interparticle contact forces. However, a cyclic change in the magnitude of these forces was observed after around three blade passes. The amplitude of these force values reached almost constant values after certain number of blade passes.

The mixing performance increased almost exponentially in the beginning with the increase in number of blade passes and reached an asymptotic value after certain number of blade passes similar to a typical exponential decay curve. A mathematical relationship was also derived for the change in mixing performance with regard to change in blade pass value *n*, blade speed and the distance through which blade is moved during the *nth* blade pass.

7.6 Nomenclature

abs	absolute (-)
C_n	normal damping coefficient (kg.s^{-1})
C_t	tangential damping coefficient (kg.s^{-1})
d_p	particle diameter (m)
E^*	reduced Young's modulus (-)
$\vec{F}$	force (N)
$\vec{F}_{cont,ij}$	contact force between particle i and j (N)
$\vec{F}_{drag,i}$	drag force on particle i (N)
$\vec{F}_{g,i}$	gravitational force on particle i (N)
$\vec{F}_n$	normal force (N)
$\vec{F}_{n-cont,ik}$	non-contact force on particle i by particle k (N)
$\vec{F}_t$	tangential force (N)
$\vec{F}_{total,i}$	total force on particle i (N)
I_i	moment of inertia (kg.m^2)
m	mass (kg)
m^*	reduced particle mass (-)
$\vec{M}_{ij}$	torque (Nm)
N	total number of particles of type $a+b$ (-)
n	n number of particles of type a (-)
$\hat{n}_c$	unit normal vector at contact point (-)
$\vec{R}$	vector of the mass center of the particle to contact plane (m)

R^*	reduced particle radius (-)
t	time (s)
$\vec{v}_c$	relative velocity of the two particles at their contact point (m.s^{-1})
$\vec{v}_c^t$	relative tangential displacement at contact (m)
$\vec{x}$	position in x-direction (m)
x, y, z	position of a particle in x, y, or z direction (m)
$x_{ref}, y_{ref}, z_{ref}$	reference position in x, y, or z directions (m)

Greek Letters

a	blade-rake angle (degree)
δ_n	relative normal displacement at contact (m)
δ_{max}	maximum relative tangential displacement when particle starts sliding (m)
$\dot{\gamma}$	shear rate [1/s]
$\dot{\gamma}^*$	dimensionless shear rate [-]
μ	friction coefficient (-)
ρ_p	particle density (kg.m^{-3})
$\vec{\omega}_i$	angular velocity (s^{-1})

Subscripts

a, b	type of particles
d	drag
g	gravitational
i	particle i
j	particle j
n	number of type a particles

7.7 References

[1]   M.S. Siraj, S. Radl, B.J. Glasser, J.G. Khinast, Effect of Blade Angle and Particle Size on Powder Mixing Performance in a Rectangular Box. Powder Technology 211 (2011) 100-113.

[2]   M.S. Siraj, J.G. Khinast, B.J. Glasser: Single-Blade Convective Powder Mixing: Impact of Blade Shape and Angle, Submission to Powder Technology (2012).

[3]   F.J. Muzzio, A. Alexander, C. Goodridge, E. Shen, T. Shinbrot. Solids Mixing Part A: Fundamentals of Solids Mixing. In: Edward L. Paul, Victor A. Atiemo-Obeng, Suzanne M. Kresta, ed. Handbook of Industrial Mixing: Science and Practice: John Wiley & Sons, Inc. (2004) 887–983.

[4]   P.J. Cullen, Food Mixing: Principles and Applications. New York, Wiley-Blackwell (2009).

[5]   P.M.C. Lacey, Developments in the theory of particle mixing. Journal of Applied Chemistry 4 (1954) 257-268.

[6]   R.L. Stewart, J. Bridgwater, D.J. Parker, Granular flow over a flat-bladed stirrer. Chemical Engineering Science 56 (2001) 4257-4271.

[7]   R.L. Stewart, J. Bridgwater, Y.C. Zhou, A.B. Yu, Simulated and measured flow of granules in a bladed mixer - a detailed comparison. Chemical Engineering Science 56 (2001) 5457-5471.

[8]   K. Malhotra, A.S. Mujumdar, H. Imakoma, M. Okazaki, Fundamental particle mixing studies in an agitated bed of granular materials in a cylindrical vessel. Powder Technology 55 (1988) 107-114.

[9]   K. Malhotra, A.S. Mujumdar, M. Okazaki, Particle flow patterns in a mechanically stirred two-dimensional cylindrical vessel. Powder Technology 60 (1990) 179-189.

[10]   K. Malhotra, A.S. Mujumdar, Particle mixing and solids flowability in granular beds stirred by paddle-type blades. Powder Technology 61 (1990) 155-164.

[11]   K. Malhotra, A.S. Mujumdar, M. Miyahara, Estimation of particle renewal rates along the wall in a mechanically stirred granular bed. Chemical Engineering and Processing 27 (1990) 121-130.

[12] B.F.C. Laurent, J. Bridgwater, D.J. Parker, Motion in a particle bed agitated by a single blade. AIChE Journal 46 (2000) 1723-1734.

[13] Y.C. Zhou, A.B. Yu, J. Bridgwater, Segregation of binary mixture of particles in a bladed mixer. Journal of Chemical Technology and Biotechnology 78 (2003) 187-193.

[14] Y.C. Zhou, A.B. Yu, R.L. Stewart, J. Bridgwater, Microdynamic analysis of the particle flow in a cylindrical bladed mixer. Chemical Engineering Science 59 (2004) 1343-1364.

[15] S.L. Conway, A. Lekhal, J.G. Khinast, B.J. Glasser, Granular flow and segregation in a four-bladed mixer. Chemical Engineering Science 60 (2005) 7091-7107.

[16] B. Remy, J.G. Khinast, B.J. Glasser, Discrete element simulation of free flowing grains in a four-bladed mixer. AIChE Journal 55 (2009) 2035-2048.

[17] B. Remy, J.G. Khinast, B.J. Glasser, The effect of mixer properties and fill level on granular flow in a bladed mixer. AIChE Journal 56 (2009) 336-353.

[18] B. Remy, T.M. Canty, J.G. Khinast, B.J. Glasser, Experiments and simulations of cohesionless particles with varying roughness in a bladed mixer. Chemical Engineering Science 65 (2010) 4557-4571.

[19] S. Radl, E. Kalvoda, B.J. Glasser, J.G. Khinast, Mixing characteristics of wet granular matter in a bladed mixer. Powder Technology 200 (2010) 171-189.

[20] G.R. Chandratilleke, A.B. Yu, R.L. Stewart, J. Bridgwater, Effects of blade-rake angle and gap on particle mixing in a cylindrical mixer. Powder Technology 193 (2009) 303-311.

[21] H.P. Zhu, Z.Y. Zhou, R.Y. Yang, A.B. Yu, Discrete particle simulation of particulate systems: Theoretical developments. Chemical Engineering Science 62 (2007) 3378-3396.

[22] P.A. Langston, U. Tüzün, D.M. Heyes, Continuous potential discrete particle simulations of stress and velocity fields in hoppers: transition from fluid to granular flow. Chemical Engineering Science 49 (1994) 1259-1275.

[23] P.A. Langston, U. Tüzün, D.M. Heyes, Discrete element simulation of granular flow in 2D and 3D hoppers: dependence of discharge rate and wall stress on particle interactions. Chemical Engineering Science 50 (1995) 967-987.

[24] P.A. Langston, U. Tüzün, D.M. Heyes, Discrete element simulation of internal stress and flow fields in funnel flow hoppers. Powder Technology 85 (1995) 153-169.

[25] Y.C. Zhou, B.D. Wright, R.Y. Yang, B.H. Xu, A.B. Yu, Rolling friction in the dynamic simulation of sandpile formation. Physica A 269 (1999) 536-553.

[26] H.P. Zhu, A.B. Yu, Averaging method of granular materials. Physical Review E 66 (2002) 1-10.

[27] B.N. Asmar, P.A. Langston, A.J. Matchett, A generalized mixing index in distinct element method simulation of vibrated particulate beds. Granular Matter 4 (2002) 129-138.

[28] GDR Midi, On dense granular flows. European Physical Journal E 14 (2004) 341-365.

[29] G.I. Tardos, S. McNamara, I. Talu, Slow and intermediate flow of a frictional bulk powder in the Couette geometry. Powder Technology 131 (2003) 23-39.

8 Conclusions and Future Work

8.1 Conclusions

The first part of the study was intended to understand the impact of granular flow characteristics like particle size ratio (r), blade angle, blade speed and wall friction on granular flows and on mixing performance using a single blade. It was observed that interparticle forces had an inverse relation with the blade-rake angle. Blade forces varied inversely with respect to the blade-rake angle and were higher for systems comprising of larger particles and wall friction. Rapidly increased blade forces and particle locking at highly acute blade angles of < 60° may result in the locking of the mixer. Binary mixtures of different-sized particles, $r=(d_{p,top}/d_{p,bot}) < 1.0$ resulted in higher mixing performance at a given blade-rake angle than those having $r > 1.0$ which was true for both acute and obtuse angle ranges leading to the conclusion that larger particles should be filled first in a convective powder blender. For the same *r-value*, the highest mixing performance was observed in the range of 70° to 90° blade rake angles. This study is helpful to understand and to improve the design of industrial convective mixers using two different-sized particles.

The second major part of the study was to investigate the flow across a single blade and to study the impact of blade shape and blade angle on the flow and mixing of two different sized monodisperse mixtures. Three blade shapes, i.e., concave, convex and straight shapes were used. The effect of blade force variation was different for all three blade shapes used. The maximal blade force was observed for the concave blade shape, followed by the straight and then the convex shapes. Thus, convex blades resulted in energy minimization of an industrial mixer. The maximum of the forces were always exerted on the bottom part of the blade, thus providing information on the construction of industrial mixers. Average interparticle forces depend inversely on the blade-rake angle values. The interparticle forces were higher at lower angles, and especially at strongly acute angles. In terms of blade shapes, these forces were higher for the concave shaped

blades followed by the straight and the convex shapes. This led to the conclusion that shear and normal-force sensitive materials should be mixed in blenders with obtuse blade angles and convex or straight blade shapes to prevent damage to the powders. For acute angles, convex blades give the best mixing performance although concave blades exert the maximum forces on the bed. For high angles, concave blades give the best mixing.

Third part of the study focused mainly on the effects of particle fill-levels and number of blade passes on blade force variation, interparticle contact forces and on mixing performance efficiency. In this study blade and interparticle forces were observed to have a direct relation with the bed height or fill-level and higher fill levels showed higher blade and interparticle contact forces. The mixing performance had an inverse relation with the fill-level and decreased with the increase in bed-height. Number of blade passes was observed to have different effects on blade force and both normal and tangential interparticle contact forces. The mixing performance showed an exponential increase with the increase in number of blade passes in the beginning and reached an asymptotic value after certain number of blade passes. A mathematical relationship was also derived for the change in mixing performance with regard to change in number of blade pass value n, blade speed and the distance through which blade is moved during the nth blade pass.

8.2 Future Work

The future work may typically cover:

1. Extension of the work to cohesive flows.

2. Extension of the work to the study covering non-spherical particles.

3. Formulation of 'mathematical relationships' for the effects of particle size ratios, particle shape, particle-particle and particle-wall friction, blade rake angle, blade shape, fill-level or bed height, position and number of blades, etc., on particle diffusion and mixing performance.

4. Extension of the work to large granular flows, typically in millions, to mimic real industrial processes.

5. Extension of the work to the wet granular flows covering study of liquid bridges and effect of moisture content, etc.

6. Experimental validation of the results for both dry and wet granular flows.

7. Study of temperature and pressure distribution during mixing for both dry and wet granular flows.

8. Study of processes covering phase change of solid particles, for example hot melt extrusion process. Study of temperature and pressure distribution during this process and possible ways to add or remove heat during the process.

9. Study of the processes involving chemical reactions for different solids in the dry/wet phase and,

10. Formulation of universal constituent equations as in fluids like Newton and Navier Stokes equations.

Resume

	01 April 1994 - 01 August 1999
Title of qualification awarded	B.Sc. in Chemical Engineering
Name and type of organisation providing education and training	University of Engineering & Technology, G.T. Road, Lahore Pakistan.

	01 February 2000 - 01 September 2001
Title of qualification awarded	M.Sc.
Principal subjects / occupational skills covered	M.Sc. in Nuclear Engineering
Name and type of organisation providing education and training	Pakistan Institute of Engineering and Applied Sciences (PIEAS) Nilore, Islamabad, Pakistan.

	June 2008 - Present
Occupation or position held	PhD Student
Main activities and responsibilities	PhD in Chemical/Process Engineering (Modeling and Simulation of Granular Flows using Discrete Element Method, DEM)
Name and address of employer	Graz University of Technology, Inffeldgasse 21a, 8010 Graz, Austria.

Publications (Journal)

1. **M.S. Siraj**, S. Radl, B.J. Glasser, J.G. Khinast: Effect of Blade Angle and Particle Size on Powder Mixing Performance in a Rectangular Box, ***Powder Technology*** 211 (2011) 100-113.

2. **M.S. Siraj**, J.G. Khinast, B.J. Glasser: Single-Blade Convective Powder Mixing: Impact of Blade Shape and Angle, Submission to ***Powder Technology*** (2012).

3. **M.S. Siraj**, S. Radl, D. Brandl, H. Heimburg, B.J. Glasser, J.G. Khinast: Investigation of Granular Flow and Mixing Due to a Single Blade, in preparation for submission to ***Chemical Engineering Science*** (2012).

4. **M.S. Siraj**: Energy Resources – The Ultimate Solution. ***Renewable and Sustainable Energy Reviews***. 16 (2012) 1971-1976.

5. **M.S. Siraj**: Improvement of Power Conversion Efficiency of P3HT/PCBM Polymer Solar Cell Systems by Optimization of the Process Steps Involved, ***Synthetic Communications***. 2012 (In-Press), DOI: 10.1080/00397911.2010.548619.

6. S. Radl, **M.S. Siraj**, D. Brandl, J.G. Khinast: Wet Granular Flows - Impact of Cohesion on Particle Mixing, Chemie Ingenieur Technik 81: 1151 (2009).

_____

Publications (Conference):

1. **M.S. Siraj**, S. Radl, J.G. Khinast: Effects of Blade Shape and Angle On Solid Particle Mixing Using 2D and 3D Discrete Element Simulations, AIChE Annual Meeting, Nov 7-12, 2010, Salt Lake City, UT (USA).

2. **M.S. Siraj**, S. Radl, J.G. Khinast: Simulation Studies for the Effects of Particle Size and Blade Rake Angle on Particle Mixing, PMS06, 8th Central European Symposium on Pharmaceutical Technology, September 16-18, 2010, Graz (Austria).

3. **M. S. Siraj**: Improving Power Conversion Efficiency (PCE) of Polymer Solar Cells, 3rd Symposium on Engineering Sciences, University of the Punjab, Mar 10, 2010, Lahore (Pak).

4. **M. S. Siraj**: Future Energy Options and Policy Guidelines for Pakistan, 3rd Symposium on Engineering Sciences, University of the Punjab, Mar 10, 2010, Lahore (Pak).

5. **M.S. Siraj**: Death of Energy, AIChE Annual Meeting, Nov 8-13, 2009, Nashville, TN (USA).

6. D. Suzzi, S. Adam, S. Radl, S. Fraser, C. Voura, D. Koller, D. Brandl, **M.S. Siraj**, J.G. Khinast; DEM and QbD: Validation Studies towards a Virtual Design Space, Medeso Pharma Seminar. Oct 29, 2009, Copenhagen (Denmark).

7. S. Radl, **M.S. Siraj**, D. Brandl, J.G. Khinast; Wet Granular Flows – Impact of Cohesion on Particle Mixing, ProcessNet, Sep 2009, Mannheim (Germany).

8. S. Radl, D. Brandl, H. Heimburg, **M. S. Siraj**, J.G. Khinast; Size Effects and Agglomerate Formation in Granular Flows, International Graz Congress for Pharmaceutical Engineering, Sep 17-18, 2009, Graz (Austria).